Palacký University Olomouc
Faculty of Science

Doctoral thesis

Coherent Control of Gamma-radiation Intensity by Vibrating Resonant Medium

Author: Mgr. Aleš Stejskal
Supervisor: doc. Mgr. Vít Procházka, Ph.D.
Study field: Applied Physics
Study form: full-time
Year: 2023

Bibliographical identification:

Author:	Mgr. Aleš Stejskal
Title:	Coherent Control of Gamma-radiation Intensity by Vibrating Resonant Medium
Type of thesis:	Doctoral
Department:	Joint Laboratory of Optics Palacký University in Olomouc and Institute of Physics of the Czech Academy of Sciences
Supervisor:	doc. Mgr. Vít Procházka, Ph.D.
The year:	2023
Number of pages:	86
Supplements:	1
Language:	English
Keywords:	Coherent gamma-radiation control, Mössbauer effect, high-frequency vibrating resonant medium, piezoelemnt control, time-resolved Mössbauer measurements, FPGA, Mössbauer spectrometer

Bibliografická identifikace:

Autor:	Mgr. Aleš Stejskal
Název práce:	Koherentní kontrola intenzity gama záření pomocí vibrujícího rezonančního prostředí
Typ práce:	Dizertační
Pracoviště:	Společná laboratoř optiky UP a FZÚ AV ČR
Vedoucí práce:	doc. Mgr. Vít Procházka, Ph.D.
Rok obhajoby práce:	2023
Počet stran:	86
Počet příloh:	1
Jazyk:	Anglický
Klíčová slova:	Koherentní řízení intenzity gama záření, Mössbauerův jev, vysokofrekvenční vibrace rezonančního prostředí, časově rozlišená Mössbauerovská měření, FPGA, Mössbauerův spektrometr

Abstract

This study explores the coherent control of gamma-ray intensity by the resonant recoilless interaction, the so-called Mössbauer effect, in the vibrating resonant medium. The Mössbauer effect is traditionally used to analyse material properties, but recent findings in the field of nuclear quantum optics have increased interest in this phenomenon. Inspired by the current state of the art, this work follows on previous publications that used harmonically vibrating resonant absorbers to manipulate gamma radiation in the time and energy domain, which led to the discovery of gamma pulses or acoustically induced transparency. In this work, the concept of gamma radiation intensity control by vibrating absorber is generalised to multi-tone vibrations. More harmonic frequencies are used to create diverse profiles of the absorber motion, which extends the possibilities of controlling of the gamma radiation intensity waveforms. The generation of narrow well-separated, high-intensity, single and double gamma pulses, or the newly discovered short-time acoustically induced absorption, is predicted by numerical simulations and proven experimentally. A significant part of the presented work is devoted to the description of the purpose-built experimental equipment and the methodology for measuring the frequency response function of the piezoelectric transducer vibrating at high frequencies with picometre amplitudes. At the end, the experimental imperfections and limitations of the gamma radiation intensity control by vibrating absorber are discussed, and possible applications and further improvements are suggested.

Abstrakt

Tato práce se zabývá koherentním ovládáním intenzity gama záření pomocí rezonanční bezodrazové interakce, tzv. Mössbauerova jevu, ve vibrujícím rezonančním prostředí. Mössbauerův jev se tradičně používá k analýze vlastností materiálů, ale nedávné poznatky v oblasti jaderné kvantové optiky zvýšily zájem o tento jev. Práce je inspirovaná nejnovějšími objevy a navazuje na nedávné publikace, které využívaly harmonicky vibrující rezonanční absorbátory pro manipulaci s gama zářením v časové a energetické doméně, což vedlo k objevení gama pulzů nebo akusticky indukované transparence. Koncept řízení intenzity gama záření pomocí vibrujícího absorbátoru je v této práci zobecněn na vibrace složené z více harmonických frekvencí, což umožňuje generování různorodých tvarů vibrací absorbátoru, které rozšiřují možnosti ovládání průběhů intenzity gama záření. Generování úzkých v čase oddělených jednoduchých a dvojitých gama pulzů o vysoké intenzitě nebo nově objevená krátkodobá akusticky indukovaná absorpce, jsou předpovězeny numerickými simulacemi a následně prokázány experimentálně. Podstatná část práce je věnována popisu speciálně vyvinutého experimentálního vybavení a metodice měření frekvenční odezvy piezoelektrického transduceru, který kmitá na vysokých frekvencích s pikometrovými amplitudami. V závěru práce jsou pak diskutovány experimentální nedokonalosti a omezení ovládání intenzity gama záření pomocí vibrujícího absorbátoru a jsou navrženy možné aplikace a další zlepšení.

Proclamation

I declare that I have written this thesis by myself, using the cited sources, and that the thesis has not been submitted, in whole or in part, in any previous application for an academic degree. The text was improved by suggestions from DeepL Write, the open source generative artificial intelligence tool.

In Olomouc ....

Signature

Acknowledgement

I would like to express my gratitude to my supervisor Vít Procházka for his support and guidance throughout my doctoral studies. I am also thankful to Michal Dudka and Vlastimil Vrba for their expert advice in electronics and nuclear forward scattering theory. I would like to thank Honza Gregar for the final language correction of the thesis and other colleagues for valuable discussions and advice.

I would also like to acknowledge the financial support provided by the internal IGA grant of Palacký University, Czech Republic (IGA_PrF_2023_003).

Most importantly, I would like to thank my girlfriend and my family for their unwavering support and patience while I was working on my dissertation.

Contents

Introduction

The aim of this work is to introduce the coherent manipulation of gamma radiation by the vibrating resonant absorber. For this purpose, the coherent resonant recoilless interaction of the gamma radiation with the nuclear energy levels, the so-called Mössbauer effect, is utilised. For many decades, the Mössbauer effect has been exploited primarily for the investigation of material properties [1–3]. Recently, however, it has again become a subject of interest in the field of nuclear quantum optics, which extends the principles of classical optics to the gamma-ray and hard X-ray regimes [4–9]. Especially the phenomena related to the gamma laser are of great interest [10,11]. Although experiments manipulating the gamma photons by harmonically vibrating absorbers, which led to the observation of comb-like structures [12,13], gamma echoes [14–16] or quantum beats [17], were conducted from the 60s of the 20th century, the impact of the harmonic vibrations on the energy and time domain of the gamma photon field was explained properly recently [18–20].

Since then, the effects of a single-frequency vibrating absorber, such as acoustically induced transparency [21, 22] or gamma pulses generation [23–26], were described and the potential applications in the field of metrology [27, 28], quantum computing [25], nuclear quantum dynamics [29] etc. were proposed. Moreover, similar type of quantum optics experiments are performed not only with the radioactive source, but also with the synchrotron radiation. At these facilities, phenomena such as electromagnetically induced absorption [30] or radiation spectral narrowing [31] were observed. In addition, another theoretical works are devoted to the topics such as thin film X-ray cavities [32,33] or single photon mode quantum entanglement [34].

This work is inspired by the state of the art in the rapidly developing field of nuclear quantum optics and focuses on the particular topic of shaping gamma radiation intensity by vibrating absorber. Up to date, only the control of radiation intensity by harmonic vibrations, which provides limited possibilities, was properly described and experimentally proved. The work has two objective: the first is the investigation of the coherent gamma radiation intensity control by the multi-tone vibrating absorber, which should extend this concept in a general form. The second is the development of the experimental equipment which is necessary for performing the nuclear quantum experiments, which require investigation of the gamma photon field in both the energy and time domain.

The present thesis is divided into three main chapters. In the first chapter, the theoretical overview is provided, including the special terms and units used, and numerical calculations and predictions are made. The second chapter deals with the experimental equipment developed for the needs of the experiments. Finally, the third chapter describes the methodology and the experiments for the control of the gamma radiation intensity by the multi-tone vibrating absorber.

1 Gamma Radiation Scattering in Resonant Environment

Scattering of gamma radiation in the matter consisting of nuclei and electrons covers several fundamental processes such as the photoelectric effect, Compton scattering, nuclear resonant scattering, etc., which are exploited for various gamma-ray and X-ray spectroscopy techniques [35–38]. These interactions can basically be classified as either resonant or non-resonant, incoherent or coherent, elastic or inelastic [35,39]. In the present work, we are only interested in the coherent elastic resonant nuclear scattering, i.e. the so-called Mössbauer effect discovered in 1958 by Rudolf Mössbauer [40]. The other interactions are unwanted and lead to noise detections that contribute to the non-resonant background in the Mössbauer experiments.

Energies of gamma photons range from units of kiloelectronvolts to megaelectronvolts, which make the excitation and deexcitation process of the nuclear energy levels more problematic than the excitation of electron energy levels in the atomic shell. High energy photons have a relatively large momentum P, which is proportional to the photon energy E as $P = E/c$, where c is the speed of light in vacuum. It means that resonant absorption and emission contend with the non-negligible momentum transfer to the nucleus, which causes that the energy of absorbed and emitted gamma photon differs from the resonance by the energy of the recoil. Since the linewidths of the nuclear resonant lines are typically several orders of magnitude smaller (e.g. in the nanoelectronvolt range) than the energy of recoil (in the miliecetronvolt range), the emission and absorption spectra do not overlap. Nuclear resonant excitation and deexcitation is then possible only by inelastic interaction with the phonon creation or annihilation [1,37,41].

Nonetheless, recoilless coherent emission and absorption of the gamma photon is possible via the aforementioned Mössbauer effect. This interaction is explained as a collective excitation of an ensemble of nuclei (nuclear exciton [37]), where the momentum of the photon is transferred to the mass of the whole ensemble, which makes the recoil energy negligible, and therefore allows excitation at resonance energy. The coherence of the process resides in the fact that the nuclear system (including the core electrons) returns to the initial state after deexcitation, and hence the individual scattering paths are indistinguishable and equally probable. The interference of all these scattering amplitudes creates a scattered photon field which is emitted dominantly in the forward[1] direction. In the incoherent processes, compared to this, it is, in principle, possible to track the particular scattering nucleus because it did not return to the initial state. From this point of view, each incoherent process involves a single atom, which means that reemission of the photon or other secondary particle (conversion electron or characteristic X-ray photon) is isotropic, i.e. all directions have the same probability [37].

The resultant photon field of the resonant scattering process is given by the sum of the probabilities of all independent and indistinguishable processes. Besides the coherent resonant interaction (including multiple scattering), the photon can simply pass through the resonant environment without any interaction. Since the other interactions may be neglected, the resultant photon field of the scattering process is given by the interference of the incident wave (passing without interaction) and the scattered wave. The observed out coming radiation intensity then depends on the

[1] In the crystals, a weaker emission occurs also in the Bragg reflection angles [37].

amplitudes and relative phases of these two waves, which in general depend on the properties of the scatterer (motion, energy structure).

Primarily, the resonant scattering process is influenced by the hyperfine nuclear energy levels, which are manifested by a decrease in the radiation intensity (absorption line) at transition energies. Thus, the Mössbauer effect is utilised in Mössbauer spectroscopy for investigation of condensed matter properties such as lattice structure, spin state, oxidation state or magnetic properties [1,3]. Specifically, a Mössbauer nucleus acts as a probe whose energy levels shift and split in dependence on the electric (electron density) and magnetic fields that the nucleus feels in its centre. These fields are dominantly influenced by the atomic core electrons, whose state is sensitive to chemical bonds and lattice arrangement.

The material spectroscopy is, however, not of interest in this thesis, because we exploit here the Mössbauer effect and the corresponding equipment primarily for a coherent manipulation with the gamma photons. Nevertheless, the basics of Mössbauer spectroscopy are described in the following section in order to explain the theoretical and experimental terms used in the present thesis. After that, two further sections are devoted to the acoustically induced interference effects caused by the scattering in the high-frequency vibrating absorber. First, an already explained model of the harmonically vibrating absorber is introduced. Second, the absorber vibrating with a periodical, but arbitrarily shaped motion profile is investigated to be used for the gamma radiation intensity control.

1.1 Mössbauer Spectroscopy Basics

The hyperfine structure of the nuclear energy levels investigated by the Mössbauer effect typically exhibits energy differences and linewidths in the nanoelectronvolt scale. Performing such spectroscopy requires sufficiently monochromatic and intense photon sources to effectively excite the sample. Two basic types of sources are utilised: a radioactive source and a synchrotron radiation source. Since all the experiments in this work were conducted with the radioactive source, we omit the description of Mössbauer spectroscopy with synchrotron radiation and only refer to relevant literature [37,42–45].

Radioactive sources for Mössbauer spectroscopy have to be the isotopes which disintegrate to the excited state of the investigated nuclide and which have an applicably long half-life. Such sources have the advantage that the emission line width is the same as the absorption linewidth of the investigated nuclei. On the other hand, radioactive materials irradiate randomly in all directions and the polarisation state of the gamma photons is mixed. In addition, they can also emit another unwanted gamma photons or particles, which typically contribute to the noise and thus decrease the signal-to-noise ratio [1,41].

Performing Mössbauer spectroscopy with the radioactive source requires a modulation of the energy of the gamma photons. The maximum required energy modulation range ΔE depends on the isotope used, but is typically in the range of several hundreds of nanoelectronvolts for the photon energy E_0 in tens of kiloelectronvolts. Fortunately, such modulation can be easily realised by the Doppler effect with velocities v in tens of millimetres per second according to the relation $\Delta E = \frac{v}{c} E_0$. In practice, the radioactive source is screwed onto a Doppler energy modulation unit, hereafter called a transducer, which moves the source back and forth with a linear velocity profile (triangle, saw). The basic arrangement of the Mössbauer spectrometer in the transmission

geometry is shown in Figure 1. It consists of the transducer, radioactive source, examined sample (absorber), detector of gamma radiation, amplifier and data acquisition system (DAQ). Transducer sweeps the energy of the gamma photons, which interact with the investigated absorber, and the scattered photon field is registered by a gamma radiation detector (semiconductor, gas or scintillation). Since the photons are emitted randomly and other unwanted photons and particles are registered, the important task of the DAQ system, besides the control of motion profile of the transducer, is also the selection of the particles (pulses) of required energy (amplitude) and their sorting with respect to the Doppler energy modulation [3].

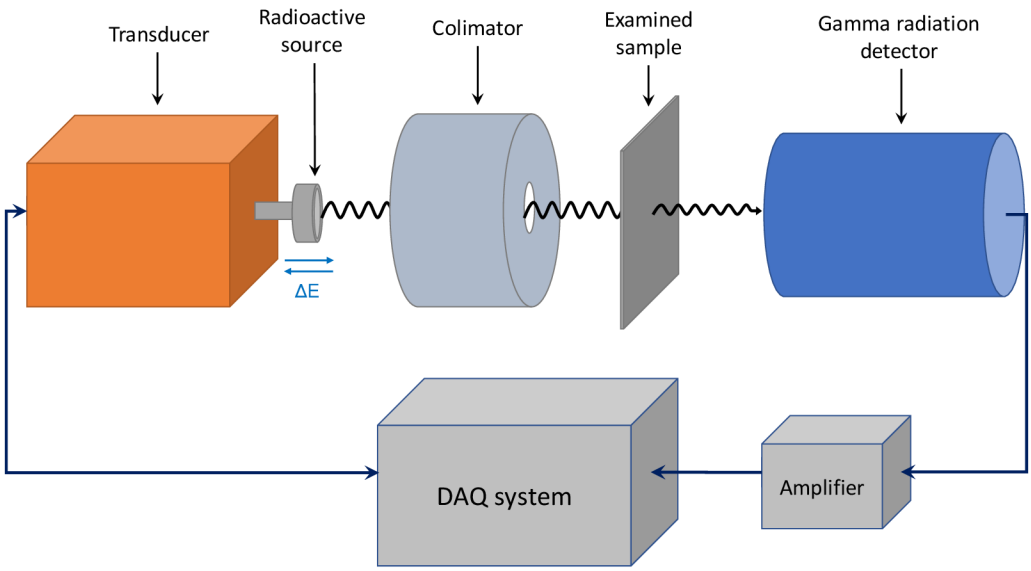

Figure 1: *Transmission Mössbauer spectroscopy setup arrangement.*

It should be noted that not all isotopes are suitable for the Mössbauer spectroscopy for various reasons. The Mössbauer effect has only been observed in 42 elements and 72 isotopes [1]. In addition, for some isotopes there are no suitable radioactive sources or they have too short decay times, making their usage practically infeasible. Furthermore, the probability of recoilless emission and absorption, the so-called Lamb-Mössbauer factor, varies for each isotope, and for higher energies of the nuclear transitions it decreases to such an extent that the signal-to-noise ratio is too low for practical use. The most commonly used Mössbauer isotopes are ^{57}Fe, ^{119}Sn, less frequently ^{151}Eu, ^{129}I, ^{121}Sb and others [1, 46]. In this work, all experiments are performed with the ^{57}Fe isotope, which is described in the following subsection.

1.1.1 ^{57}Fe Mössbauer Isotope

Mössbauer spectroscopy with ^{57}Fe examines the energy transition between the first excited state (spin 3/2, energy $\approx$ 14.41 keV) and the ground state (spin 1/2). The natural linewidth Γ_0, the full width at half maximum (FWHM), of the recoilless emission and absorption is 4.66 neV (0.097 mm/s), which comes from the excited state mean lifetime $t_{\text{life}} = 141.1$ ns according to the Heisenberg uncertainty principle ($\Gamma_0 = \hbar/t_{\text{life}}$), where $\hbar$ is reduced Planck constant. The gamma photon has energy 14.41 keV and allows to penetrate the samples to a depth of several tens of μs in the transmission

geometry. This neither low nor high energy is associated with a comparatively high Lamb-Mössbauer factor $\approx$ 0.5–0.8. On the other hand, the natural abundance of this isotope is only 2.119 %. Therefore, in specific cases, the investigated sample is enriched with the ^{57}Fe isotope to increase the scattering probability which results in enhancement of the signal-to-noise ratio.

The corresponding radioactive source for ^{57}Fe is ^{57}Co which disintegrates by electron capture into the ^{57}Fe nucleus in the second excited state dominantly (99.8 %). This decay has a relatively long mean lifetime of 392.1 days, so the source can be utilised for Mössbauer measurements for several years. The ^{57}Fe nucleus deexcites from the second energy level either to the ground state (10,71 %) emitting a 136.47 keV photon, or mostly to the first excited state (85.49 %) accompanied by the emission of a 122.07 keV photon, see Figure 2 which depicts the dominant gamma transitions in ^{57}Co. The 14.41 keV gamma photons needed for the spectroscopy are produced by deexcitation of the first energy level. Although the ^{57}Fe nucleus gets to the first excited state in 85.49 cases per 100 disintegrations of ^{57}Co, the 14.41 keV photon escapes from the source in only 9.18 cases per 100 disintegrations. This difference is due to the interactions of the emitted 14.41 keV gamma photon with the internal electrons of the atom, which lead to the secondary emission of conversion electrons, Auger electrons and characteristic X-ray photons of miscellaneous energies, see the complete decay scheme of ^{57}Co listed in reference [47]. In the context of the Mössbauer experiments, we should mention also the conversion electrons and X-ray photons with energies between 5.3 keV and 7.3 keV which used to be labelled in a simplified way as 6.4 keV particles.

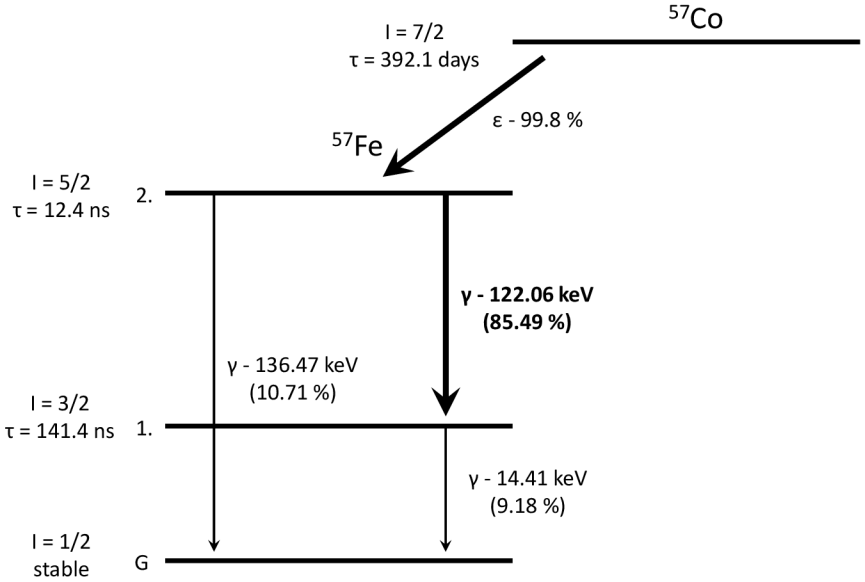

Figure 2: *Relevant gamma transitions in the ^{57}Co radioactive decay. Probabilities are given per 100 disintegrations of ^{57}Co nuclei.*

Based on the aforementioned facts, the ^{57}Co decay scheme is often simplified to 122 keV, 14 keV gamma photons and 6 keV electrons and X-rays. We are primarily interested in the 14 keV gamma photons. The energy of these photons is modulated by the Doppler effect, where the velocity of 1 mm/s changes the energy by 48,04 neV, i.e. $10.31\Gamma_0$. A huge amount of 122 keV photons is usually undesirable because their inter-

action with the matter leads to production of the Compton continuum, characteristic X-rays, high energy electrons etc, which contribute to the non-resonant background. However, the 122 keV photons find utilisation in time measurements, where their detection labels the time of origin of the first excited state. Particles with the energy about 6 keV deserve attention for two reasons. First, they create a significant peak in the energy spectrum, which has to be considered when selecting the 14 keV photons with an amplitude discriminator. Second, the conversion electrons and X-ray photons with the energy between 5.3 keV and 7.3 keV may also be used to investigate the hyperfine energy structure of the ^{57}Fe in the conversion X-ray Mössbauer spectroscopy (CXMS) and conversion electron Mössbauer spectroscopy (CEMS) [2,48,49].

1.1.2 Hyperfine Interactions

The nuclear energy levels are influenced by three basic interactions: the Coulombic interaction, the quadrupole interaction and the magnetic dipole interaction (magnetic splitting). For the ^{57}Fe, these interactions are shown in Figure 3. In the Coulombic interaction, the nuclear charge interacts with the electric field of s-electrons in the atomic shell, which are the only electrons with a non-zero occurrence probability in the centre of the nucleus. Since the spatial distribution of the positive nuclear charge differs for the ground and excited state, both levels are not shifted by the same value. As a result, the transition energy changes by a so-called isomeric shift, which is seen in the Mössbauer spectrum as an shift of the absorption line position [1,3].

The quadrupole interaction describes the interaction of the dipole moment of the nucleus with the electric field gradient. In the case of ^{57}Fe, the ground state does not split due to the half spin value, but the excited state splits into two levels. Thus, two absorption lines (doublet) are observed in the Mössbauer spectrum [2,3].

Within the magnetic interaction, the nucleus in the non-zero spin state interacts with the effective (hyperfine) magnetic field B_{hf} by means of its magnetic dipole moment. In general, there are several contributions to the effective magnetic field, including the external field. The most important of the inner magnetic fields are those generated by the Fermi contact field and the coupling of the nuclear spin with the orbital moment of the electrons [2]. The magnetic interaction causes the splitting of the energy levels to the equally spaced substates (Zeeman multiplet) with different nuclear magnetic spin quantum numbers m. In the case of ^{57}Fe, the ground state splits into two levels ($m = +1/2, -1/2$) and the excited state splits into four levels ($m = -3/2, -1/2, +1/2, +3/2$). It gives in total eight transitions, but due to the selection rules for magnetic interaction transitions [3] only six of them are possible, so the six absorption lines (sextet) are visible in the Mössbauer spectrum.

In practice, the aforementioned interactions combine. Typically, the sample contains Mössbauer nuclei in different states. Since in the transmission Mössbauer spectrum we observe the integral contribution of all nuclei, the spectrum may consist of various components (singlets, doublets, sextets), which may even exhibit a distribution of isomeric shift or effective magnetic field.

A deeper explanation of the relations between the hyperfine parameters and the structure of the examined sample is not important for the present thesis because we are interested only in the calculations of the scattered gamma radiation field. For these, the knowledge of the hyperfine parameters is sufficient to describe the absorption line shape and to find the resonant (effective) thickness, see the following subsection.

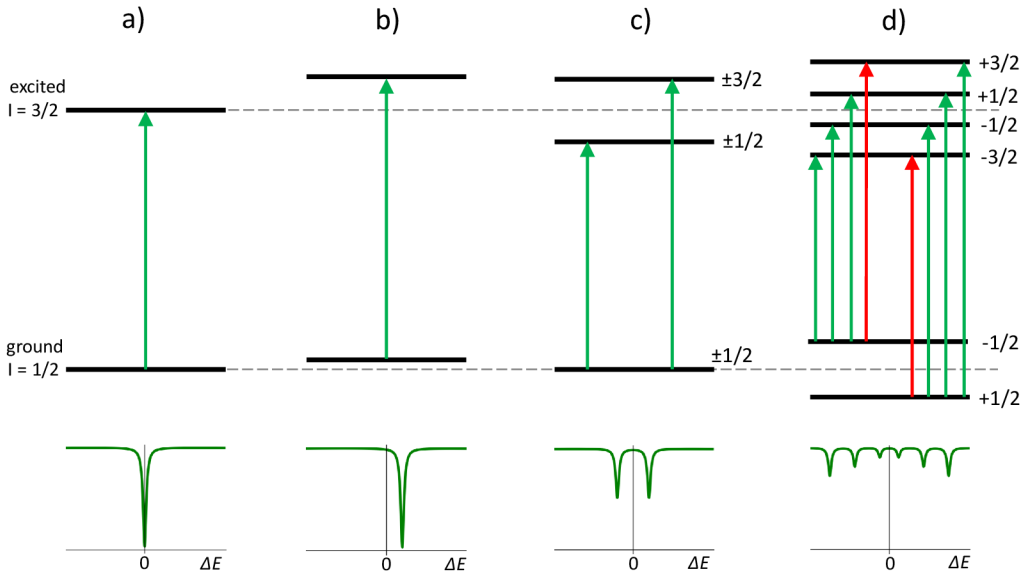

Figure 3: *Hyperfine interactions demonstrated on the ^{57}Fe isotope: no interaction, part a), Coulombic interaction (isomer shift), part b), quadrupole interaction, part c) and magnetic dipole interaction , part d). The upper parts show the shifts and splitting of the energy levels. The lower parts show the corresponding Mössbauer spectra. The red arrows mark the forbidden transitions and the numbers next to the energy levels label their magnetic numbers.*

1.1.3 Resonant Line Shape

This section is devoted to the shapes of the emission line, absorption line and the observed transmission spectrum because they are important for the coherent control of the gamma photons by means of the nuclear scattering. Let's consider the common transmission Mössbauer measurement, where the relative motion between the source and the absorber includes only the Doppler energy modulation (no high frequency vibrations). Each energy transition in the source and absorber is represented by a single emission and absorption line (component) and the final emission and absorption spectrum respectively is given by their sum.

The basic shape of the emission and absorption line in the energy domain is a Lorentzian function which results from the Fourier transform of the exponential decay of the excited state in the time domain. The equation for this function, which is normalised to the unit area, has the form

$$L(\omega) = \frac{1}{\pi} \frac{\frac{\Gamma_0}{2}}{(\omega - \omega_a)^2 + \left(\frac{\Gamma_0}{2}\right)^2}, \tag{1}$$

where ω_a is the energy (angular frequency) of the nuclear transition in an absorber and Γ_0 is the former mentioned natural linewidth of resonance in radians per second.

The experimentally observed shape of the transmission spectrum is, in general, given by a convolution of the emission and absorption spectra. Assuming an ideal Lorentzian single line radioactive source and absorber, the transmission spectrum has again a Lorentzian shape whose linewidth[2] is equal to $2\Gamma_0 = 0.194\,\mathrm{mm/s}$. This value represents the lowest theoretical limit, which is practically impossible to achieve. In

[2]The convolution of two Lorentz curves is Lorentzian, whose linewidth (FWHM) is given by the sum of the linewidths of the convolved curves.

practice, the thinnest observable lines have widths greater than 0.21 mm/s. This is due to three main factors: the distribution of the hyperfine parameters, imperfections in the Doppler energy modulation (Gaussian broadening) and the sample effective thickness.

In Mössbauer spectroscopy, the components are dominantly fitted by Lorentzian curves. However, this approach is based on the thin absorber approximation, which assumes only a single scattering. Such situation can hypothetically occur on the ideal single atomic layer absorber. In practice, with real absorbers the probability of a multiple scattering (repeated ensemble excitation and deexcitation) is always non-zero and becomes relevant for resonantly thick absorbers. Specifically, the absorption line has a higher amplitude and becomes wider as the effective thickness increases [2], see Figure 4.

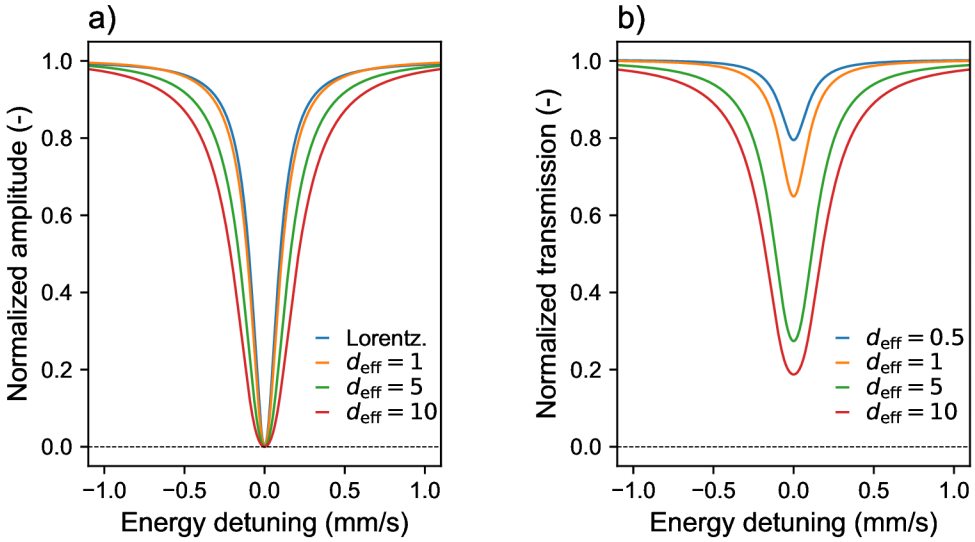

Figure 4: *Transmission integral lineshapes for different effective thicknesses. In part a), the shapes of the transmission integral normalised to the unit amplitude are compared with the Lorentzian curve. Part b) shows the dependence of the shape of the transmission integral on the effective thickness.*

The full analytical description of the transmission spectrum shape of the ideal single line source and absorber depends on the effective thickness and is described by the transmission integral which is defined by the relation

$$S_{\mathrm{tr}}(\omega_s) = \frac{1}{\pi}\int_{-\infty}^{\infty} \frac{\frac{\Gamma_0}{2}}{(\omega-\omega_s)^2 + \left(\frac{\Gamma_0}{2}\right)^2} \times \exp\left[-d_{\mathrm{eff}}\frac{\left(\frac{\Gamma_0}{2}\right)^2}{(\omega-\omega_a)^2 + \left(\frac{\Gamma_0}{2}\right)^2}\right] d\omega\,, \qquad (2)$$

where ω_s is the energy of the photons emitted from the source. The dimensionless parameter d_{eff} is the above mentioned effective thickness, sometimes called the resonant thickness, which can be defined [2, 50] in the form

$$d_{\mathrm{eff}} = \sigma_0 \eta f_{\mathrm{LM}} d\,, \qquad (3)$$

where σ_0 ($2.56{\cdot}10^6$ barns/atom) is the differential cross section of the nuclear resonant interaction, η is the number of Mössbauer nuclei per unit volume, f_{LM} is a Lamb-Mössbauer factor and d is the physical thickness of the absorber. In essence, the effective thickness expresses the probability of resonant scattering in the real absorber.

One of the simplest methods of determining the effective thickness of the absorber is to fit the transmission Mössbauer spectrum by the transmission integral.

For the coherent gamma radiation control, not only the exact knowledge but also the required values of the effective thickness may be desired. According to Equation 3, the effective thickness can be tuned primarily by changing the absorber thickness d and the number of Mössbauer nuclei per unit volume η. Due to the relatively low natural abundance of the iron Mössbauer nuclei, the most effective way to increase the effective thickness is to enrich the absorber with ^{57}Fe isotope.

1.2 Resonant Scattering in Harmonically Vibrating Absorber

Now assume a single line absorber that, unlike the standard Mössbauer spectroscopy experiment, vibrates harmonically, so that its position in time can be written as

$$z(t) = z_0 + R\sin\left(2\pi f t + \phi\right) , \tag{4}$$

where z_0 is the initial position, and R, f and ϕ describe the amplitude, frequency and phase of the vibrations respectively. For the further description, we define also the angular frequency of the vibrations $\Omega = 2\pi f$ and take into consideration that the vibration frequency is comparable to the reciprocal value of the decay lifetime (6.75 MHz for ^{57}Fe) and the amplitude is comparable to the gamma photon wavelength (86 pm for 14.41 keV). The impact of the absorber vibrations on gamma radiation scattering was comprehensively explained recently in the reference [20], despite the fact that the first experiments were conducted several decades earlier [12,13,17]. It was explained that the uniformly vibrating single line absorber sees the incident photon field like a structure of multiple absorption lines (spectral components) which are equidistantly spaced by the frequency Ω. As a result, the Mössbauer spectrum $S(\omega_s)$ of the vibrating absorber consists of the central component and several sidebands (peaks) that is described by the following equation

$$S(\omega_s) = \sum_{k=-\infty}^{\infty} J_k^2\left(p\right) S_k\left(\omega_s\right) , \tag{5}$$

where the ω_s is the energy of the incident gamma photons, k is an summation index, J_k is a Bessel function of the first kind and k-th order and p is an amplitude modulation index. The k-th spectral component $S_k\left(\omega_s\right)$ is described by the above mentioned transmission integral (Equation 2) with the additional line shift $k\Omega$ as follows

$$\begin{aligned} S_k(\omega_s) = \frac{1}{\pi}\int_{-\infty}^{\infty} \frac{\frac{\Gamma_0}{2}}{\left(\omega-\omega_s\right)^2 + \left(\frac{\Gamma_0}{2}\right)^2} \\ \times \exp\left[-d_{\text{eff}} \frac{\left(\frac{\Gamma_0}{2}\right)^2}{\left(\omega-\omega_a-k\Omega\right)^2 + \left(\frac{\Gamma_0}{2}\right)^2}\right] d\omega \, . \end{aligned} \tag{6}$$

In this, so-called coherent model [27], which assumes the uniform (homogeneous) vibrations of all nuclei, the amplitude of the n-th sideband is determined by the square of the Bessel function of the n-th order and argument p. This parameter is defined [20] by the relation

$$p = \frac{2\pi R}{\lambda} , \tag{7}$$

which relates the vibrations amplitude R to the gamma photon wavelength λ. The amplitudes of the spectral components, including the central one, vary according to the square values of the nth-order Bessel functions, which alternate as the p parameter increases. In this way, the individual components can be maximised but also suppressed to zero, see Figure 5 or measured spectra in [27]. Specifically for $p = 2.4$ the central component vanishes which is known as acoustically induced transparency [21]. The presented modulation of the spectral components in the energy domain by the

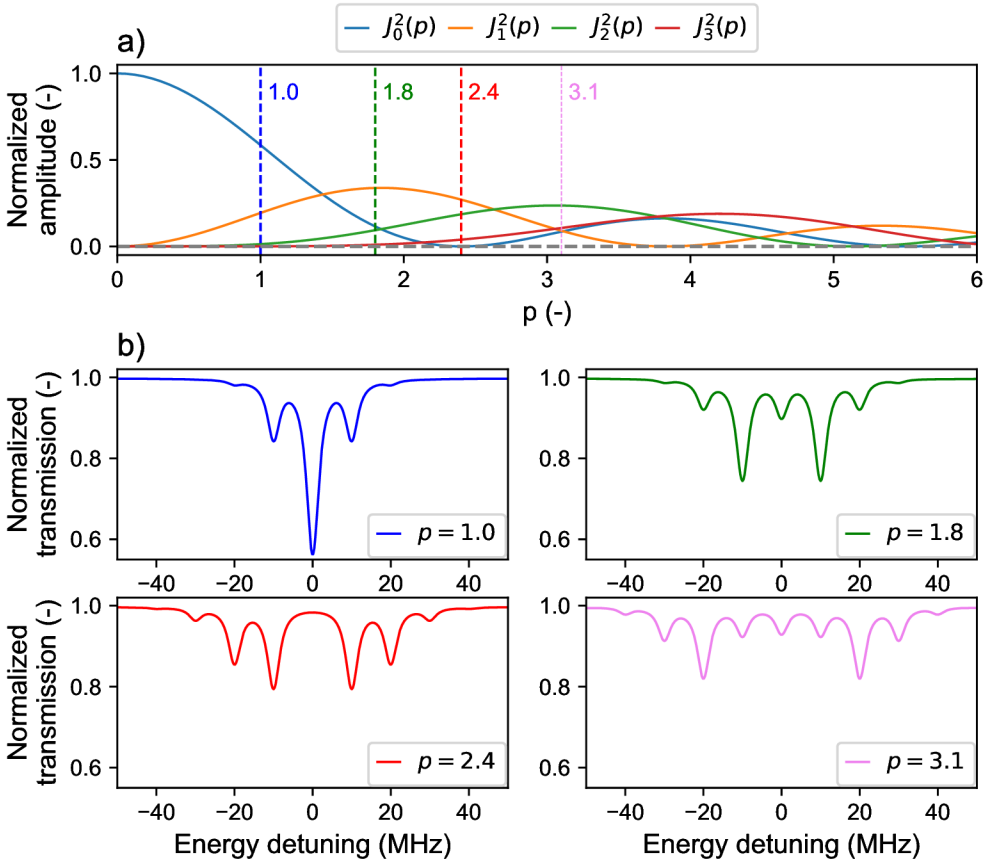

Figure 5: *Square values of Bessel functions of the first kind for the first four orders as a function of the modulation parameter p (vibrations amplitude), part a) and transmission Mössbauer spectra of the harmonically vibrating single line absorber calculated for the effective thickness $d_{eff} = 5$ and selected values of parameter p, part b).*

absorber vibrations has interesting consequences also in the time domain. In the paper [20], it is further explained that tuning the energy of the radioactive source to the first peak (sideband) leads to the generation of periodic gamma pulse intensity structure whose period is given by frequency of the vibrations and whose intensity exceeds the incident radiation level, see Figure 6. The increase in radiation intensity is explained by the phase matching of the spectral components, which results in the positive interference at the respective times. From a time domain point of view, the explanation for the positive interference resides in an additional phase shift which is introduced into the scattering process by the fast Doppler energy modulation caused by the uniform motion of the absorber during the excitation time. Note here that the dimensionless parameter p defined by Equation 7 can be interpreted as the phase shift, since we get the $p = 2\pi$ (one period phase shift) when $R = \lambda$. The harmon-

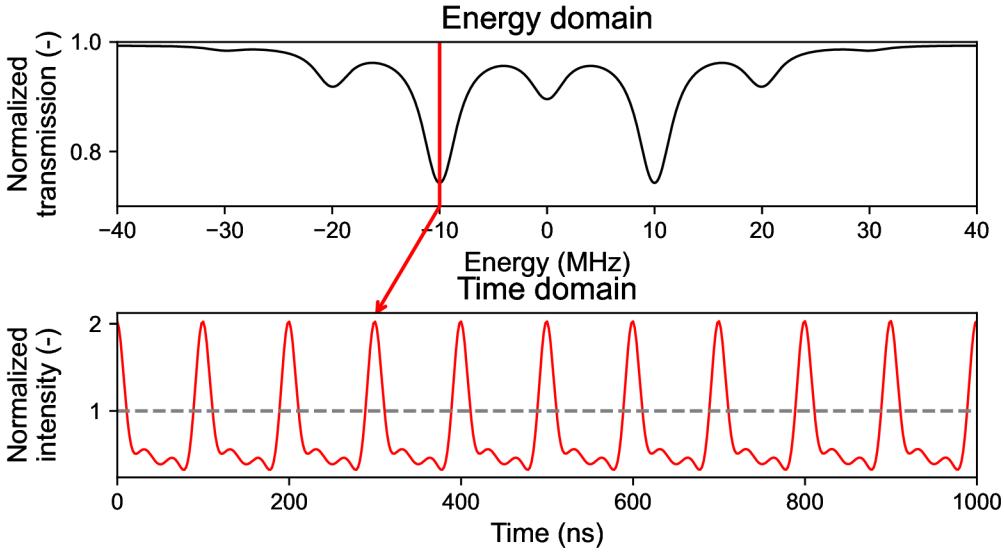

Figure 6: *The pulses of the gamma radiation intensity generated by the harmonically vibrating absorber (10 MHz) in the time domain. Tuning the energy to the first sideband ($\Delta E = \pm 10 MHz$) generates a single gamma pulses. The structure of gamma radiation is calculated for $p = 1.8$ when the intensity of the pulses and the first sideband are maximised. In this case, the scattered radiation exceeds the incident intensity by almost the factor of two.*

ically vibrating absorber can also be utilised also for the generation of double and triple pulse bunches by tuning the gamma photons energy to the second and the third sideband respectively [24–26]. However, the temporal properties of the gamma pulses in this concept can be modified only to a limited extent by changing the absorber characteristics, incident photon energy or frequency and amplitude of the vibrations. Specifically, the single vibration frequency cannot generate pulses narrower than about $1/(4f)$ [25], which determines the lowest positive duty cycle of about 25 %. Thus, the absolute pulse width can be reduced only if the repetition frequency f is increased. Furthermore, the intensity of the pulses reaches its maximum at certain vibrations amplitudes, e.g. the most intense single pulses are obtained for $p = 1.8$ pm, [20], and the shape of the pulses at the maximum intensity can be modified only in a limited way by absorber characteristics and energy detuning.

At the end of this section, we would like to point out that, with respect to the theoretical description of the interference phenomena induced by the vibrating absorber and the notation used in this field, it is more natural to express the energy in megahertz units and the amplitude of the vibrations by the dimensionless parameter p. Expressing the energy axis in frequency units makes it easier to match the energy of the source to the particular positions of the spectral sidebands. Similarly, the parameter p directly indicates the amplitudes of the spectral components and expresses the vibration amplitude as a phase shift. For this reason, the megahertz units are utilised in this work instead of in the Mössbauer spectroscopy conventional millimetres per second, and the parameter p is used instead of basic length units. The conversion relations between the mentioned units are the following: 1 mm/s = 11.615 MHz and $p = 1.0 = 13.694$ pm ($\lambda = 86$ pm).

1.3 Resonant Scattering in Multi-Tone Vibrating Absorber

One of the goals of the nuclear quantum optics is the generation of the narrow high-intensity pulses whose temporal properties could be easily controlled. For this reason, the improvement of the concept of the harmonically vibrating absorber is of interest. A recent theoretical work [51] predicts that the narrower gamma pulses of higher intensity can be obtained if the second harmonic frequency of appropriate amplitude and phase is added to the vibrational motion of the absorber. The additional intensity enhancement is explained by the synchronization of more spectral components which appear in the spectrum owing to the second harmonic. From another point of view, the interference result is influenced by adding the second frequency because it changes the absorber motion profile, which results in a different phase shift modulation of the scattered wave in time.

In the present work, we develop the idea of adding more harmonics, which allows the creation of more complicated periodical motion of the absorber. Taking into account the infinite series of harmonics, we get the Fourier series, which offers the possibility of assembling any arbitrary but still periodic motion profile, whose period is determined by the fundamental frequency. Each harmonic frequency in the absorber motion introduces two variables (amplitude and phase) that influence the temporal properties of the gamma pulses. The question is, what are the optimal amplitudes and phases of these harmonics – in other words – what is the optimal absorber motion profile for generating the high-intensity narrow pulses? The clue can be partially found in the publications regarding the study of the gamma echoes [14,16,18,23] and in the work describing the spectral narrowing of synchrotron radiation [9].

Gamma echo refers to a rapid increase in the radiation intensity that is observed in the decay of the ^{57}Fe excited state as a result of the step-like change in position of the single line absorber, which is tuned near the resonance. As in the case of the above mentioned harmonically vibrating absorber, the increase in intensity is explained by a positive interference which is caused by a rapid absorber jump. Similarly, in the experiment with the synchrotron radiation, the finite step-like motion with the amplitude $\lambda/2$, corresponding to the phase shift by π, resulted in the spectral redistribution of the radiation intensity into the resonance. This indicated that the required amplitudes and the phases of the individual harmonics for generation of the high-intensity pulses are those, which create the absorber motion profiles containing the fast jumps, e.g. a square or saw motion profile. Incidentally, this statement was confirmed by a theoretical work [52], which has been published while writing the present thesis.

Since the analytical description of the scattering in the multi-tone vibrating absorber was difficult to handle, we decided to solve it numerically. The calculation procedure of the gamma radiation intensity is described later in Subsection 1.3.1. Analysis of the numerical results proved that the step-like motion creates intensive single gamma pulses. Moreover, observation of the various simulations revealed that the concept of the multi-tone vibrating absorber can be further generalised to arbitrary control of the gamma radiation. It means that there can exist various motion profiles that create not only the single gamma pulses, but also the arbitrary structures containing the enhanced pulses and absorptions of different widths and amplitudes as well.

Since the palette of possible motion profiles is too broad and searching for the optimal ones would deserve a thorough analysis, we have focused only on the basic profiles such as triangle, square, trapezoid and bipolar pulse in this work. The ap-

plication of these motion profiles to gamma radiation intensity control and discussion of the corresponding results of the numerical simulations are presented in Subsection 1.3.2.

1.3.1 Numerical Calculations

For the numerical calculation of the gamma radiation intensity behind the multi-tone vibrating absorber, we assume the absorber motion in time $z(t)$ in the form

$$z(t) = z_0 + Rz'(t) = z_0 + R\sum_{k=1}^{K} B_k \sin\left(2\pi k f t + \phi_k\right) , \tag{8}$$

where z_0 is the absorber initial position, R defines the amplitude of the absorber maximum displacement and $z'(t)$ is the normalised shape of the absorber motion profile ($\max|z'(t)| = 1$), which is defined by the sum of the Fourier series. In it, K defines the number of harmonics, f is the fundamental frequency of the motion, B_k are the normalised amplitudes and ϕ_k are the phases of the k-th harmonic.

The gamma photon originating from the deexcitation of the first excited state is in the distance z from the radioactive source described as a quasi-monochromatic electromagnetic wave with electric intensity

$$\mathcal{E}(t) = \mathcal{E}_0\,\theta\left(t - t_0 - \frac{z}{c}\right) \times \exp\left[-\left(i\omega_0 + \frac{\Gamma_0}{2}\right)\left(t - t_0 - \frac{z}{c}\right) + i\varphi_0\right] , \tag{9}$$

where $\mathcal{E}_0$ is the normalisation constant whose value is equal to $\sqrt{\Gamma_0}$, θ is the Heaviside step function with argument $t - t_0 - \frac{z}{c}$ which describes the emission of the photon after time t_0 from the excited state origin, the fraction $\frac{z}{c}$ describes the time delay caused by the propagation of the photon through space, ω_0 is the transition energy in the radioactive source, φ_0 is an initial random phase and i is the imaginary unit. Note that the phase φ_0 can be neglected in the further description, because it plays role only in the multiple photon interference. In the case of nuclear resonant scattering, the single photons dominantly interfere in the scattering process and the result is independent of the initial phase of the incident photon.

Let's consider now that the gamma photon propagates towards the vibrating absorber and its energy is Doppler-modulated by the constant velocity motion of the source. The total relative movement of the source from the absorber view can be written as

$$z(t) = -z_0 + vt - Rz'(t) , \tag{10}$$

where v is the constant velocity of the source. Then the absorber sees the frequency modulated electric intensity $\mathcal{E}_m(t)$ in the form

$$\begin{aligned} \mathcal{E}_m(t) = \mathcal{E}_0\,\theta&\left(t - t_0 - \frac{z_0}{c} + \frac{vt}{c} - \frac{Rz'(t)}{c}\right) \\ \times \exp&\left[-\left(i\omega_0 + \frac{\Gamma_0}{2}\right)\left(t - t_0 - \frac{z_0}{c} + \frac{vt}{c} - \frac{Rz'(t)}{c}\right)\right] . \end{aligned} \tag{11}$$

In this equation, we can neglect the expression z_0/c, since it causes an irrelevant constant time delay and the corresponding phase shift. In the same way, any disturbing mechanical vibrations can be neglected due to their low frequency (in comparison

with absorber vibrations) even though, in practice, they can change the distance z_0 by several micrometres. In the argument of the Heaviside function, all parameters except t_0 can be neglected because their effect is eleven and more orders of magnitude lower.

In the exponential, the expression vt/c can be recognised as the constant velocity Doppler energy modulation $\Delta E = \frac{v}{c}\omega_0$ provided by the transducer. Since the term $\Gamma_0/2$ is thirteen orders of magnitude lower than ω_0, the multiplication with the exponential decay can be neglected and the exponent can be simplified by merging the energy modulation with ω_0 into $\omega_s = \omega_0 + \Delta E$. Next, the expression $Rz'(t)/c$ describes the effect of the high-frequency multi-tone vibrations, which basically also perform the Doppler energy modulation, but five orders of magnitude faster than the transducer. In order to replace the maximum vibration displacement R by the parameter p, the expression can be rewritten using the emitted photon energy ω_s as follows

$$\frac{R}{c} z'(t) = \frac{p}{w_s} z'(t)\,. \tag{12}$$

Taking into account the above mentioned adjustments, the modulated electric intensity can be expressed in the form

$$\mathcal{E}_m(t) = \mathcal{E}_0\, \theta\,(t - t_0) \times \exp\left[- \left(i\omega_s + \frac{\Gamma_0}{2} \right) \left(t - t_0 - \frac{pz'(t)}{\omega_s} \right) \right]\,. \tag{13}$$

Note here that from the absorber reference frame, the situation when the electric intensity is modulated by the motion of either the absorber or the radioactive source is equivalent, because the relative motion between the source and the absorber is important. Thus, the high frequency modulation can be performed also by the radioactive source. However, in the laboratory reference frame it has to be ensured that the source moves in the opposite direction than the absorber in order to induce the same effects.

The photon field $\mathcal{E}_m(t)$ interacts with the absorber, which is described in the energy domain by the absorption function $\tilde{A}(w)$. Unlike the transmission integral, in the numerical calculations, this function has to be expressed in the complex form in order to capture the imaginary part. The complex single Lorentzian absorber is described as follows

$$\tilde{A}(w) = \frac{i\frac{\Gamma_0}{2}}{(\omega - \omega_0 - \delta) + i\frac{\Gamma_0}{2}}\,, \tag{14}$$

where δ is the shift of the centre of the absorption function with respect to the source emission line. For the needs of the experiments, we consider a more complicated model of magnetically split absorber, whose absorption function is given by the sum of the six lines

$$\tilde{A}(w) = \sum_{n=1}^{6} A_n \frac{i\frac{\Gamma_0}{2}}{(\omega - \omega_0 - \delta - \Delta\omega_{m,n}) + i\frac{\Gamma_0}{2}}\,, \tag{15}$$

where $A_n = \frac{3}{12}, \frac{2}{12}, \frac{1}{12}, \frac{1}{12}, \frac{2}{12}, \frac{3}{12}$ for $n = 1, \ldots, 6$ are the normalised amplitudes of the sextet lines and the term $\omega_0 - \delta - \Delta\omega_{m,n}$ defines their energies. The expression $\Delta\omega_{m,n}$ depends on the hyperfine magnetic field B_{hf} and determines the energy shifts induced by magnetic interaction. The calculation of $\Delta\omega_{m,n}$ values can be found in Appendix (function "magnetic_splitting") or can be derived from the literature [2, 37] by subtracting the corresponding excited and ground state energy levels.

The procedure of the numerical calculation of the output intensity is similar to the analytical derivation of the transmission integral. The electric intensity $\mathcal{E}_m(t)$ of

the incident photon field is transformed into the energy domain by the fast Fourier transform (FFT). Subsequently, the scattering process is performed by multiplying the energy domain of the photon field $\tilde{\mathcal{E}}_m(\omega)$ and the absorption function $\tilde{A}(w)$ according to the equation

$$\tilde{\mathcal{E}}_{\mathrm{out}}(w) = \tilde{\mathcal{E}}_m(\omega) \times \exp\left(-\frac{d_{\mathrm{eff}}}{2}\tilde{A}(w)\right) , \tag{16}$$

where the effective thickness of the absorber plays an important role. The scattered output wave $\tilde{E}_{out}(w)$ is subsequently transformed back into the time domain by inverse FFT. The experimentally measurable radiation intensity $I_{\mathrm{out}}(t)$ is then obtained as a modulus of the output electric intensity $\mathcal{E}_{out}(t)$ using the complex conjugate

$$I_{\mathrm{out}}(t) = E_{\mathrm{out}}(t)E^*_{\mathrm{out}}(t) = \mid E_{\mathrm{out}}(t) \mid^2 . \tag{17}$$

However, this is not the end because the calculation was performed for a specific value of t_0. Since we are interested in the radiation intensity measured with respect to the absorber motion profile, the random nature of the radioactive decay has to be considered. Deexcitation at time t_0 after the excited state origin has an exponential distribution, but the excited state originates at random times, so the resultant distribution of the parameter t_0 is uniform, corresponding to the random process. For this reason, the resultant experimentally observable gamma radiation intensity, which we label the normalised radiation intensity $I(t)$, is given by integral

$$I(t) = \int_{-\infty}^{\infty} I_{\mathrm{out}}(t, t_0)\, dt_0 . \tag{18}$$

The normalised intensity $I(t)$ depends on several parameters which come from Equation 8, 13 and 15. Since these parameters will be discussed later in Section 3.3, which is devoted to the fitting the experimental data, their overview is provided in Table 1.

The linewidth of the emission Γ_s and absorption Γ_a line is intentionally listed separately because the natural linewidth Γ_0 is not always used. For experimental data fitting, when the precise parameters of the absorber or especially the source are unknown, the linewidths may be slightly increased to describe the line broadening [21]. For example, $\Gamma_s = 1.2\Gamma_0$ is considered in our experiments and the same approach can be used also for the absorber linewidth.

Since only a single line absorber is used in this work, it is advantageous to relate the Doppler energy modulation ΔE to the spectrum shift δ. In this way, both parameters can be merged in ΔE, which hereafter has the meaning of the energy detuning from the resonance. This step helps to simplify the description of the energy detuning of gamma photons in simulations and experiments.

The calculation procedure was implemented in Python and the optimised script to simulate the normalized intensity waveforms $I(t)$ is available with comments in Appendix. Since the numerical simulation works with a finite time resolution in units or tenths of nanoseconds, the real angular frequency $w_s = 3.49 \times 10^{18}$ rad/s is too high to be used due to the sampling theorem. The maximum numerical angular frequency range $\Delta\omega$ of the simulation is determined by the time resolution dt according to the relation $\Delta\omega = 2\pi/dt$ which gives a maximum angular frequency range 3.14×10^9 rad/s (500 MHz) for 2 ns time resolution. For that reason, the lower angular frequency w_s, specifically the value equal to half of $\Delta\omega$, i.e $w_s = \pi/dt$, which fulfils the condition of the sampling theorem, is used in the calculation.

Origin:	Parameter:	Description:
Absorber motion Eq: 8	p	Vibrations amplitude
	f	Vibrations frequency
	B_k	Fourier series amplitudes of the absorber motion profile
	ϕ_k	Fourier series phases of the absorber motion profile
	K	Number of harmonics in the Fourier series
Doppler energy modulation	ΔE	Transducer Doppler energy modulation
Source Eq: 13	Γ_0 (Γ_s)	Emission linewidth of the source
	ω_s	Wavelength of the emitted photon
Absorber Eq: 15	Γ_0 (Γ_a)	Absorption linewidth of the absorber
	δ	Shift of the absorber resonant relative to the source
	B_{hf}	Natural emission linewidth of the source
	d_{eff}	Effective thickness

Table 1: Parameters of the normalised intensity function $I(t)$.

Another numerical aspect is the determination of the finite integration limits for t_0. It was experimentally verified that the sufficient integration interval is from -0.5 μs to the required time length of the simulation, i.e. for the time length $\langle 0, t_1 \rangle$ the t_0 should be integrated at least in the range $\langle -0.5, t_1 \rangle$. Going further into the past does not improve the simulation results. Nevertheless, some numerical artefacts still occur in the first approximately 350 ns. We were unable to identify the cause of these artefacts, so we simply cut this region out when fitting the experimental data.

1.3.2 Simulations

In this subsection, we demonstrate the potential of the multi-tone vibrating absorber to control the temporal properties of the gamma radiation intensity by four different velocity profiles: triangle, trapezoid, square and bipolar pulse. For the simulations shown here, we take into account the single line absorber ($B_{\mathrm{hf}} = 0$), the radioactive source with $\Gamma_s = \Gamma_a = \Gamma_0$ and the effective thickness of the absorber $d_{\mathrm{eff}} = 10$ (equivalent of about 30 μm thick stainless steel foil). The energy detuning ΔE and the parameters influencing the absorber motion profile, i.e. p and K, are varied. The fundamental frequency f, which controls the period of the radiation intensity pattern, is chosen at either 1 MHz or 2 MHz. For practical reasons, we further describe the motion amplitude by the maximum span of the absorber position $\Delta p = \max[z(t)] - \min[z(t)]$ when $\Delta p = 2p$ applies for all profiles symmetrical along the time axis.

Triangular Motion: First, the triangular motion profile is presented because it provides an empirical view on the scattering in the vibrating absorber. The triangular profile actually means the constant velocity Doppler energy modulation. However, if the change in the absorber position is fast enough, i.e. comparable to the excited state lifetime, the oscillations in the intensity waveform occur instead of the two constant levels, see Figure 7. Especially in the times when the absorber turns the direction of motion, i.e. the Doppler energy modulation changes rapidly, the spikes in intensity appear. It clearly demonstrates additional interference effects caused by the fast change of the Doppler energy modulation within the excitation time.

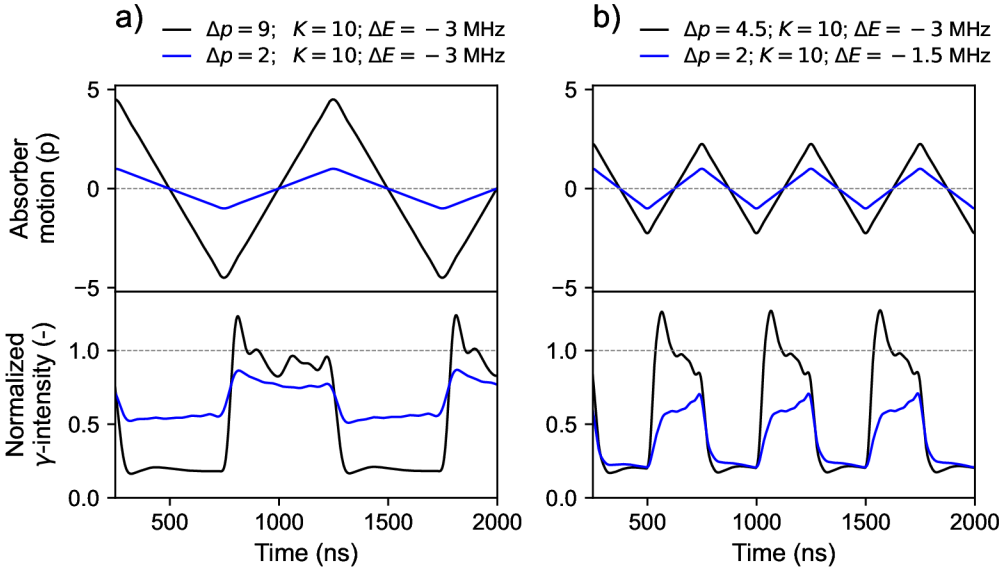

Figure 7: *Radiation intensity waveforms controlled by a triangular motion profile with fundamental frequency 1 MHz, part a), and 2 MHz, part b). The highest deviations from the two constant levels occur when the Doppler modulation rapidly changes when the absorber turns the direction of its motion.*

Trapezoidal Motion: The fast jump of the absorber, which allows to create the high-intensity pulses, is demonstrated on the trapezoidal motion profile. This shape is derived from the unit step function based on the requirement to return slowly back to the initial position. The optimum velocity profile according to reference [52], i.e, saw, was not tested because visually it seemed that it does not provide any significant improvement in the comparison to the trapezoid. However, it might generate a bit narrower and intense pulses.

The intensity of the pulses generated by the trapezoidal profile depends on the energy detuning and the height of the absorber jump Δp. The width of the pulses is approximately proportional to the time of the jump. Thus, the infinite jump might seem to be the best option for generating the pulses of desired qualities but this is not the truth, see the results of simulations in Figure 8. The highest intensity (≈ 3.5) and, simultaneously, the narrowest width (≈ 8 ns) of the single pulses were observed for the fast finite jumps with $\Delta p \approx 6.28$, i.e. 2π. Unlike this, the infinite jump provided the highest intensity for $\Delta p = \pi$ and no pulse was created for $\Delta p = 2\pi$. For higher jumps ($\Delta p > 6.3$) the increase in intensity moderates and more than one pulse emerges.

Furthermore, the pulse shape and the maximum intensity also depend significantly on the effective thickness, but the investigation of the impact of this parameter was beyond the scope of this work.

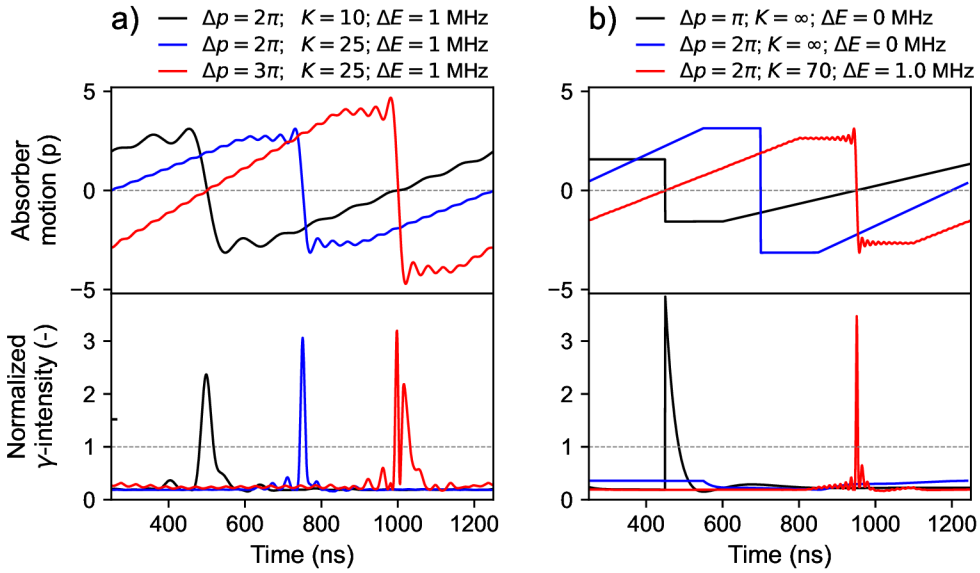

Figure 8: *Radiation intensity waveforms controlled by a trapezoidal motion profile with a fundamental frequency 1 MHz. The influence of the number of harmonics and vibrations amplitude on the pulse shape generated by finite jump is demonstrated in part a) and comparison of finite and infinite step jump ($K = \infty$) is shown in part b).*

Along with the trapezoidal motion profile, the energy detuning of the incident photons has to be also properly adjusted in order to generate the well-shaped pulses, which ideally consist of the constant absorption and narrow high intensity peaks. To reach this, the optimal energy detuning is slightly out of the resonance (0.5–2.0 MHz). The sign of the detuning depends on the direction of the absorber jump, which has to Doppler-modulate the energy further out of the resonance. The necessity to tune the energy on the correct side of the resonant line is related to the discovered general symmetry where altering the sign of the energy detuning and the direction of the absorber motion results in the same radiation intensity

$$I(t, \Delta E, z'(t)) = I(t, -\Delta E, -z'(t))\,, \tag{19}$$

see Figure 9, part a).

Thinking about the scattering in the vibrating absorber in terms of the fast Doppler energy modulation gives an indication on how to find the conditions for the short-time acoustically induced absorption. This is feasible if the energy of the incident photons is set further away from the resonance and the velocity of the absorber jump turns the energy modulation to the resonance and back, see the simulation results in Figure 9, part b). Thus the absorption can be induced for only several tens of nanoseconds.

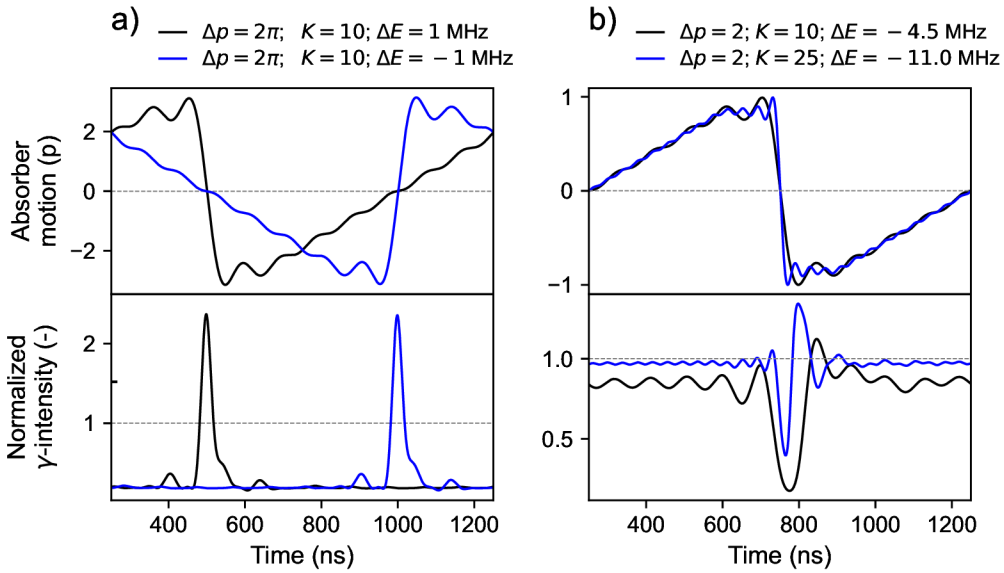

Figure 9: *Demonstration of the symmetry of energy detuning and absorber motion direction, part a), and short time acoustically induced absorption, part b).*

Square Motion: The fast jumps in the square velocity profile can be used to easily double the frequency of the single gamma pulses. However, in order to create the symmetrical pulses on both the rising and falling edges, it is necessary to tune the energy precisely to the resonance, see the Figure 10.

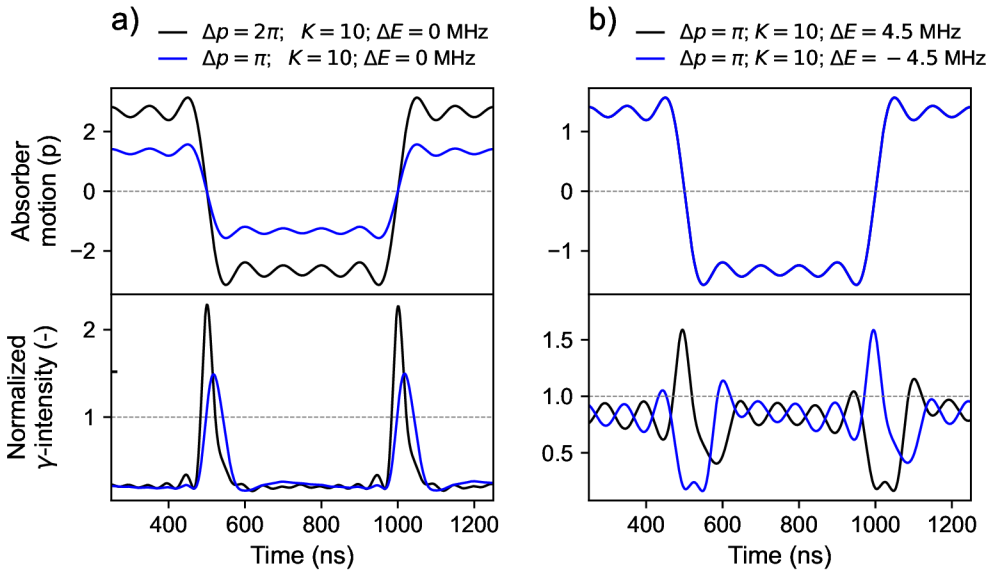

Figure 10: *Radiation intensity control by a square motion profile. Both, rising and falling edges of the profile allow easily double the frequency of the pulses, part a), but when detuned out of the resonance, one edge creates pulses and another induces the absorption, part b).*

Bipolar Pulse Motion: The last investigated profile, called the bipolar pulse, consists of the harmonics with equal amplitudes and zero phases. This profile is of interest because it allows the generation of either single or double gamma pulses in dependence on tuning the energy of the incident photons to the left or right side of the resonance, see Figure 11. The nature of this phenomenon remains unexplained.

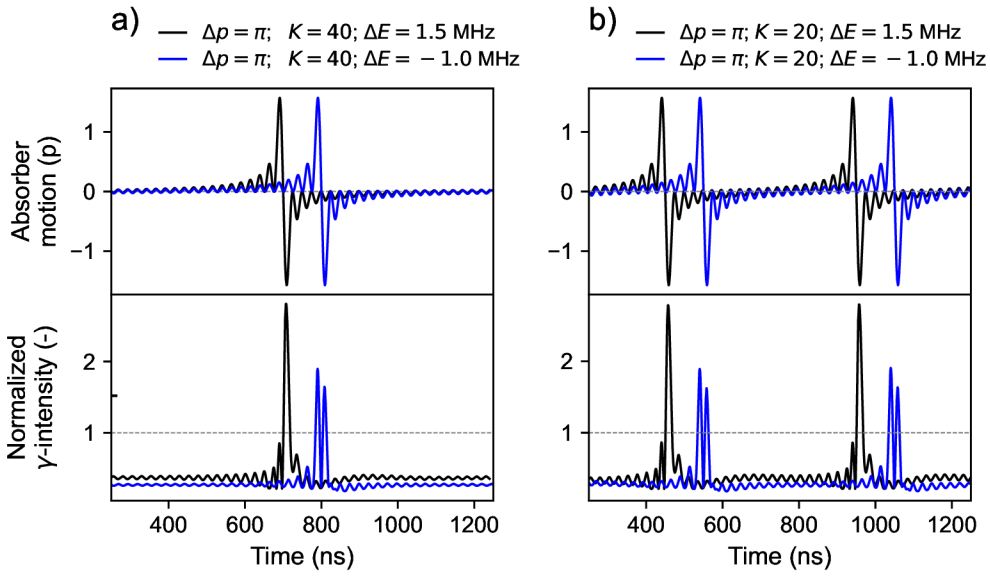

Figure 11: *Generation of single or double gamma pulses by a bipolar pulse shaped motion profile with a fundamental frequency 1 MHz, part a) and 2 MHz, part b).*

The presented simulations show that the multi-tone vibrations allow to control the temporal properties of the gamma radiation in a much broader way than a simple frequency vibrations. The period of the pulses can be tuned while maintaining their width, which can be adjusted by the low-to-high time of the absorber jump. Under certain conditions, the output intensity can exceed more than three times the incident intensity and the pulse width can be narrowed to a few nanoseconds. In addition, the intensity waveforms may be shaped in various ways by changing the energy detuning and the absorber motion profile.

2 Experimental Equipment

The nuclear quantum experiments described in the previous chapter require specific equipment. In addition to the sufficiently fast piezotransducers to vibrate the absorber at high frequencies, a DAQ system combining the functionality of the Mössbauer spectrometer and a time-tag is necessary. As the area of nuclear quantum optics is relatively new, it is not possible to purchase specialised equipment for this purpose. One possibility is to assemble the DAQ system from many general-purpose modules (e.g. from Ortec) [18, 20, 25]. However, assembling and setting up such a system is time-consuming and changing its functionality is complicated. Therefore, we have developed our own system based on the Mössbauer spectrometer that has been developed at our department in recent years [53, 54]. Specifically, the firmware and software of the spectrometer has been upgraded in order to develop a compact, purpose-built DAQ system for nuclear quantum experiments in general, which provides data processed on the hardware level.

Furthermore, this chapter describes the creation of the piezotransducer and the piezodriver, which provide the low-amplitude, high-frequency motion of the Mössbauer absorber. Driving the piezotransducers at high frequencies has to deal with the low impedance caused by the capacitive nature of the piezoelements. Utilising a standard arbitrary function generator with 50 Ω output impedance and maximum output voltage ±10 V for direct driving of piezotransducers may be insufficient because only a fraction of the output voltage is applied due to the voltage drop on the output impedance. This is one of the reasons why a purpose-built, high-frequency piezodriver with low output impedance was developed specifically for our experiments

2.1 Mössbauer Spectrometer for Nuclear Quantum Experiments

The aforementioned upgraded Mössbauer spectrometer as a whole is properly described in the author's paper [55]. The scope of this section is only the description of the spectrometer improvements regarding the signal processing for the time measurements, because the fully-fledged Mössbauer spectrometer was developed as a part of the author's previous theses [53, 54]. Nevertheless the basic operating principles of the spectrometer are briefly described in following two paragraphs in order to understand the context of the improvements.

The spectrometer was designed as a compact purpose-built electronic circuit board that offers two independent channels. These enable to drive two loudspeaker-based transducers [56, 57] and acquire two Mössbauer spectra simultaneously. This dual-channel spectrometer is based on an FPGA and a 32-bit microcontroller (MCU) where the FPGA processes two independent signals from the detectors and the MCU is responsible for the rest of the spectrometer functions such as peripherals setting, analog-to-digital and digital-to-analog conversions, data management and communication with the controlling computer, see the spectrometer diagram in Figure 12.

The control of the transducer velocity profiles (Doppler energy modulation) is ensured by the auto-tuning procedure [58] which continuously updates the currents in the excitation coils based on the transducer velocities measured by the pick-up coils. Signals from individual detectors (pulse-shaped) are processed by three comparators with different voltage levels, the baseline (BL), lower level (LL), and upper level (UL). The comparator outputs, which carry the information about the pulse shape, are

subsequently analysed by the pulse shape discriminator (PSD) [54, 59] implemented in the FPGA. The PSD carries out the amplitude and time length discrimination and increments the particular counter if the pulse is valid. The MCU reads out the FPGA counters 2048 times within the transducer motion period and thus sorts the counts into channels of spectra with respect to the Doppler energy modulation. Next, the MCU exchange the data with the controlling computer periodically after adjusted number of the transducer motion periods. For example, typically used 300 periods give the data sending period of 15 s for 20 Hz transducer frequency. The computer sends the commands and the excitation waveforms for the transducers into the MCU and receives measured data, i.e. Mössbauer spectra and velocities of the transducers.

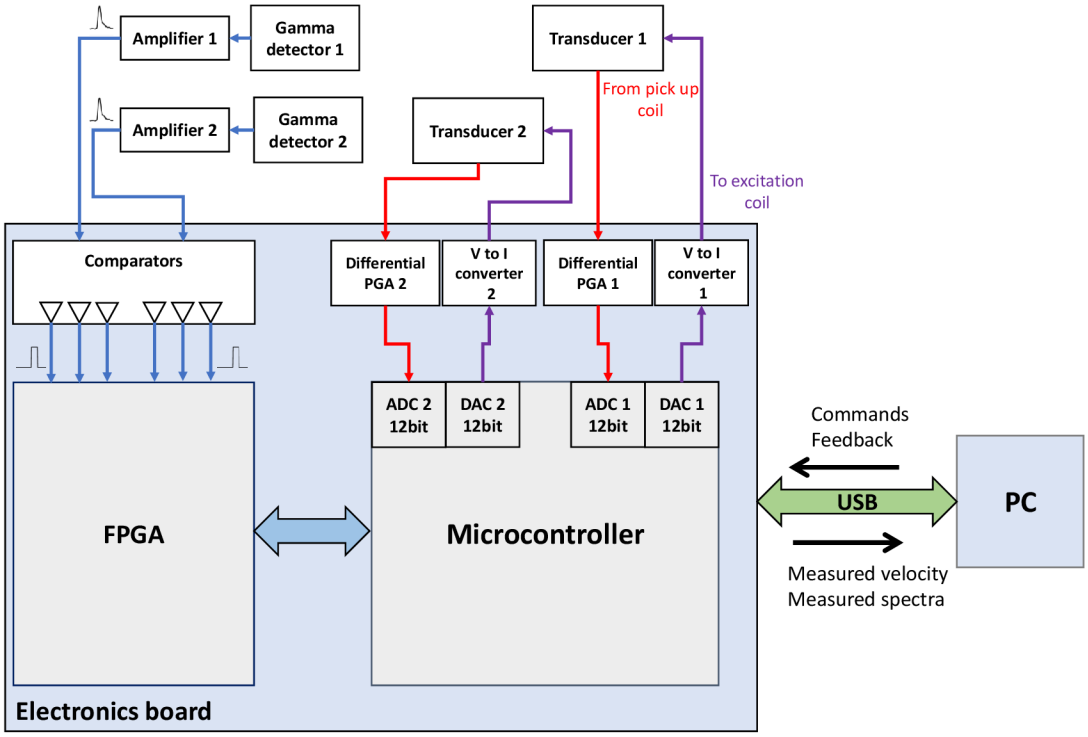

Figure 12: *Diagram of the dual Mössbauer spectrometer. Abbreviations: ADC – analog-to-digital converter, DAC – digital-to-analog converter, PGA – programmable gain amplifier.*

For nuclear quantum experiments, it is essential to analyse the gamma radiation not only in the energy domain, but mainly in the time domain. For this reason, an upgrade of the spectrometer involved the implementation of the time-to-digital converter (TDC), asynchronous amplitude discriminator (AAD) and asynchronous delay lines, which are described in detail in the following subsections. These components are necessary to perform the required time-of-flight measurements on two separated inputs between the pulses having the demanded amplitude. To avoid the hardware modifications, the required components (entities) were implemented on the level of the FPGA firmware. The diagram of the signal processing in the FPGA with upgrade highlighted is shown in Figure 13.

The input analog signal from the detector or another device (e.g. function generator) on each channel is digitised by three comparators. Two comparators ,UL and

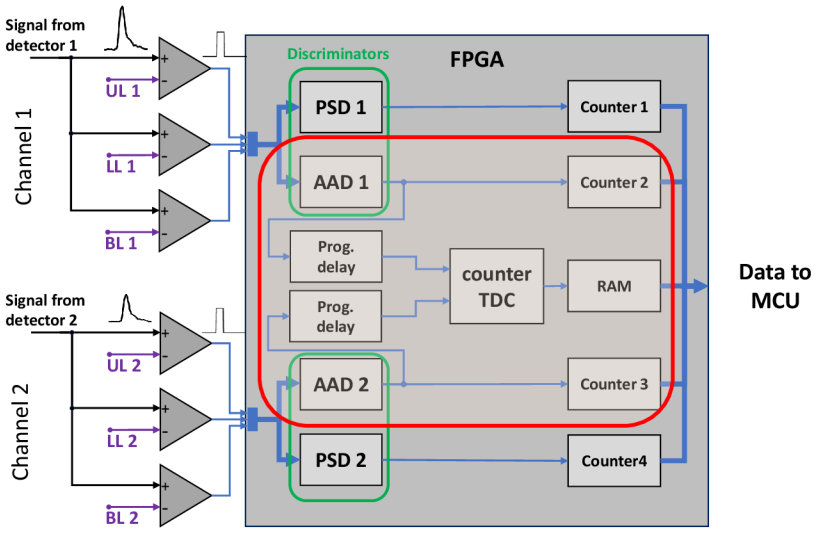

Figure 13: *Diagram of the signal processing in the FPGA. Red line encircles the newly developed parts for the nuclear quantum experiments. Abbreviations: PSD – pulse shape discriminator, AAD – asynchronous amplitude discriminator, TDC – time-to-digital converter.*

LL, define the amplitude discrimination window, the third comparator, BL, is used to determine the time of flight by the leading edge timing method[3] [60]. The outputs of the comparators, which carry the information about the pulse amplitude, time of flight and pulse length, are analysed by discriminators (AADs and PSDs) in the FPGA. A detailed description of the PSD function can be found in [54] and now will be omitted here because it is used exclusively in standard Mössbauer measurements, which are not in the scope of this work.

The AAD performs an amplitude discrimination which, due to its asynchronous design, retains the information about the time of flight. More detail description of the AAD is provided in the following subsection. The outputs of the AADs can be used also for common Mössbauer spectra measurements, but are mainly utilised to generate the time stamps for the time measurements. The output pulses from the AADs are additionally delayed by programmable asynchronous delay lines before entering the TDC.

A time measurement in the TDC is started by the pulse from the AAD on the first channel (start pulse) and stopped by the pulse from the AAD on the second channel (stop pulse). Specifically, the time interval is always measured between the latest start pulse and the first subsequent stop pulse. Other stop pulses are ignored. As the time interval is measured, the result is stored in the in-built FPGA RAM. The measuring range of the time intervals is either 1024 ns with 250 ps, or 2002 ns with 500 ps resolution. This is sufficient for measuring nuclear excited state lifetimes in the nanosecond range or gamma experiments with piezotransducers vibrating in the megahertz range.

[3]For most of our nuclear quantum experiments, the leading edge timing was sufficient. If constant fraction discriminators are required, the external ones have to be used and connected to the spectrometer.

The spectrometer offers the acquisition of two time histograms, when each of which can be measured for different phase of the Doppler velocity modulation. This allows individual histograms to be measured for a different energy detuning in the constant velocity regime. In addition, reading of the FPGA RAM for each channel of the Mössbauer spectrum (2048 times within the transducer motion period) allows to acquire, besides the normal Mössbauer spectra or time measurements, also the time-differential Mössbauer spectra (TDMS) [55, 61], which require sorting of the detected pulses with respect to the time of flight and the energy modulation simultaneously.

The signal processing on the hardware level allows the spectrometer to easily switch between three basic operational modes which offer: Mössbauer spectra measurements, time measurements and time-differential Mössbauer spectroscopy. As a result, different types of experiments can be performed without the complexity of connecting many devices or modules.

2.1.1 Asynchronous Amplitude Discriminator

The main tasks of the AAD is to recognise whether the incoming pulse has the required amplitude and then to generate the pulse which preserves the information about the time of flight. This requires first obtaining information about the amplitude of the analysed pulse. Due to causality, we cannot predict what the amplitude of the pulse will be in the future, so immediate amplitude evaluation at pulse arrival is impossible. Optimally, the amplitude should be evaluated after the time when the pulse has already reached its maximum. Additionally, in order to keep the information about the time of flight (given by the rising edge on the BL comparator), it is necessary to evaluate the amplitude always after the constant time from the pulse arrival.

The requirements mentioned above determine the design of the AAD which has to contain asynchronous logic, which is challenging to implement in the FPGA. For this reason, the crucial part of the discriminator is a programmable asynchronous delay line which ensures a constant delay of the signal from the BL comparator. This entity is described in detail in Subsection 2.1.2. The AAD generates the pulse on its output on the rising edge of the signal from the BL comparator delayed by a time τ (hereafter evaluation delay) provided that the input pulse has the required amplitude (crossed LL but did not reach UL). This is also shown graphically in Figure 14, where the operation of the AAD is demonstrated on an example analysis of three pulses.

Since the shape (mainly the slope) of the pulse may be different, it is necessary to adjust the evaluation delay τ to the signal. For this reason, the delay line was designed to be programmable, offering a delay adjustment in 256 steps in the range from 2 ns to approximately 140 ns. For example, in the experiments presented in this work, where the YAP:Ce scintillation detectors are used with purpose-built amplifiers [53], we usually have the pulses that have a low-to-high time from 5 to 40 ns, depending on the amplifier gain. Therefore, the evaluation delay range of 140 ns is sufficient, since the steeper rising edges are typically desired for the time measurements.

The discriminator consists of the logic elements that perform the amplitude evaluation, output pulse generation and reset. An equivalent schematic of the AAD is shown in Figure 15. The validity of the pulse amplitude is continuously updated by the output state of a triad D flip-flops, which latch the crossing of certain comparator levels until the delayed BL signal makes the final decision and generates (or not) the output pulse. After the amplitude evaluation, a reset procedure starts. The procedure takes 20 ns after each analysed pulse and represents the dead time of the discriminator.

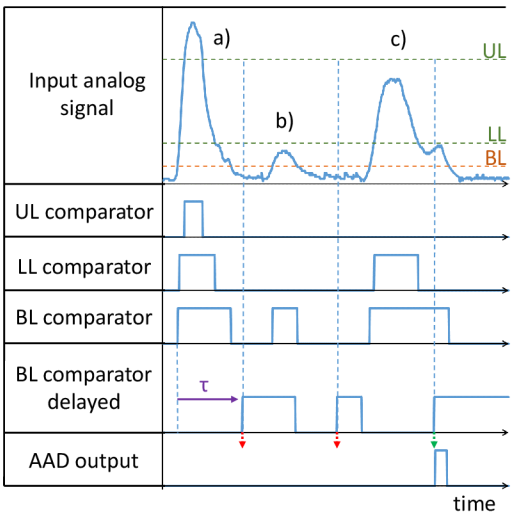

Figure 14: *Timing diagram of AAD illustrating its function on analysis of three pulses a-c). Pulse a) and b) have to high and too low amplitude respectively. Pulse c) has required amplitude so the AAD generates output pulse on the rising edge of delayed output from the BL comparator.*

Such a small dead time, given by the number of the D flip-flops in the reset part, can usually be neglected in the experiments with scintillation detectors where the pulse length is typically in the range of hundreds of nanoseconds. On the other hand, the dead time should be considered when setting the BL level. If it is set too low, the discriminator may be saturated with many noise pulses and a significant amount of the desired signal may be omitted.

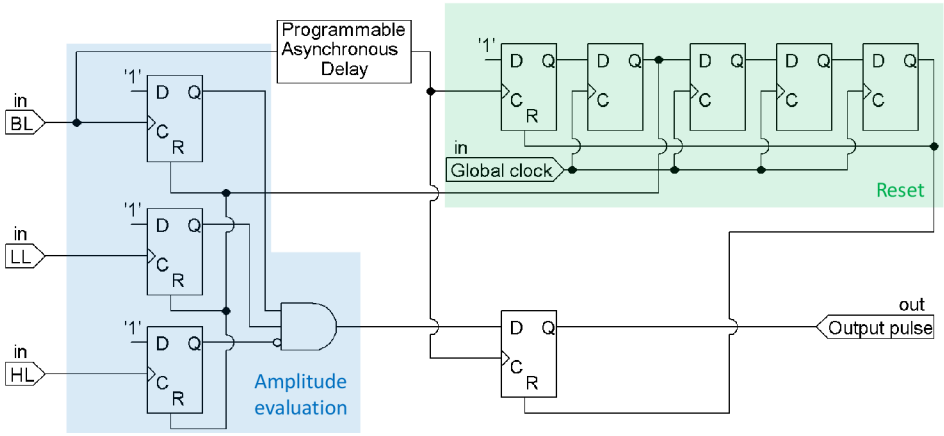

Figure 15: *Equivalent schematic of the AAD. Symbol '1' labels logic high.*

The maximum throughput of the AAD depends on the total pulse analysis time, which consists of the evaluation delay and the dead time. Therefore, the maximum countrate[4], which the AAD is able reliably process, ranges from 6.25 MHz ($\tau_{\max}$ = 140 ns) to almost 45 MHz ($\tau_{\min}$ = 2 ns) depending on the evaluation delay settings.

[4]For the countrate test a square-wave signal with 50 % duty cycle was used.

2.1.2 Programmable Asynchronous Delay Line

Basically, the delay lines can be divided into analog and digital, or blocking and non-blocking[5]. For our purpose, we are interested only in non-blocking digital delay lines since we need to delay two level i.e. digital signals (logic '1' or '0') without dead time. Such delays are typically realized by the signal propagating through a cascade of electrical components, e.g. RC networks or gates and often can be got as application specific integrated circuit (ASIC) [62]. In our case, however, an aim was to implement the delay line in the FPGA.

Concept of the FPGA delay lines has been developed in the last decade especially for implementation of the TDCs with tens of picoseconds resolution [63, 64]. These delay lines are based on asynchronous propagation of the signals through carry chains[6] or look-up tables (LUTs) [65]. Inspired by the literature, we developed our digital non-blocking delay line [66]. Based on it, the programmable digital delay line was implemented in the Mössbauer spectrometer.

The signal delay is generated by its propagation through the line of LUTs organised in several stages. Each stage contains a different number of LUTs, which is given by a power of two, so that the resultant delay is programmable by redirecting the signal into selected blocks via multiplexers, see the delay line schematic in Figure 16. Thus, the delay can be adjusted in 2^N levels where N is a number of stages.

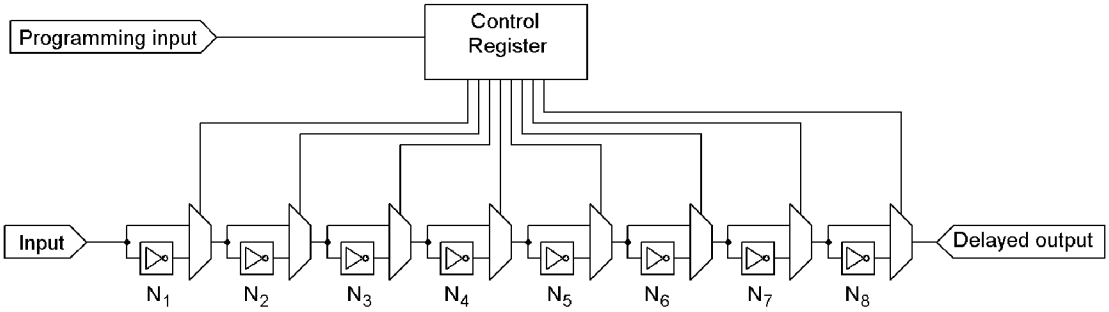

Figure 16: *Schematic of the eight-stage programmable asynchronous delay line. Each stage contains a delay with the different number of LUTs* N_1, N_2, ...,N_8.

In total, there are four programmable asynchronous delay lines in the spectrometer. Two are utilised in the AADs to set the evaluation delays and the other two serve for additional delaying of the output signals from the AADs before they enter the TDC. Except for the delay line on the channel 1 (start line), the rest three delay lines have the same parameters. They offer the delay from approximately 2 ns (intrinsic delay) up to approximately 140 ns adjustable in 256 steps (0.54 ns resolution). Specifically, there are 8 stages consisting of 2, 4, 8, ... , 128, 256 LUTs (510 LUTs in total). On the start line, the additional delaying has the meaning only if the signal from the detector on the stop line generates the output signal with an unwanted delay which can be caused by, for example, a longer transition time in the photomultiplier.

[5]Non-blocking delay lines are those which introduce the same delay to the whole signal. In the contrary, the blocking delay lines distort the signal because of a non-zero dead time so they may skip some pulses (e.g. Vernier or counter based delay lines)

[6]Carry chain means the sequence of carry signals of FPGA adders, i.e. the basic digital circuit utilised to sum two bits. Contrary to other elements in the FPGA, the carry path has one of the lowest usable propagation delay.

For that reason, the delay line provides here the delay only up to 36 ns (126 LUTs) adjustable in 64 steps (6 stages) with resolution of about 0.54 ns.

The delay lines realized in this way have the jitter below 20 ps and maximum temperature variance of approximately 100 ps/K. It was also found out that one LUT of the FPGA EP4CE6E22C6N provides an average delay of approximately 270 ps [66]. Related to that, the delay lines have an intrinsic delay of approximately 2 ns which is a cost for the programmability because the signal always has to propagate through all multiplexers (8 LUTs). Additionally, it is necessary to note that these delay lines are not linear and even monotone if the shortest stage contains only a few LUTs. This is caused by the differences in the propagation delay through the individual LUTs (variances in the manufacture process) and the unpredictable length of the routing paths in the FPGA, which cannot be neglected. The second one resides in the process of routing and placing during the VHDL code compilation when the particular logic elements are selected for the circuit synthesis. The algorithms carrying this task out are based on random placing [67] so the LUTs in each stage are not physically in the row but are distributed across the whole gate array. A statistical nature of these delays is captured in Figure 17 where the delay per LUT was measured for several delay lines having different number of LUTs in individual stages. It is possible to see that the average delay per LUT converges to approximately 270 ps if the stage consists of more than 50 LUTs.

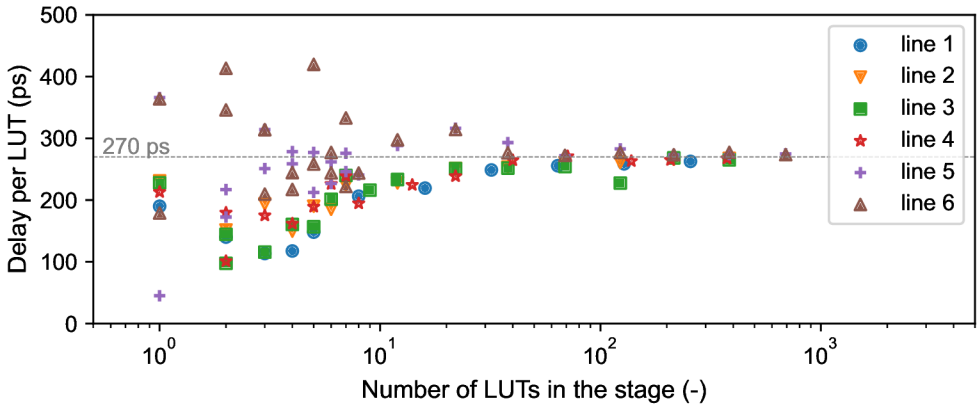

Figure 17: *Average delay per LUT on six delay lines containing a various number of LUTs in individual stages. Data come from the development of the digital delay line [66] where the propagation delay through the individual stages was measured. The lines 5 and 6 contain twice the stages with the number of LUTs lower than nine. For that reason, there are two values of average delay for the same number of LUTs.*

Fortunately, the stability of the delay is much more important than the absolute precision of the delays in the experiments, in which the spectrometer is employed. Nevertheless, in order to characterise the delay lines, in total 14 measurements of the prompt peak positions were performed in the coincidence time resolution experiments [68] with 122 keV photons. In individual measurements, the delay on the stop or start line was gradually increased from the minimum to the maximum. This way, besides the maximum range also a rough estimation of the nonlinearity was found out. The worst nonlinearity of the delay on the start line was 5.0 % (0.64 ns) and 3 % (1.08 ns) on the stop line.

2.1.3 Integrated Time-to-Digital Converter

The target parameters for the TDC were at least 2 μs measuring range, a subnanosecond resolution and a negligible dead time. There are two basic ways how to implement the TDC purely on the FPGA – the utilization of the tapped delay lines or the counters. Tapped delay lines allow to reach a very low resolution in tens or even units of picoseconds [69–71], but not at a large range. Additionally, getting a result complying with the linearity requirements involves the control of the logic elements placing algorithm [71] or has to be handled in another way. Moreover, the tapped delay lines also obey the process, voltage and temperature (PVT) variations which get worsen their stability. On the other hand, the counter-based TDCs utilising one clock offer a practically unlimited measuring range, high stability, negligible integral and differential nonlinearity but their time resolution is limited by the maximum clock frequency (hundreds of megehertzes).

The time resolution can be further improved by utilization of the multi-phase shifted clocks [72–75] which can provide the subnanosecond time bins, but also increases the differential nonlinearity (DNL). Naturally, the TDC designs combine the advantages of both, the tapped delay lines for a fine timing and counters for the course timing [65,76–78]. However these solutions always has to handle out with the imperfections of the tapped delay line.

Since, in our case, a high time resolution in range of tens of picoseconds is not needed, otherwise uncomplicated solution having low DNL is desired, a counter-based design with multi-phase shifted clocks was selected for our TDC. Specifically, the time measurement is based on eight 10-bit counters clocked by either rising or falling edge of one of four 500 MHz clocks which are phase-shifted of 0 ps, 250 ps, 500 ps and 750 ps by internal phase-locked loop (PLL) of the FPGA. A resultant time interval is obtained by summing of all eight counters which gives the maximum measuring range of 2048 ns (8192 time bins, 250 ps time resolution).

The entire TDC consists of two independent time measuring units where each contains the three basic functional blocks which are the time measuring counters (including adders to sum up all counters), a timeout counter and an event controller, see the block diagram of the TDC in Figure 18. These two units alternate in the time interval measuring, in order to minimise the dead time, the first unit is prepared for a new measurement while the second one is measuring. Since the spectrometer has been supposed to be used to measure a nuclear decay times, the detection of the only first event after the starting pulse is necessary. For that reason, the TDC was devised to work in the start-stop regime. Each start pulse always resets the counters in the first time measuring unit and enables the counters in the second one until it is either reset by another start pulse, or stopped by the stop pulse. If the stop pulse occurs, the time measuring counters are summed up in three iterations and the resultant time interval length is saved in the RAM of the FPGA.

The timeout counter fulfils an important role in the time interval measurement termination. If the measurement is started and the stop pulse will not arrive, the counters has to be protected against the overflow. For that reason, the timeout counter always provokes the reset of the time measuring unit after 2 μs. Next, the start pulses, stop pulses and the signal from the timeout counter are continuously assessed by the event controller which executes the data saving and reset of the time unit. If the timeout occurs or another start pulse arrives after the measurement has been started, the event controller only resets the particular time measuring counters and timeout

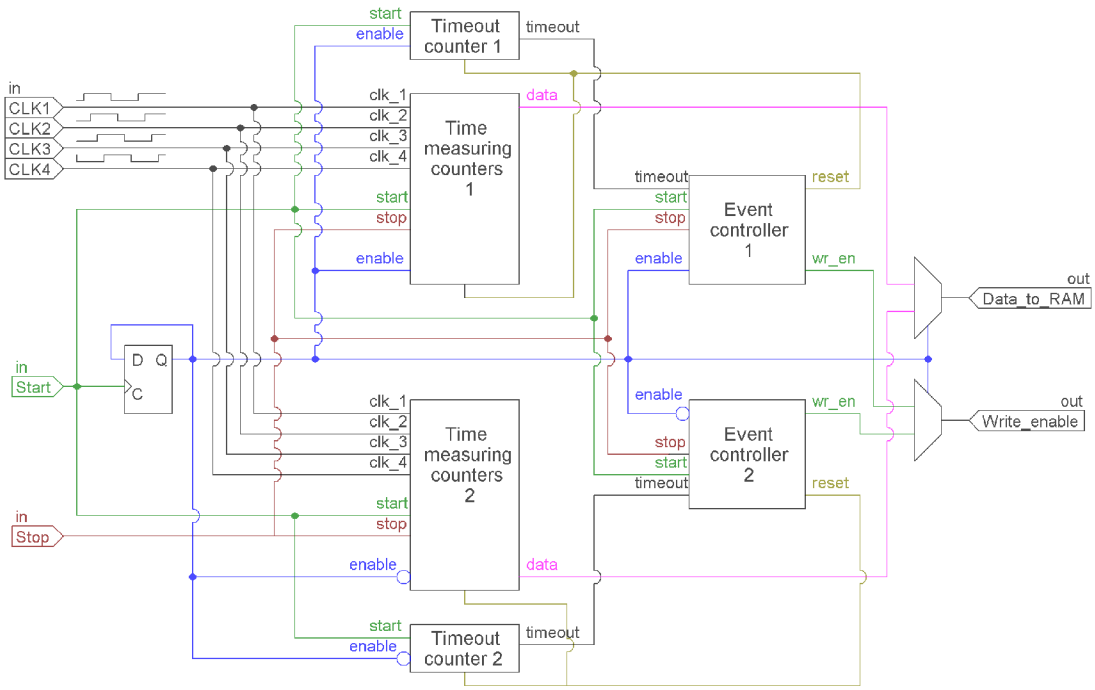

Figure 18: *Simplified block diagram of the TDC consisting of two time measuring units (blocks labelled by "1" and "2"). The inputs of the entity are four 500 MHz differently phase-shifted clocks, a start and stop signal. At the outputs, the TDC passes on the measured time interval and the signal allowing the data to be written in the RAM. For the sake of simplicity, the 250 MHz system clock, which enters the timeout counters, event controller and time measuring counters, was left out.*

counter. In case that the stop pulse comes after the start, the controller, besides the reset, also saves the measured time interval into the RAM.

It should be mentioned that several designs of the TDC were tested. Although some of them were not fundamentally wrong, they did not run correctly or did not work at all when implemented. In general, an implementation of the D-flipflops synchronizers into many parts of the design helped to improve the TDC performance. Although the final design was functional, the conditions of the synthesis were tuned in order to get the best compilation evincing the lowest DNL. The final design comprises of 2904 (46 %) FPGA logic elements covering 980 registers (D-flipflops) and utilizes 1664 memory bits (<1 %).

2.1.4 Time Measurements Characteristics

First, let's explain why the spectrometer offers the measuring range either 1024 ns with 250 ps resolution or 2002 ns with 500 ps resolution although the hardware manages to measure up to 2048 ns with 250 ps resolution. The main reason is the limited capacity of the MCU memory and the structure of the dataset, which the MCU sends periodically to the PC. There is a space only for the half ,i.e. 4096 instead of 8192, time bins. Since we want to keep the measuring range of 2 μs, the time resolution is degraded to 500 ps. This is conducted in the MCU by rotation the measured time intervals by one bit which is equivalent to division by two without reminder. Furthermore, the measuring range is restricted also by the timeout counter at approximately 2 μs so the last tens of bins are always empty.

The DNL of the TDC measured for all time bins within measuring range and under the ambient temperature is lower than ±0.094 LSB (RMS 0.037 LSB) for 250 ps resolution and lower than ±0.058 LSB (RMS 0.015 LSB) for 500 ps resolution. Under the condition that eight and four points are summed up to get 2 ns resolution (counters clock period), the DNL decreases below 0.017 LSB (RMS 0.003 LSB) for both time resolutions, see Figure 19 parts a) and b). The DNL was measured by a density code test [73] when the TDC was periodically started by a rising edge of low amplitude square waveform (400 kHz, high and low level 200 mV and 0 mV respectively, 95 % duty cycle) from an arbitrary function generator and stopped by random pulses from a scintillation detector. A periodic pattern in the DNL, see inset in Figure 19 in part a), springs primarily from the inaccuracy of the clock phase shifts. There are two fundamental factors influencing this clock error a clock skew caused by a propagation of the signals through the global clock networks (maximum estimation ±25 ps) and a precision of the FPGA PLL, (manufacturer declares worst case ±50 ps). The DNL measurements show that the absolute TDC time resolution precision is better than ±24 ps (RMS 9.3 ps). Incidentally, such result is approximately two times better compared to the other FPGA counter phase shifted clocks based TDCs. [72–75].

It should be pointed out that various non-periodical DNL distortions were noticed and they are also visible in Figure 19, in parts a) and b), in the first 300 ns. It was discovered that the DNL is negatively influenced by, for example, the bad impedance of the cables, the shape of the starting signal (its amplitude, spectral width) or by the settings of the BL comparator level. The correct cable impedance and low amplitude signals with slow rising/falling edge improves the DNL. On the contrary, a slow rising edge of the input signal and low overdrive voltage on the BL can increase a propagation delay dispersion of the comparator and thus increase the DNL.

We guess that reflections on the badly terminated cables and fluctuations of electric current flow related to the incoming starting pulse, comparator switching or bad grounding can affect the propagation delay of LUTs (voltage variations) and comparators which cause increase of the DNL in certain times. Position of the distorted region moves based on the settings of the asynchronous delays and it is observed about the time when the starting signal changes simultaneously with the stopping signal. A huge increase of the DNL is shown in Figure 19, part c), where the amplitude of the starting signal was intentionally increased from 200 mV to 2 V compared to the measurement in Figure 19, part b). Additionally, the duty cycle was changed from 90 % to 40 % in order to shift the falling edge into the measuring range. That is the reason why the second distorted region appears around 1100 ns. Since the real cause of the DNL distortion is unknown (a bad grounding and the board layout are the most suspect), the starting signal coming from the function generator has to be properly adjusted to avoid this parasitic effect.

An effective dead time of the TDC is only 60 ns. Although the time measuring unit needs 120 ns until it is prepared for a new measurement, due to a dual design the half dead time is reached. If both time units are busy i.e. two start pulses arrive within 120 ns, then the third start pulse interrupts the saving of the first measured time interval so it is lost. However, such a situation mostly did not happen because the AADs prevent it by their own dead time, which ranges from 20 to 160 ns in dependence on the evaluation delay settings. Typically for the nuclear quantum experiments, where the signal from the scintillation detectors are utilised, the AADs dead time is higher than 60 ns so the TDC dead time can be neglected.

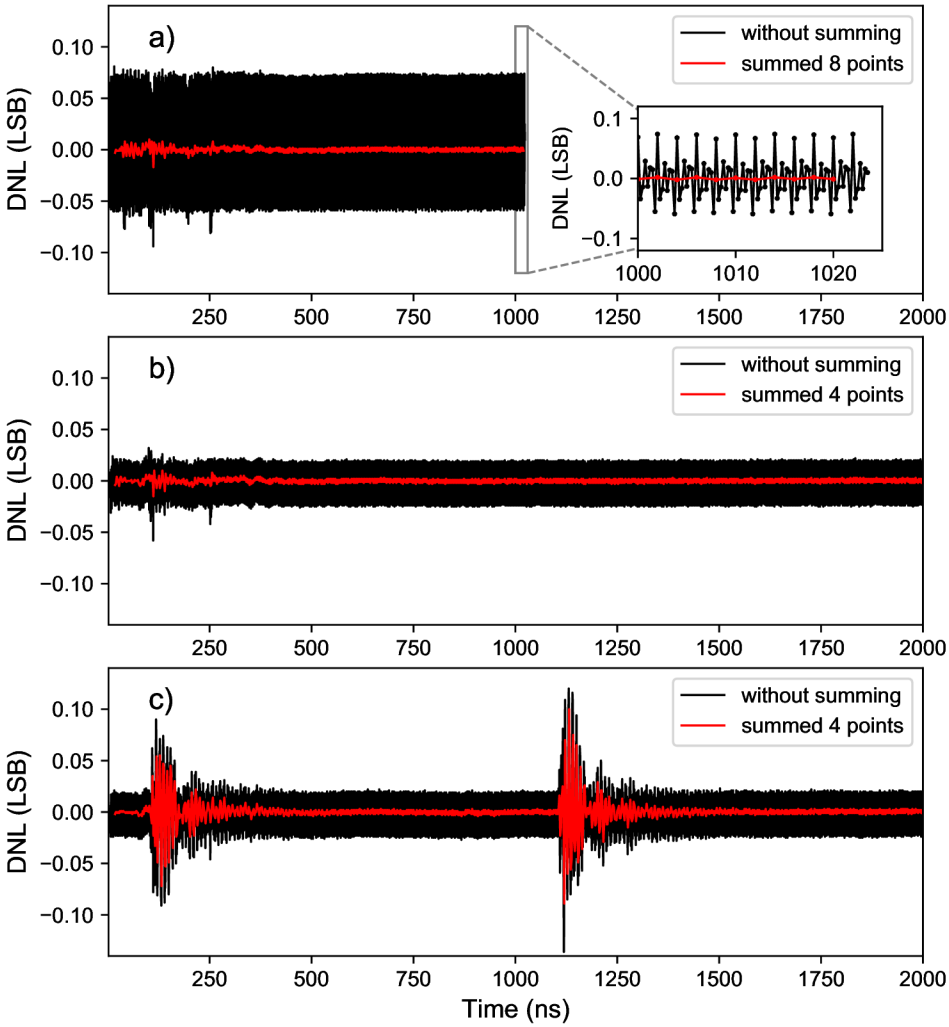

Figure 19: *Differential nonlinearity of the TDC measured with 250 ps resolution, part a), with 500 ps resolution, part b). In both cases the TDC was started by the rising edge of the periodic square signal from arbitrary function generator with frequency of 400 kHz, 200 mV high level 0 mV low level and 95 % duty cycle. A falling edge was set out of the measuring range. The graph in part c) shows the unwanted DNL distortion when the TDC was started by square signal with high level increased to 2 V and 40 % duty cycle, so the falling edge comes 1 µs after the rising edge.*

The maximum countrate of the time intervals that the spectrometer can measure is much lower than the TDC can handle. This is due to the limited acquisition time in which the MCU has to process the data from the FPGA for each channel of the spectrum. Since this time depends on the frequency of the transducer motion, the maximum countrate relies also on it. To ensure the safe operation of all processes in the MCU, especially the communication with the PC, a data processing interrupt handler has to be serviced in maximum of 7 µs. However, for the frequency above 50 Hz, the acquisition time drops to ≈ 10 µs per channel and critical time of only 3 µs remains for all other tasks. Therefore, as the frequency increases from 50 Hz up to 80 Hz (the maximum spectrometer frequency), the time for the data processing is further constrained to 4 µs. Because the most time consuming operation is the sorting of the time intervals into histograms and TDMS spectra (≈ 400 ns per event), the

maximum number of time intervals, which the microcontroller can read out of the RAM of the FPGA in a line, is restricted to 15 for the frequency below 50 Hz and decreases to 5 as the frequency increases. Thus the maximum processable countrate of the time intervals linearly increases from 0.09 MHz up to 1.4 MHz for the frequency from 3 Hz up to 50 Hz and decreases linearly down to 0.82 MHz at frequency of 80 Hz. All time intervals, which the TDC measures above the mentioned limits, are lost.

The total data latency of the time interval measurement, i.e. the time from the stop pulse arrival at the spectrometer inputs until the data are prepared to be read by the microcontroller, depends mainly on the TDC latency ($\approx$ 150 ns) settings of the AADs (2–140 ns) and the delay on the stop line (2–140 ns). If the propagation delays through the comparators (2–3 ns) and input buffer of the FPGA (6–7 ns) are included, then the latency ranges from the minimum of approximately 164 ns up to the maximum of 440 ns. The reason for mentioning the latency parameter is that it determines the precision with which the pulses are sorted according to the Doppler energy modulation. If the incoming pulse is detected a short time before the FPGA is read out, the TDC do not have to manage to save this event into the RAM on time so that it is added into the correct channel. Instead, the event is assigned incorrectly to the neighbouring channel. Assuming the maximum latency of 440 ns and 16.2 μs acquisition time per channel (at energy modulation frequency of 30 Hz) gives the energy sorting error (energy shift) of 0.027 channel. Such an error may be neglected in the Mössbauer spectra measurements.

The performance of the spectrometer in the time measurements is shown in Figure 20 where the decay time of the first excited state of the ^{57}Fe is obtained at the high resolution of 250 ps. In this experiment, the one inch thick $LaBr_3$:Ce scintillation detector (Saint-Gobain Crystals scintillator with photomultiplier (PMT) R9420 and ORTEC 296 ScintiPack PMT base) was utilised for detection of starting 122 keV photons and the 400 μm thick (1-inch diameter) YAP scintillation detector (Crytur scintillator, PMT R6095 with socket C9028-01) was used for detection of stopping 14 keV photons. The delay lines were set to the minimum and the maximum on the

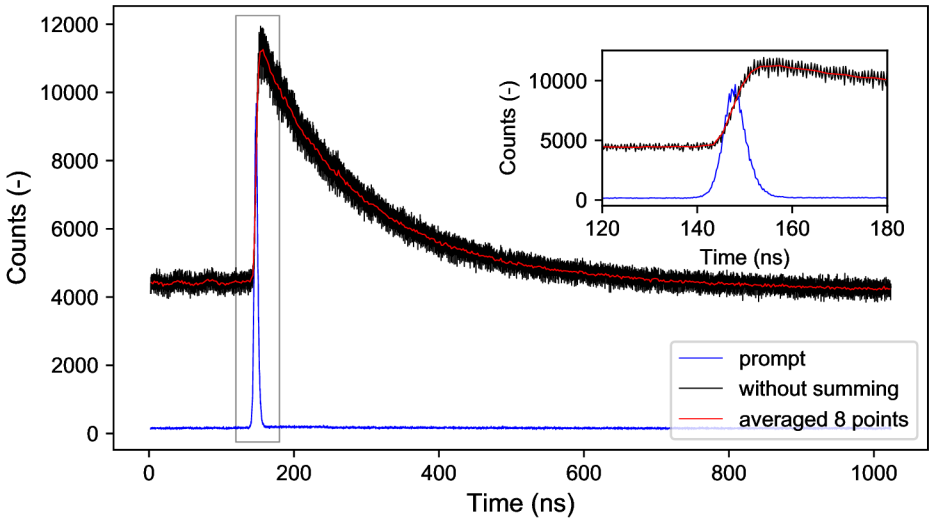

Figure 20: *Lifetime of the first excited state of ^{57}Fe and a prompt peak of the coincidence setup measured with 250 ps time resolution. Fitting the prompt peak with normal distribution gives the time resolution of the coincidence setup and total coincidence delay 5.4 ns (FWHM) and 147.9 ns respectively.*

start and the stop line respectively, therefore the rising edge of the life time decay is shifted by approximately 148 ns. A prompt peak of scattered 122 keV photons was also measured to demonstrate the time resolution of the coincidence setup which was 5.4 ns (FWHM). A better result can be achieved with faster PMTs or constant fraction discriminators.

2.2 Piezotransducer

Gamma radiation intensity control requires a high-frequency motion of the resonant absorber at amplitude levels comparable to the gamma photon wavelength. Piezoelements are the best way to achieve the well-controlled low amplitude motion, even on the scale of picometres. Specifically, the beta phase of the organic polymer polyvinylidene fluoride (β-PVDF) exhibits suitable piezoelectric properties such as a sufficient electromechanical coupling and high frequency response [79] for this purpose. Unlike other piezoelectric materials, such as quartz or piezoceramics, the PVDF can be easily formed into thin foils (tens of μs) which exhibit negligible gamma radiation absorption. This makes the PVDF a suitable piezomaterial for the realization of the low-amplitude motion in gamma optical experiments. As the high-frequency positioning of the Mössbauer absorber at a picometre scale is a specific task, no suitable transducer or actuator was found on the market. For this reason, the purpose-built piezotransducer was developed.

We got inspired by the experimental equipment in the previous works [19, 25, 27] where the 28 μm thick piezofoil by Measurement Specialties, Inc., model LDT0-28K was utilised. When constructing our piezotransducers, we have tested two piezofoils from the same manufacturer – the aforementioned 28 μm PVDF foil model LDT0-28K and 52 μm PVDF foil model DT1-052K. The creation of the good piezotransducer requires sufficient backing for the foil and gluing the resonant absorber tightly onto the foil. Practically, it means that the piezofoil is forever connected to the particular absorber because removing it results in the piezofoil damage. The backing for the foil is required in order to suppress the resonant frequencies [80] and improve the momentum transition to the absorber. Tight sticking is desired for the same reason as the backing pad because any kind of the matter (plastic coating, glue) can be understood as a spring [81] which influences the momentum transfer from the surface of the piezomaterial to the absorber.

Different types of backing (3D printer plastics, mica pad, plexiglass) with a hole in the middle or full and two basic types of glues, an epoxy glue and an acrylic glue (so-called "second glue"), were tested. To evaluate the quality of the transducer, the two main qualities were studied: the homogeneity (coherence) of the motion and the amplitude of the motion at given driving voltage and frequency. Both can be recognized either from the measurements of the energy spectra [27] or time intensity waveforms of gamma radiation [20] which are caused by the interference effects of the scattered gamma radiation on the vibrating absorber. If the motion of the absorber was inhomogeneous (incoherent), i.e. not all nuclei vibrate the same, the comb structure in the energy spectrum or radiation intensity in time domain simply did not agree with the simulations assuming the uniform (homogeneous) motion of the whole surface of the absorber.

The best results were observed for the 28 μm foil (LDT0-28K) fixed to the approximately 2 mm thick compact plexiglass, see the cross section an the photo of created piezotransducer in Figure 21. Both the backing and the absorber were tested

to be glued by either the epoxy or acrylic adhesives but any significant difference in electromechanical properties was not observed between these two approaches. Nevertheless, the type of adhesive may play an important role since the driving of the piezotransducer at high frequencies leads to a considerable heat dissipation. An experience of one research group [9, 31] is that they observed a deterioration of the electromechanical properties of the piezotransducer glued by the epoxy glue as its temperature increased above 50 °C. From this point of view, the acrylic glue seems to be a better choice due to its temperature stability.

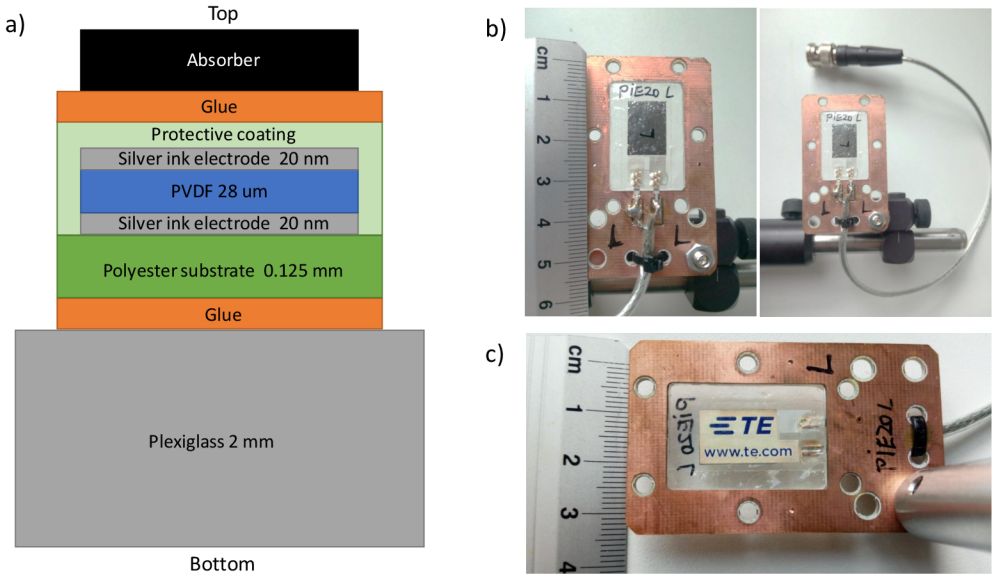

Figure 21: *A cross section, part a), and the photos of the created PVDF piezotransducer from the top, part b), and the bottom side, part c). Plexiglass is surrounded by a holder milled from the cuprextit which serves for the cable mounting.*

In the following paragraphs, some experiences, dead ends and ideas are presented. The backings with a hole in the middle eliminate the absorption of the gamma rays coming through, but the amplitude of the absorber vibrations was roughly 2 times lower than if the backing was a tough compact plane. Absorption loses can be further reduced by the utilization of thinner backing. For example, a 1 mm thick plexiglas of an old CD cover can be easily obtained.

For the 52 μm PVDF foils it is possible to expect that the thicker piezofoil will allow a larger displacements compared to the 28 μm foils. It was assumed that the higher volume of the piezoelectric material will expand more but the piezofoil deformation depends on the electric intensity not only an absolute voltage on the electrodes. Since the thickness is approximately twice the size, for the constant voltage on the electrodes the electric intensity is twice lower and the total expansion of the piezofoil remains the same. Nevertheless, the behaviour of the both piezos must not be identical if the dependence of the applied electric intensity on the piezofoil deformation is nonlinear.

In case of 52 μm PVDF piezotransducer the both inhomogeneous and homogeneous behaviour of the absorber motion was observed for particular frequencies. For example, the radiation intensity time structure was in agreement with the theoretical predictions for 1, 2, 3, 8, 9, 10 and 11 MHz but were distorted for 4, 5, 6 and 7 MHz. We do not have an explanation for such a strange behaviour. But the mistake could be

that we cut the piezofoil in order to decrease its capacity. Furthermore, it was more difficult to glue these 52 μm piezofoils well because, in contrast to the 28 μm foils, the model DT1-052K is much softer because it lacks the 125 μm reinforcing polyester layer. For this reason, the piezofoil could be distorted and vibrate non-uniformly.

2.3 Piezotransducer Driver

Driving of the piezotransducers at high frequencies (1–50 MHz) contends with three basic issues which are related to the capacitive nature of the piezoelement and the energy transfer troubles due to inadequate impedance matching. Firstly, not all function generators or amplifiers are designed to drive the capacitive loads. In some cases a phase margin, caused by the capacity, may lead to undesired oscillations. This problem is typically fixed by inserting the resistor in series with the capacitive load. Secondly, achieving large displacements requires supplying the electrodes of the piezoelement with the highest possible voltage. However, the impedance of a piezoelement at high frequencies is quite low, e.g. assuming pure 1 nF capacity at 10 MHz gives the impedance of about 16 Ω. If the function generator with 50 Ω output impedance was utilised in this case only 24 % of voltage amplitude would be applied on the capacitive load. For this reason, the lowest possible output impedance of the driver is desired in order to maximize the voltage on the piezotransducer.

Unfortunately, decreasing the output impedance is in contradiction with the third issue concerning impedance matching. If the piezotransducer is powered via a long interconnection[7], the proper impedance termination has to be ensured otherwise reflections occur and the ratio of transferred energy decreases. For that reason, a transmission line, driver and load as well should be impedance-matched. Nevertheless the impedance of the piezotransducer varies with the frequency and it is typically impossible to adjust it precisely to the typical transmission line impedances (50 Ω, 75 Ω, 100 Ω). In such cases, the impedance-matching transformers or networks consisting of inductors and capacitors are necessary, otherwise only a fraction of the energy is delivered to the piezotransducer [82–84].

The aforementioned facts give the choice of using either a long cable with impedance matching or a short cable with a low output impedance driver. Since the considerable alternate currents (up to 200 mA, 15 V_{pp} at 12 MHz) flowing into our piezotransducer through longer cables would increase the radiation of unwanted electromagnetic waves, it was decided to use short cables and to develop a purpose-built driver with low output impedance. Besides that, a small size of the driver was required so that it could be placed close to the piezotransducer in confined experiment conditions.

The developed piezodriver, which schematic is shown in Figure 22, is based on the two current-feedback operational amplifiers THS3491 [85] in a parallel connection. This type of operational amplifier was chosen for its ability to drive the capacitive loads with high power at the required frequencies. The piezodriver provides the output voltage ±14V with a linear output current up to 200 mA into the capacitive loads of about 1 nF. The input signal is terminated by 50 Ω and the gain is set to 5 by feedback resistors. The total output impedance is about 9 Ω which is given mainly by the external resistors. The output impedance solely of the THS3491 lies below

[7] To distinguish the short interconnections from the long transmissions lines, one-tenth of sinusoidal wavelength passing through the interconnect is taken as a conservative rule of thumb. For example, the division length for 20 MHz in a coax cable is roughly 1 m. Shorter interconnections can be considered as lumped capacitors, but the longer ones are the transmission lines.

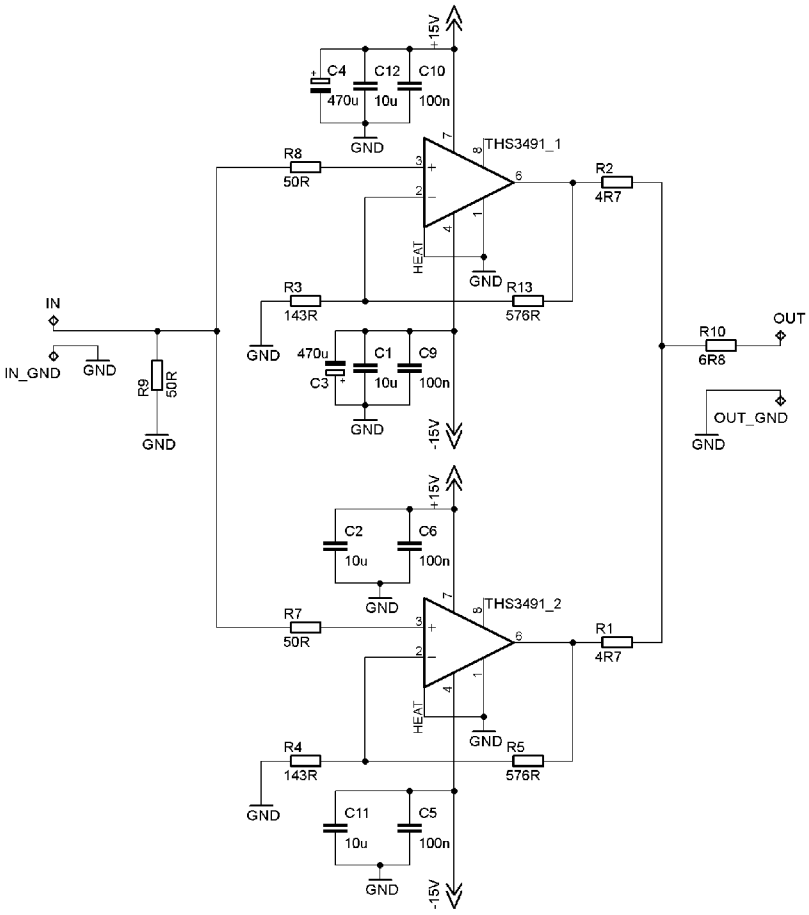

Figure 22: *Schematic of the piezodriver based on the operational amplifier THS3491.*

0.2 Ω for frequencies lower than 20 MHz. Attempts were made to decrease the resistor values further but the driver tended to oscillate.

Next, the special care was devoted to the chip cooling because the power dissipation warms it up and disturbs the stability of the operational amplifier. Since the driver was placed in the aluminium box with the dimensions 110 × 63 × 40 mm (L × W × H), see photos in Figure 23, there was not too much space for a heat sink. For that reason, the heat is led away by the 3 mm thick copper strip which is tightly

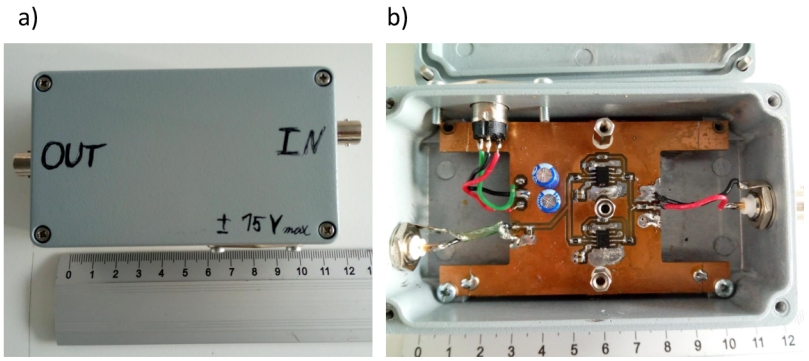

Figure 23: *Developed piezodriver: outside view, part a), and inside view, part b).*

screwed to the board (from the bottom side) and thermally connected to the box, which serves as a huge heat sink.

Compared to the arbitrary function generator Siglent SDG2042, which has been utilised for piezotransducer driving in the first experiments, the developed piezodriver has approximately five times lower output impedance, it provides 40 % higher output voltage range and it is thirty times less spacious. Thus the driver enables to apply about 2.7 times higher voltage at 12 MHz on our piezotransducer, which evinces capacity of roughly 400 pF. Moreover, the piezodriver also provides sufficient power which allows to exploit the piezotransducer to its physical limit. Specifically, the driver remains stable even if the output power heats the piezotransducer above the temperature of 50 °C when the mechanical properties of the transducer's layers change in an undesirable way.

3 Gamma Radiation Intensity Control

This chapter contains the complete description of the experimental work concerning the coherent control of the gamma radiation intensity by the vibrating Mössbauer absorber, which was presented in Chapter 1. First, the experimental setup and the type of measurements are described in detail. Subsequently, a methodology for determining the frequency response of the piezotransducer system is explained. Specifically, the dependence of the amplitude and the phase of the Mössbauer absorber vibrations on the driving voltage are the subject of interest because it is crucial for realization of more complex absorber motion profiles composed of more than one harmonics. Related to that, one section is devoted to the fitting of the measured time histograms. Since the numerical calculations rely on few parameters, which are undesirably correlated, it was necessary to fix some of them in order to get a correct results.

After the piezotransducer is characterized, the predicted generation of the well-separated high-intensity single pulses, double pulses and short-term acoustically induced absorption are presented. For that the trapezoidal, square, triangular and bipolar pulse motion profiles, which composed of up to 12 harmonics (1–12 MHz), were applied. Furthermore, the limits and specific problems of the multi-tone piezotransducer vibrations are described. At the end of the chapter, ideas of further experimental development and potential application of the presented technique for gamma radiation intensity control are listed.

3.1 Experimental setup

Experimental investigation of the gamma radiation intensity control by the multi-tone vibrating absorber requires measuring the time-of-flight histograms of the 14 keV gamma photons which energy is tuned to the certain level. The time-of-flight is measured between the starting pulse synchronized with the high-frequency motion of the Mössbauer absorber and the detection of the 14 keV photon. The diagram of experimental setup, which utilizes components described in Chapter 2, i.e. the spectrometer, piezodriver and piezotransducer, is shown in Figure 24.

The radioactive source (^{57}Co, 1.85 GBq) was screwed on the transducer which ensured Doppler energy modulation. Gamma radiation from the source interacted with the vibrating Mössbauer absorber and out-coming photon field was detected by scintillation detector. Specifically, 1-inch 400 μm thick YAP:Ce scintillation crystal (by Crytur) with the PMT R6095 and socket C9028-01 (by Hammamatsu) were utilised. The signal from the detector was amplified by the transimpedance amplifier of our construction [53] and connected to our Mössbauer spectrometer.

The high-frequency motion of the Mössbauer absorber was provided by the piezotransducer which was driven by the piezodriver. The Mössbauer absorber was the 25 μm thick stainless steel foil from Alfa Aesar, production No. 41580, type 304, with a natural abundance of ^{57}Fe. The shape of the driving waveform was generated by one of the two channels of the arbitrary function generator SDG2042X (by Siglent). As the output channels are synchronised, the second output was utilised to generate the start pulse for the time measurements. This way the synchronization of Mössbauer absorber motion and the start pulse was ensured. The arbitrary waveforms required to drive the piezotransdcuer, were loaded into the generator by means of the free software tool EasyWave (by Siglent), which allows the waveform to be entered in form of equation, e.g. Fourier series.

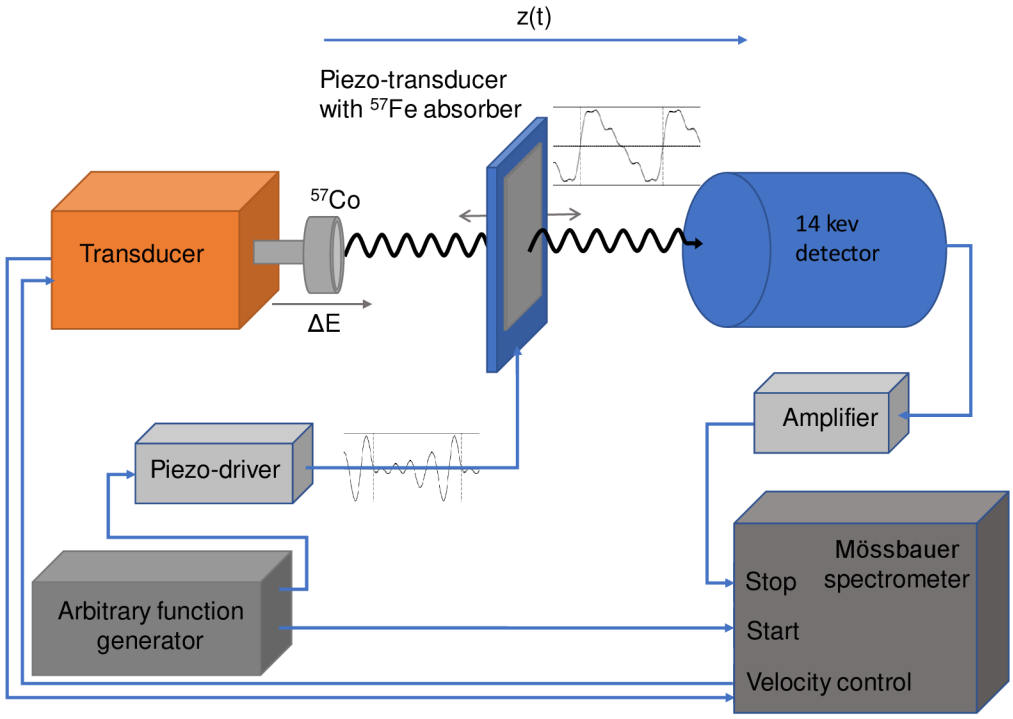

Figure 24: *Experimental setup for measurement of the gamma radiation intensity controlled by a vibrating absorber.*

The spectrometer was operated in two regimes. Once a time it was required to measure the Mössbauer spectrum of the absorber to get the information about the measurement effect. But most of the time, the spectrometer was set to measure the time histograms. In these measurements, the transducer was driven in the constant velocity regime so that it tuned the energy of the gamma photons to the positive $(+\Delta E)$ and negative $(-\Delta E)$ values for equally long time. This regime was utilised to acquire two time histograms simultaneously for different energy detuning within one measurement. Specifically, the time intervals were added to the particular histogram only within the channels 200–800 and 1200–1800, see Figure 25.

3.2 Piezotransducer Frequency Response Measurement

It is already known that the Mössbauer absorber glued to the PVDF piezofoil moves harmonically when driven by a harmonic voltage [25–28]. However, if more complicated motion profiles are required, they are difficult to be achieved if the system is not linear, i.e. the principle of superposition does not hold true. In general, the piezoelectric materials are non-linear. Their electromechanical frequency response depends on the shape of the piezoelement, its microstructure, mounting, intensity of applied electric field, its temperature etc. [86–88]. The excitation by sinusoidal voltage does not have to result in sinusoidal motion of the piezoelement surface. However, for some materials and under certain conditions, e.g. low excitation voltage, the non-linearities are so small that the system can be approximated as linear. Since the

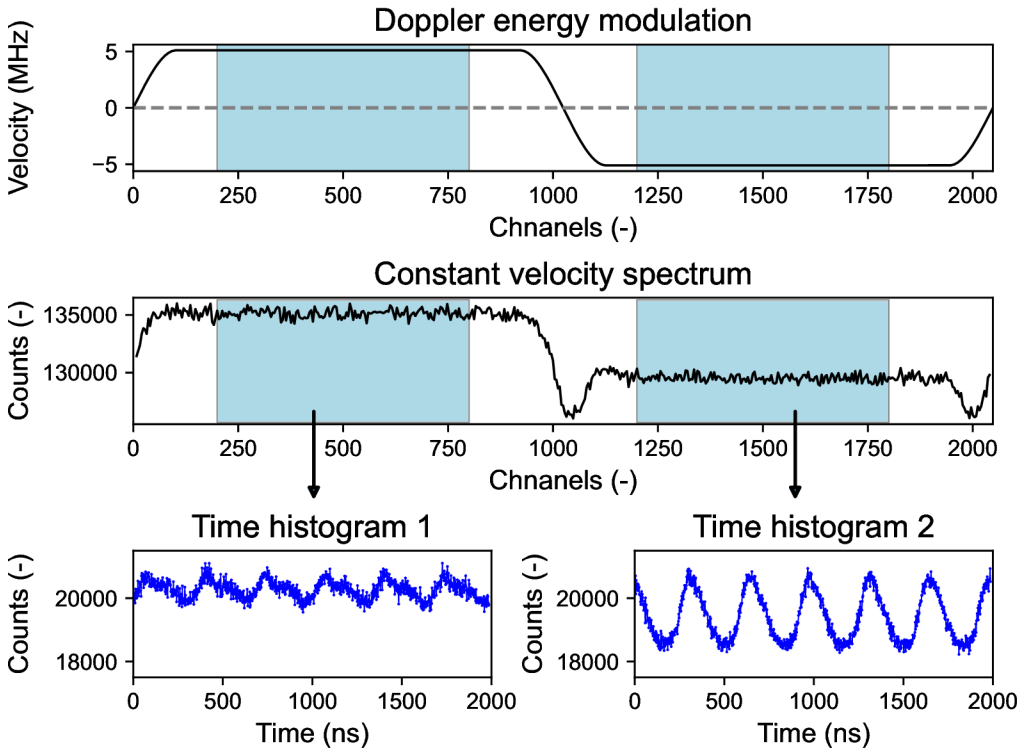

Figure 25: *Acquisition of two time histograms in the constant velocity regime. Only the time intervals measured within the channels in the coloured regions, where the energy modulation is constant, are added to the particular time histogram. The principle is demonstrated on the measurement of the 3 MHz photon field time structure for energies tuned to ±5.1 MHz.*

complex analysis of the properties of our piezotransducer would be demanding, it was simply assumed that it could be a linear system. Under this assumption, the relation between the driving voltage and the real motion of the absorber can be described by a complex frequency response function where the real part defines the relation of the amplitudes and the imaginary part determines the differences of the phase shifts.

One way, how to get the required response function, is to know the frequency response of individual parts, i.e. piezodriver, piezotransducer including the cable, electromechanical coupling of the piezofoil and mechanical coupling between the piezofoil and the absorber. However, obtaining all of them would be too complicated. Since they are assumed to be linear systems, the response function of the entire system can be measured directly between the on generator set driving voltage [8] (hereinafter only driving voltage) and the motion of the absorber.

The driving voltage is under our control so it remains to measure the real motion of the Mössbauer absorber which vibrates, however, on the level of units, maximally tens of picometres. Fortunately, the most natural way to measure such a low amplitude is to use the interference effects which are caused by the motion itself. Such a method for determining the amplitude of the high-frequency harmonic motion has already been published [27, 28] and an outstanding spacial resolution in units of picometres was achieved. It was based on the measuring of the comb structure in the Mössbauer spectrum. However, this method was unsuitable in our case, because it does not

[8] Relation between the on generator set driving voltage U_d and the voltage on the piezotransducer $U_{piez.}$ is approximately given by relation $U_{piez.} \approx 2.5 U_d$

provide the information about the phase shift. For this reason, it is necessary to measure the time structure of the photon field, because it allows to obtain not only the information about the amplitude response, but also the phase of the absorber motion relative to the phase of the driving voltage. In addition, the time domain measurement is much more sensitive. Especially low amplitudes vibrations, which are hardly distinguishable in the energy domain, are well visible in the time domain in the form of oscillations. As an example see Figure 26 where the manifestation of the interference effects in both domains is compared.

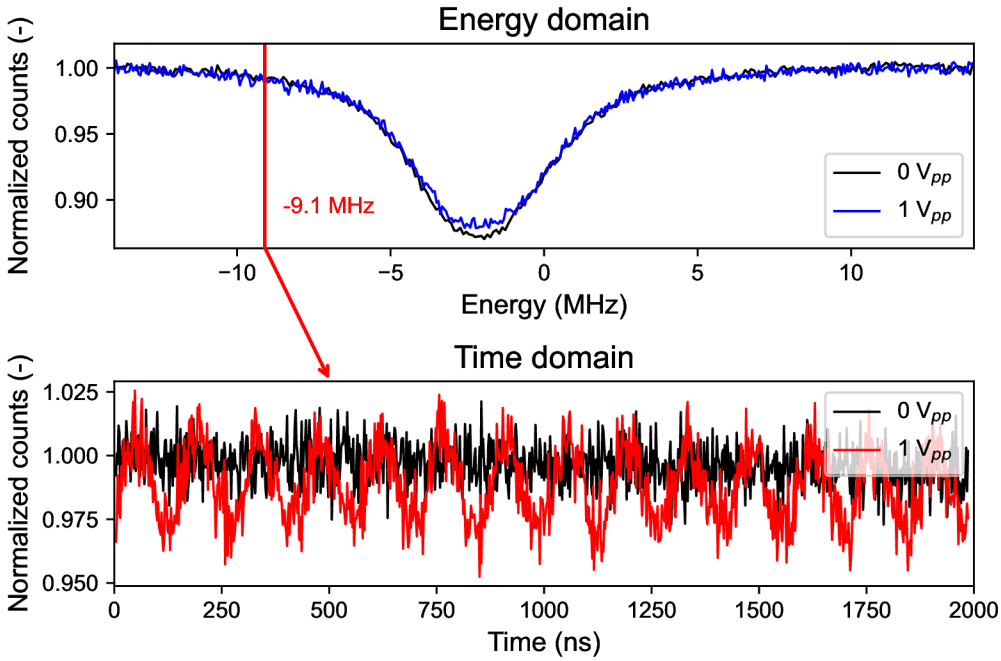

Figure 26: *Comparison of the interference effects caused by static absorber (driving voltage $U_d = 0\ V_{pp}$) and absorber vibrating at 7 MHz ($U_d = 1\ V_{pp}$) in the energy and the time domain. Contrary to the energy domain where a tiny difference in the amplitude of peak (0.007 in normalised intensity) is detected, in the time domain, the distinct oscillations (0.03 peak-to-peak in normalised intensity) are observed. Black lines show the intensities without the motion of the absorber. The driving voltage of 1 V_{pp} induced the harmonic motion with an amplitude of approximately 2.6 pm (0.026 Å). The time waveform for 0 V_{pp}, unlike the others, is not a real measurement but only the corresponding simulation of the invariable intensity.*

In general, the entire frequency response function can be acquired within one single measurement if the spectral-broad input signal, e.g. the step function, excites the system. Response coefficients for individual frequencies are then obtained by the comparison of the input and output Fourier spectrum. However, in our case, when the linearity of the system was only supposed, the results of such a complex measurement would be unreliable and data fitting would be much more complicated because of higher amount of parameters. For that reason, the response function was measured point by point for single frequencies. Since the preliminary measurements in the time domain showed that the dependence of the vibration amplitude and phase on the driving voltage is not linear, see Figure 27, the response function was acquired also for different values of the driving voltage. The only disadvantage of this approach is that the numerous time consuming measurements have to be conducted.

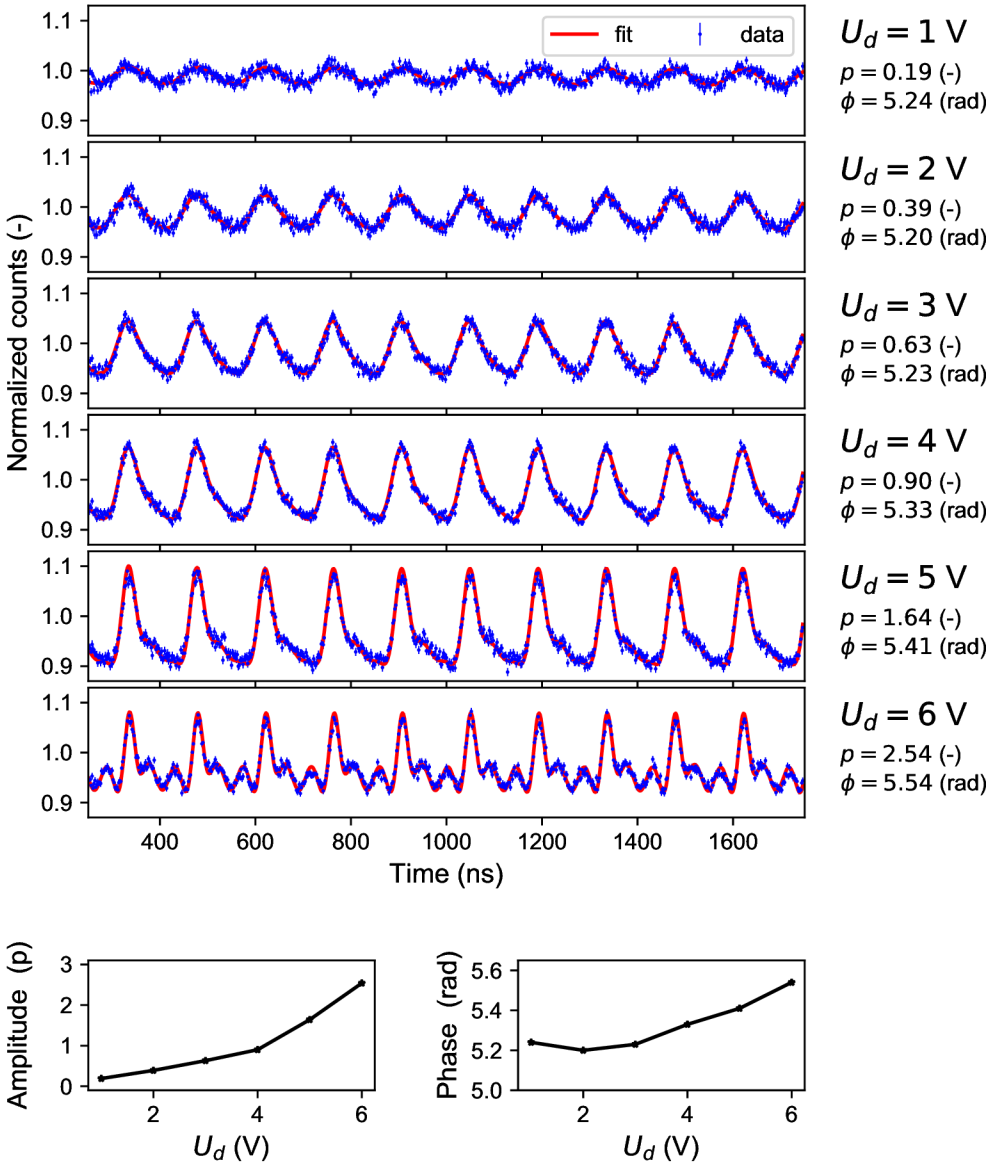

Figure 27: *Time histograms and nonlinear dependence of the absorber vibrations amplitude p and phase ϕ on the driving voltage U_d. The photon field time structure is acquired for 7 MHz frequency and energy tuned to -9.1 MHz (approximately the position of the first sideband).*

All time domain measurements were conducted so the gamma photons energies were tuned to the values $\pm(-2.1 - f)$ MHz, where f is the driving frequency in megahertzes and the value of -2.1 MHz is a constant related to the resonant line shift of the absorber[9]. Thus the energy was always detuned from the resonance approximately to the first sideband ($\Delta E = -f + 0.4$ MHz) and to the opposite energy ($\Delta E = f + 4.6$ MHz). The two time histograms, which were obtained within each sin-

[9] A correct value of the absorber line shift is 2.5 MHz. The difference of 0.4 MHz comes from preliminary experiments when this energy shift was determined imprecisely. In order to keep the comparability of all performed measurements, the tuned energy was not corrected.

gle measurement, were fitted and extracted amplitude and phase shift were averaged in order to get a more precise result. This way, the response function was measured for twelve frequencies from 1 up to 12 MHz in total of 47 measurements.

Resultant frequency response of the entire system, i.e. between the driving voltage and absorber motion, is shown in Figure 28, parts a) and b). One can see miscellaneous trends in the amplitude and phase response, whose explanation is far beyond the scope of the present thesis. Dependence of the response function merely on the frequency for constant driving voltage 1 V_{pp} is shown in Figure 28 in parts c) and d). The maximum amplitude response was observed for 1 MHz and local maxima for 6 MHz and 10 MHz. On the other hand, the lowest amplitude response was for 4 MHz and local minima for 7 MHz. A huge step in the phase characteristics for 9 MHz is caused by displaying the values in interval $\langle 0, 2\pi \rangle$.

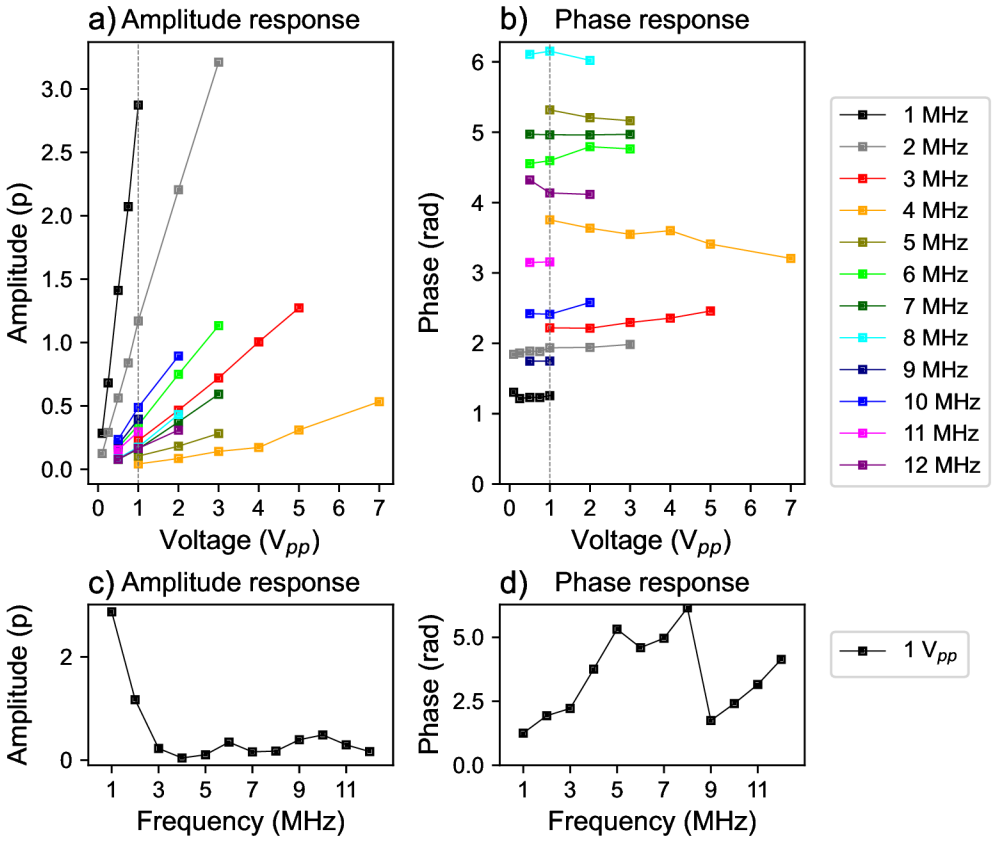

Figure 28: *Frequency response function between driving voltage and absorber motion. Amplitude and the phase response in the dependence on the driving voltage for individual frequencies are shown in the parts a) and b) respectively. The amplitude and phase response for constant driving voltage 1 V_{pp} are shown in the parts c) and d) respectively.*

3.2.1 Frequency Response Stability

This subsection brings a note about the change of the frequency response function which was observed during the experiments. The first characterization of the piezotransducer system spent approximately two months (almost 90 measurements). After that, the first multi-tone motion profiles were tested, but the results were not

in as good agreement with the predictions as desired. For that reason, the response function for particular frequencies was remeasured and it was found out that different results were obtained. Specifically, the amplitude response at 11 MHz increased of 20 % and phase shift decreased of 10 %. Based on this finding, the response function was measured again for all frequencies but not for all driving voltages. For the low frequencies, the amplitude response was high enough with lower driving voltages so the higher ones were not necessary. For higher frequencies, the higher driving voltages were skipped for two reasons. First, the intended motion profiles required only low amplitudes at higher frequencies. Second, there were concerns that the changes in the response function could be caused by piezotransducer heating, which takes place at higher frequencies and amplitudes. In total, two response functions were acquired. One is labelled as old, and the other one, which is presented as resultant in Figure 28 in previous section, is labelled as new. Comparison of both response functions is shown in Figure 29. Another comparison of the response functions for constant driving voltage of 1 V_{pp} is depicted in Figure 30.

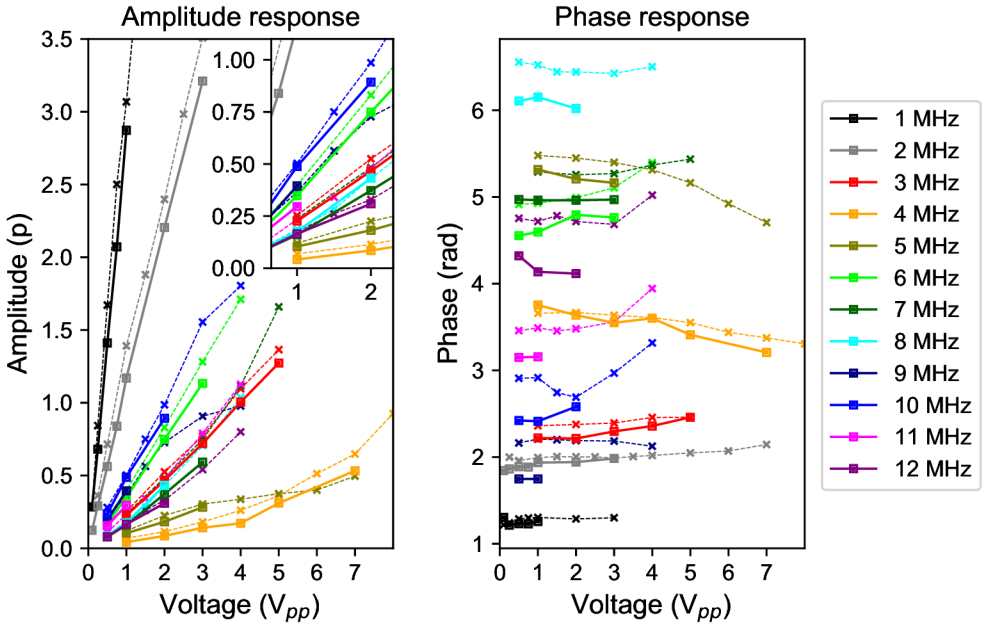

Figure 29: *The old (dashed line with crosses) and new (solid line with squares) response function in dependence on the driving voltage for individual frequencies.*

The cause of the response function change remains unexplained. We think that it could be a consequence of the heating of the piezotransducer near to 50 °C, which could lead to degradation of the piezoelectric material or the change in the mechanical properties of the epoxy adhesive. However, it was much more surprising that the radiation intensity waveforms acquired for the driving voltage calculated using the old and the new response function did not differ significantly, although the individual parameters changed by tens of percent. An example comparison of two time waveforms is shown in Figure 31. It means that the absorber motion control may be relatively resistant to the cumulation of such errors in the response function.

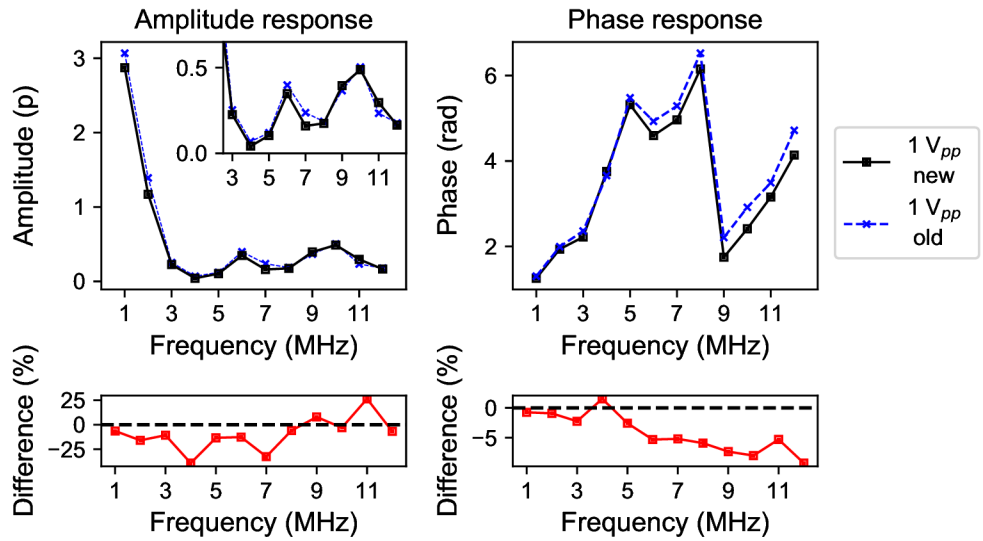

Figure 30: *The old (dashed line with crosses) and new (solid line with squares) response function at the constant driving voltage 1 V_{pp}.*

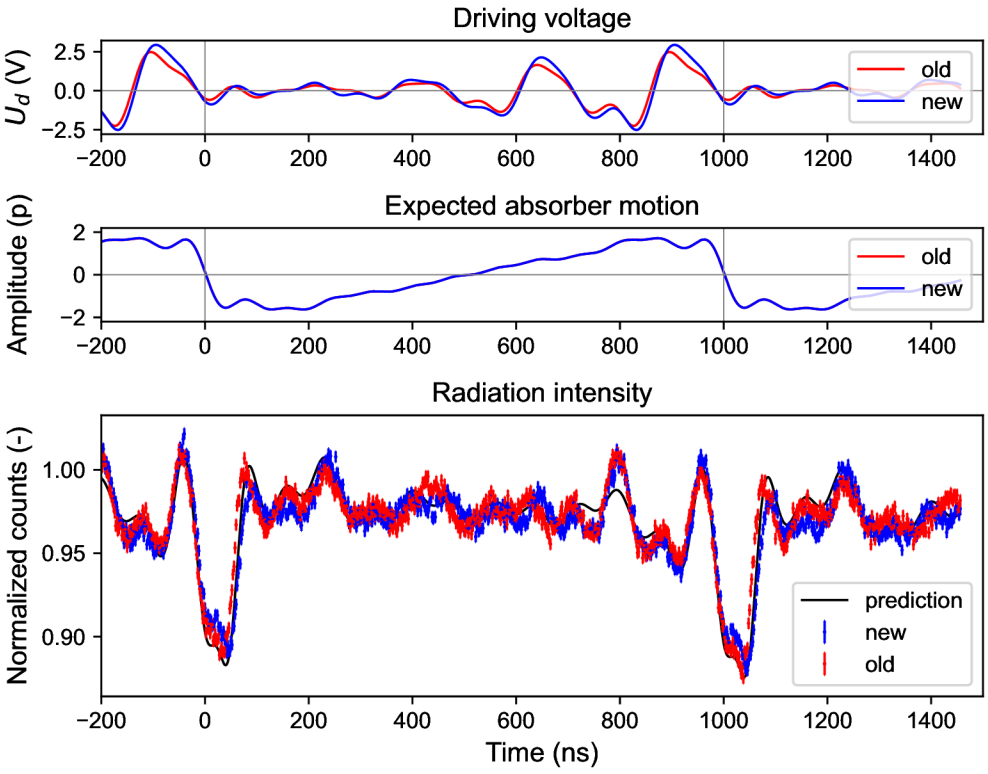

Figure 31: *Radiation intensity waveforms controlled by voltage waveforms computed from the old and the new response functions. Energy was tuned to −9.1 MHz. Despite the maximum value of the driving voltage changed of 15 %, both intensity waveforms are very similar.*

3.3 Data Fitting

The proper method of fitting the time histograms is crucial for obtaining the correct values of the harmonic motion parameters ,i.e. for measuring the frequency response, and also for comparing the simulations with the experiments. This task is not so simple because, in our case, the function describing the intensity of radiation

in time depends on twelve parameters. In addition, some of the parameters are undesirably correlated which affects the precision of the results. For this reason, it is necessary to measure and fix as many parameters as possible, and the instructions on how to carry this out are provided in the present section.

Let's list all the parameters, which are involved in the fitting of the radiation intensity scattered in the harmonically vibrating absorber, i.e. $K = 1$, $B_1 = 1$ (recall the list of parameters in Table 1 in Subsection 1.3.2). In such case, the normalised radiation intensity $I(t)$, depends on frequency f, amplitude p and phase ϕ of the Mössbauer absorber motion, the energy detuning ΔE, linewidth of the source Γ_s and the Mössbauer absorber parameters such as absorber linewidth Γ_a, effective thickness d_{eff} and hyperfine magnetic field B_{hf}. Furthermore, the fitting of the experimental data requires other parameters such as the number of counts N, time resolution of the apparatus σ_t, normalised amplitude of the non-resonant background A_{bcg} and the exponential countrate decay constant C_{bcg}. The latter parameter is introduced to describe a gentle inclination in the number of counts, which is observed for the longer time intervals in the time histograms. This is due to the way the time interval is measured. Only the first 14 keV photon is registered after the start pulse, not all of them. Since the photons arrive randomly relative to the start pulse, the probability that the longer time interval is measured decreases exponentially in dependence on the countrate of the 14 keV photons.

The function utilised for fitting the experimental data $I_{exp}(t)$ is given by a convolution of the radiation intensity scaled to the experimental data $I_s(t)$ and the Gaussian time resolution $G(t)$ of the apparatus,

$$I_{exp}(t) = I_s(t) * G(t)\,, \tag{20}$$

where

$$G(t) = \frac{1}{\sqrt{2\pi}\sigma_t} e^{-\left(\frac{t}{\sqrt{2}\sigma_t}\right)^2} \tag{21}$$

covers the parameter σ_t which is related to the FWHM of the time resolution as FWHM $\approx 2.35\sigma_t$. The other experimental parameters N, A_{bcg} and C_{bcg} are included in the scaled radiation intensity $I_s(t)$, which has a form

$$I_s(t) = \left(\frac{I(t) + A_{\text{bcg}}}{1 + A_{\text{bcg}}}\right) N e^{-\frac{t}{C_{\text{bcg}}}}\,. \tag{22}$$

The rest of the parameters, i.e. Γ_s, Γ_a, p, ϕ, f, ΔE, d_{eff} and B_{hf}, are covered in the normalised radiation intensity $I(t)$.

From the parameters listed above, the p and ϕ are the subjects of interest. The frequency f Doppler energy detuning ΔE and hyperfine parameters of the source belongs among the parameters which can be fixed easily. Frequency generation is well controlled and very precise. In the case of the energy modulation control, the precision of $\pm\,0.2$ MHz was expected, which was supposed to be sufficient. Since the parameters of the radioactive source are not easy to be measured, we used, in accordance with the work [21], the single Lorentzian line shape having the linewidth $\Gamma_s = 1.2\Gamma_0$. For the absorber, we took the natural linewidth $\Gamma_a = \Gamma_0$ in account. But then, it is essential to measure precisely and fix the absorber effective thickness d_{eff} and hyperfine magnetic field B_{hf}. Since the obtaining of these values from the common transmission Mössbauer spectrum we find to be misleading, the better method of utilising the resonant detector is introduced in following Subsection 3.3.1.

The fixation of the eight parameters mentioned above is not enough. When trying to fit the data this way, there were significant differences in the motion amplitudes p, time resolutions σ_t and background amplitude levels A_{bcg} obtained from the first and second time histogram. However, it cannot be true, since these three parameters have to be the same for both time histograms. This reveals that there is a mutual correlation between these parameters. The significance of this relation is demonstrated on two measurements at 10 MHz, for driving voltage 1 V_{pp} and 2 V_{pp} in Figure 32. There are four different fitted curves for each time histogram when none, either σ_t or A_{bcg} or both parameters are fixed. Although the curves are almost indistinguishable and leaving all parameters free gives one of the best fit according to the chi square test, the triplet of parameters converges to significantly different values, see Table 2.

We believe that the most relevant results are obtained when the time resolution and the background level are precisely measured and fixed because then the fitted parameters from the both time histograms are maximally unified. Nevertheless, in few measurements (mostly for higher driving voltages) the parameter p differs by almost 13 % between the first and the second time histogram. We understand this as a result of possible errors in the fixed parameters or also the inhomogeneous motion of the absorber [27], whose influence on the shape of the radiation intensity in the time domain has not yet been properly investigated in this work.

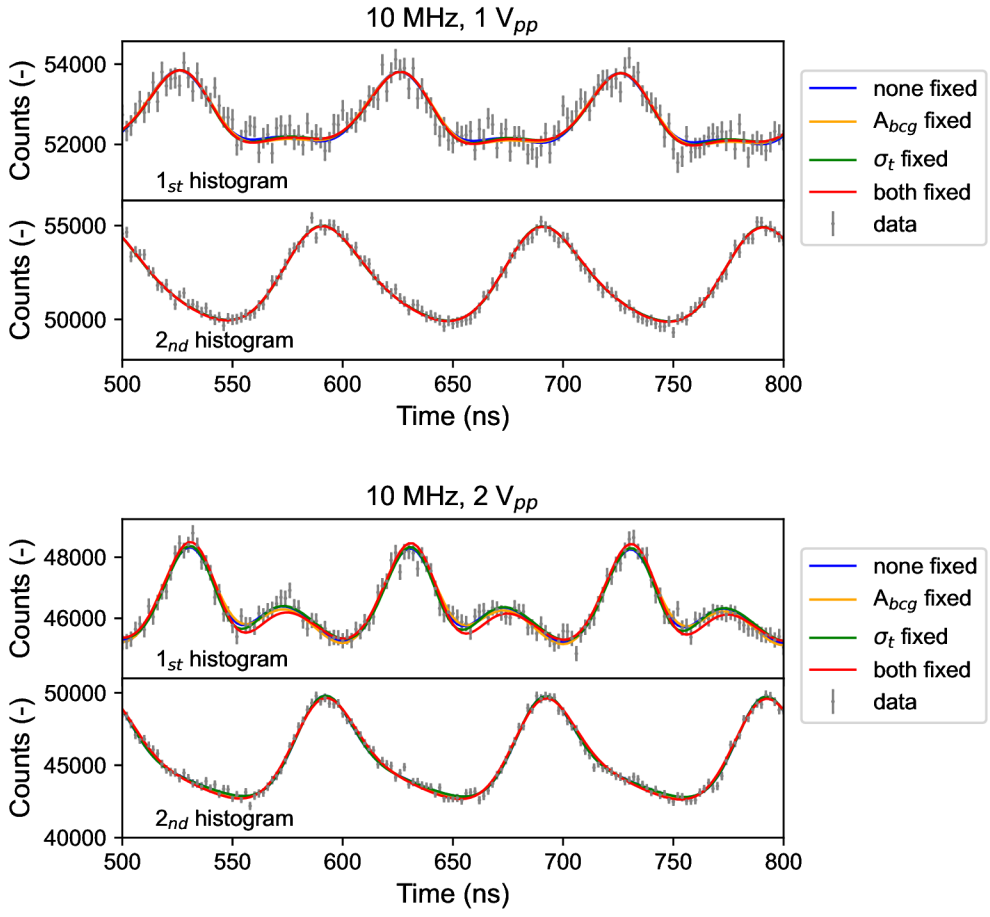

Figure 32: *Demonstration of the different curves fitted in two pairs of time histograms of the harmonically vibrating absorber at 10 MHz driven by voltage 1 V_{pp} and 2 V_{pp}. Individual fits differ in fixing the parameters A_{bcg} and σ_t.*

10 MHz, 1 V_{pp}								
Parameter	A_{bcg} (-)		σ_t (ns)		p (-)		δp (-)	$\bar{\mathrm{p}}$ (-)
Time histogram	1_{st}	2_{nd}	1_{st}	2_{nd}	1_{st}	2_{nd}		
None fixed	6,7	6,66	9,6	6,4	0,69	0,56	0,13	0,63
A_{bcg} fixed	**5,85**	**5,85**	8,2	3,1	0,56	0,46	0,10	0,51
σ_t fixed	6,31	6,28	**5,1**	**5,1**	0,52	0,51	0,01	0,52
A_{bcg} , σ_t fixed	**5,85**	**5,85**	**5,1**	**5,1**	0,49	0,47	0,02	0,48

10 MHz, 2 V_{pp}								
Parameter	A_{bcg} (-)		σ_t (ns)		p (-)		δp (-)	$\bar{\mathrm{p}}$ (-)
Time histogram	1_{st}	2_{nd}	1_{st}	2_{nd}	1_{st}	2_{nd}		
None fixed	6,9	6,8	7,1	3	1,08	0,87	0,21	0,98
A_{bcg} fixed	**5,85**	**5,85**	8,3	2	1,07	0,73	0,34	0,90
σ_t fixed	7,59	6,99	**5,1**	**5,1**	1,03	0,96	0,07	1,00
A_{bcg} , σ_t fixed	**5,85**	**5,85**	**5,1**	**5,1**	0,89	0,79	0,10	0,84

Table 2: *The correlated parameters p, σ_t and A_{bcg} obtained by fitting of two pairs of the time histograms shown in Figure 32. Values of the fixed parameters are in bold. Two last columns δp and $\bar{p}$ show the difference of the p value obtained from the first and the second time histogram and its average value respectively.*

After the fixation of the σ_t and A_{bcg}, last four parameters remain free in the fitted function. Specifically, besides the p and ϕ, the number of counts N, and the countrate constant C_{bcg} are fitted. All of these parameters are independent. The parameter p defines the shape of the intensity waveform and ϕ moves it along the time axis. Number of counts positions the time waveform according to y-axis and the countrate constant determines its inclination.

3.3.1 Absorber Parameters

The 25μm thick stainless steel foil from Alfa Aesar (production No. 41580, type 304) with a natural abundance (2.119 %) of ^{57}Fe, which was utilised in our experiments, was fitted as a magnetically split absorber with a weak hyperfine magnetic field. This more complicated model was applied because of the specific line shape and the relatively large FWHM linewidth of 5.4 MHz (0.47 mm/s). Simple fitting by single line transmission integral was unsatisfactory.

The hyperfine magnetic field and the effective thickness of the absorber can be determined by fitting the transmission Mössbauer spectrum with the transmission integral [89,90]. However, the better way is to measure these qualities by the means of the resonant Mössbauer spectroscopy [50,91] because the resonant detector [92,93] allows the resonant photons to be distinguished. This enables the level of the non-resonant background and the absolute amplitude of the absorption peak to be determined [50,94]. Thus, the effective thickness can be measured more precisely, because its value is much more sensitive to the amplitude of the absorption peak, in contrast to the common transmission Mössbauer spectrum, where the effective thickness is recognised mainly from the line broadening. The results obtained by both methods are compared in Figure 33.

The value of the effective thickness and the hyperfine magnetic field obtained from the resonant Mössbauer spectrum were 7.6±0.3 and 0.58±0.02 T respectively. These values were subsequently used to fit all radiation intensity waveforms. For comparison, fitting of the common Mössbauer spectrum gave the hyperfine magnetic field 0.57±0.03 T but the effective thickness was 8.7±0.3. In the other published experiments [21, 27, 28], the same method (assuming the non-split absorber) gave the effective thickness 5.2 for the same type of the absorber. In reality, however, the physical thickness of the foil may differ from the declared 25 μm. Also for this reason, it is always important to measure the effective thickness of the particular absorber used for the radiation intensity control.

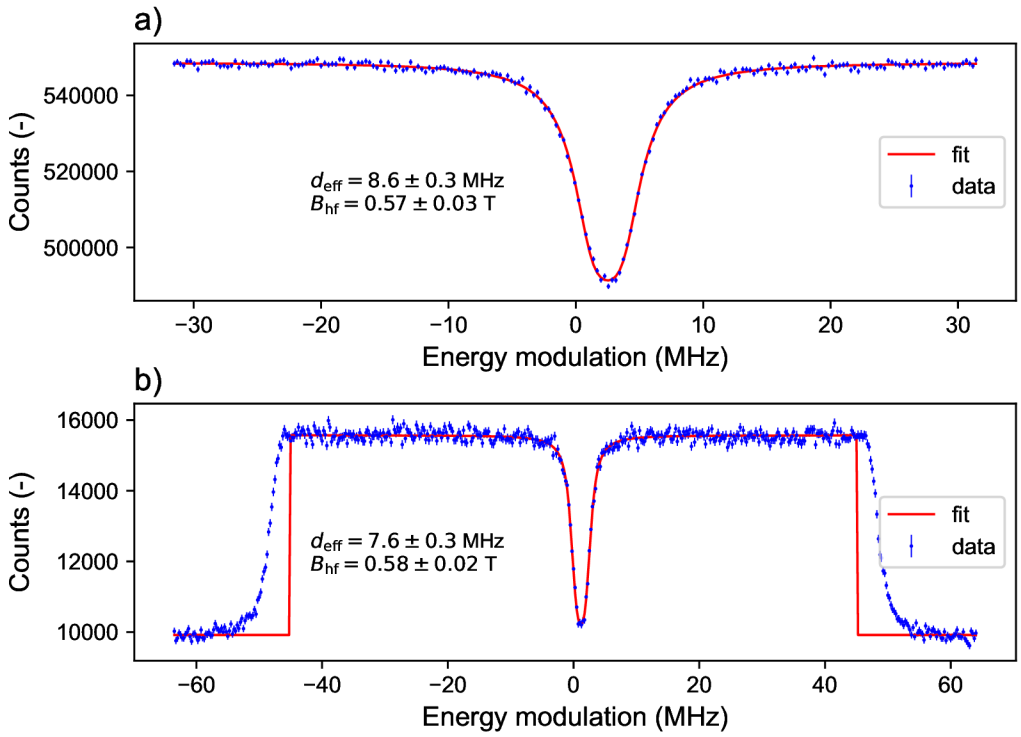

Figure 33: *Absorber effective thickness determined by transmission integral, part a), and by resonant Mössbauer spectroscopy, part b). Fitting procedure used in part b) is described in [50].*

The last parameter, the resonance line shift of the stainless steel absorber measured relative to the radioactive source, was $\delta = -2.5 \pm 0.1$ MHz. This parameter influences the absolute values of energies that have to be tuned in the experiment to adjust the required energy detuning ΔE, which is related to δ value.

3.3.2 Background Level Determination

The non-resonant background, which consist of the noise detections and the recoil 14 keV photons, can be determined with the above mentioned resonant detector, but it involves replacing the scintillation detector in the experiment. Fortunately, there is a simpler and more convenient way how to calculate this parameter from the experimentally measured absorption amplitude a_e (measurement effect) of the common Mössbauer spectrum and the amplitude of the theoretically calculated normalised

absorption a_n (without non-resonant background). Since we already know the effective thickness, the normalised absorption can be computed either by a normalised transmission integral or by the Python script for numerical simulations of radiation intensity in time provided in the Appendix. Both can provide the minimum value of the normalised absorption at the resonant energy. After that, it is a rule of three, which is shown in Figure 34. The ratio of the measured effect a_e and normalised absorption a_n is equal to the ratio of the full effect (equal to one) and normalised spectrum amplitude including the background. Writing this into the equation gives

$$\frac{a_e}{a_n} = \frac{1}{1 + A_{\mathrm{bcg}}} \tag{23}$$

from which the required A_{bcg} is expressed as

$$A_{\mathrm{bcg}} = \frac{a_n}{a_e} - 1\,. \tag{24}$$

For example, for our stainless steel absorber with $d_{\mathrm{eff}} = 7.6$ and $B_{\mathrm{hf}} = 0.58\,\mathrm{T}$, the normalised absorption amplitude is $a_n = 0.786$ and the measured effect was $a_e = 0.115$ (11.5 %) which gives $A_{\mathrm{bcg}} \doteq 5.8$. This value was so high in our experiments mainly due to the noise generated by scattered 122 keV photons. The measurement effect could be improved if the detector with better energy resolution, e.g. semiconductor, was utilised.

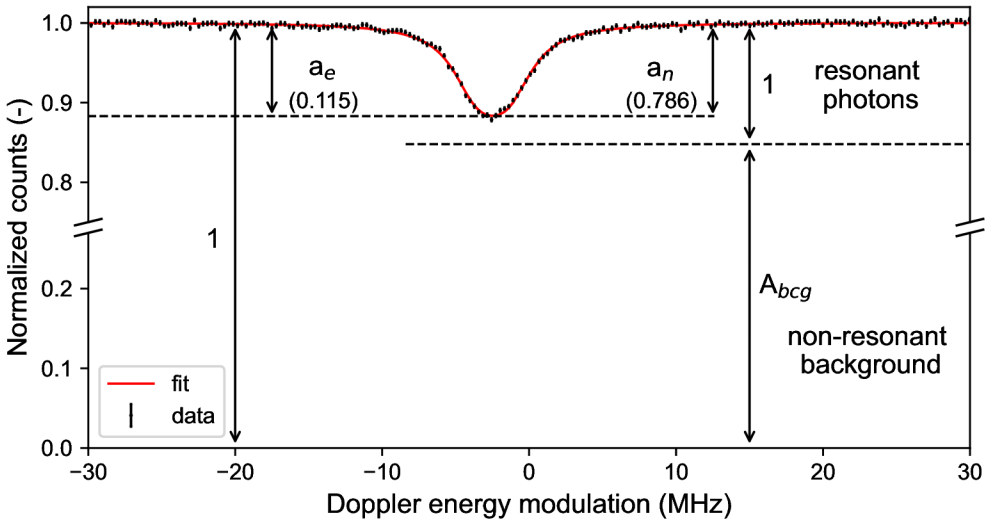

Figure 34: *Determination of non-resonant background A_{bcg} from the measurement effect a_e in the transmission Mössbauer spectrum and theoretically calculated normalised absorption amplitude a_n. Specifically, the case for the absorber with $d_{eff} = 7.6$ and $B_{hf} = 0.58\ T$ when the measured effect $a_e = 0.115$ corresponds to the $a_n = 0.786$ is depicted.*

Such a simple method has a weak point in the measurement of the Mössbauer effect, which depends on the geometry of the setup, the stability of the gamma radiation detector and the activity of the radioactive source. To ensure the maximum stability of the effect, the geometry has to be invariable. Additionally, a sufficiently stable detector has to be utilised. Specifically in the case of scintillation detectors, stable behaviour of the scintillator and stable amplification of the PMT signal are required,

because a possible change of the multichannel analysis spectrum can significantly influence the measurement effect. The last issue is the activity of the radioactive source, which decreases with time and thus causes a slow decrease of the signal-to-noise ratio. Fortunately, this change is relatively slow in the case of the ^{57}Co so it can be resolved by remeasuring the effect once a time. For example, our experiments with an unchanged setup took over two months and the effect was remeasured eleven times. Within this time, the effect gradually decreased from 11.9 % to 11.0 %. The measurement of the response function therefore began with the measurement of the Mössbauer effect, and subsequently a series of measurements were performed in the time domain. In order to keep the background value updated, the Mössbauer effect was remeasured approximately once a week.

3.3.3 Time Resolution Determination

A time resolution of the gamma photon detection by the scintillation detector is influenced by several factors such as the type of scintillation material, PMT type, amplifier bandwidth, pulse timing method or jitter of signal processing electronics. In our setup, the time resolution is more distorted by the leading edge timing method, which suffers from a walk [95], and less distorted by the time jitter of the PMT and the electronics. Besides that, the time resolution also depends on the pulse rise time, which is mainly determined by the type of the scintillation material, PMT rise time and amplifier bandwidth. Determination of all factors would provide the information on the total time resolution of the apparatus, but it would require a too complicated analysis of the individual parts. For this reason, the methods of measuring the overall time resolution of apparatus are interesting and preferred.

In most gamma radiation experiments, two gamma detectors are used and the coincidence time resolution can be measured. This involves some particles which are detected simultaneously in both detectors, which creates the prompt peak as shown for example in the measurement of excited state lifetime in Figure 20. This approach could be, in principle, applicable also in our case, but to obtain the required information, we need to be able to distinguish the contribution of each detector to the total coincidence time resolution. Determining the time resolution of the apparatus with a single gamma radiation detector is therefore not a simple task without an on-demand source of appropriate radiation, which is available only at synchrotron facilities.

An original solution for our problem was found again in the use of the interference effects of the gamma radiation induced by the harmonically vibrating absorber. The total time resolution of the apparatus can be obtained by the fitting of the radiation intensity waveforms. However, in order to get reliable results, the shape of the waveform has to be highly sensitive to the time resolution of apparatus and not strongly correlated with any other parameter. Such waveforms are double and triple gamma pulses which can be produced by the absorber vibrating at an amplitude p between 2 and 3 at a sufficiently high frequency (about 10 MHz) when the energy is tuned to the second or third spectral sideband [25]. For example, absorber vibrating harmonically at 10 MHz with amplitude $p = 2.5$ generates the gamma double pulses about 12 ns wide.

The depth of the valley between the pulses in the measured waveform is dominantly influenced by the time resolution of the apparatus, which is described by the parameter σ_t, see Figure 35, part a). On the other hand, the parameter p primarily

increases the amplitude of the pulses in this situation, see Figure 35, part b). So, in this case, the correlation between the p and σ_t parameters is lower unlike the frequency response measurements where both parameters have a similar effect on the amplitude of the oscillations or single pulses.

Experimentally, the time resolution of our apparatus was determined as the average of four values obtained by fitting two measurements conducted at 10 MHz with driving voltage 8 V_{pp}. In the first and the second measurement, the energy detuning was +30 MHz, −20 MHz and +27 MHz, −25 MHz respectively. Thus, three triple pulse and one double pulse time structures were acquired, see Figure 36. Afterwards, the data were fitted in the way described above in this section, except for the σ_t parameter which was left free. The resultant σ_t and p parameters were 5.1 ± 0.3 ns (FWHM 12.0 ns) and 2.54 ± 0.09 respectively. The value of time resolution was fixed to 5.1 ns for fitting all subsequent experiments. The relatively low uncertainty in determination of p parameter then confirms its lower correlation with the time resolution parameter unlike the single pulses fitting, compare the results with data in Table 2 in Section 3.3.

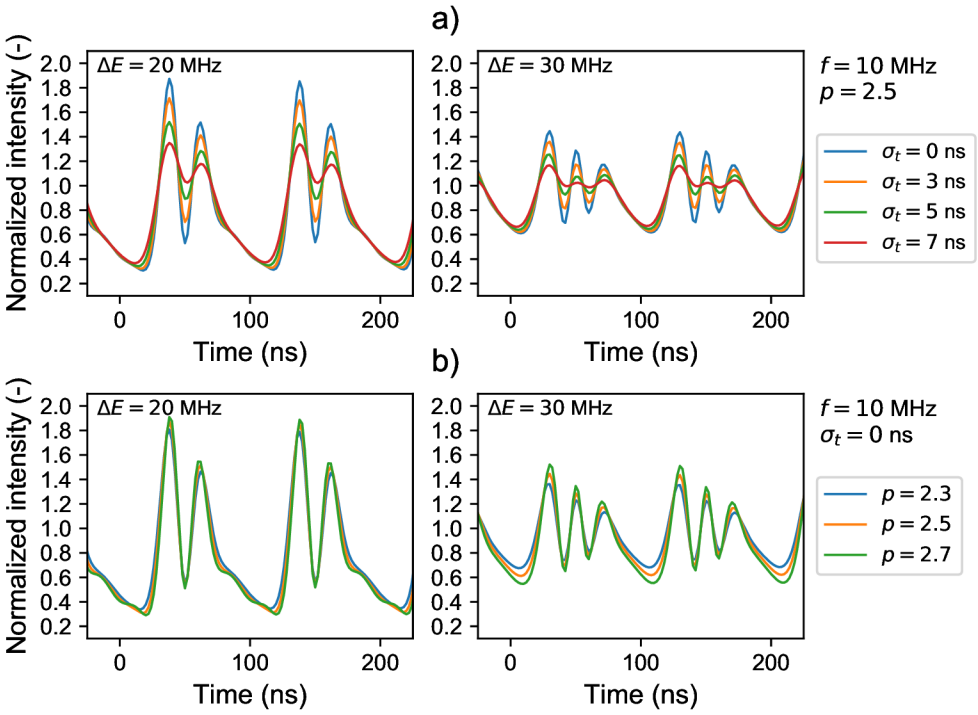

Figure 35: *Radiation intensity simulations demonstrating the impact of the time resolution parameter σ_t, part a), and the amplitude parameter p, part b), on the double and triple pulse structure.*

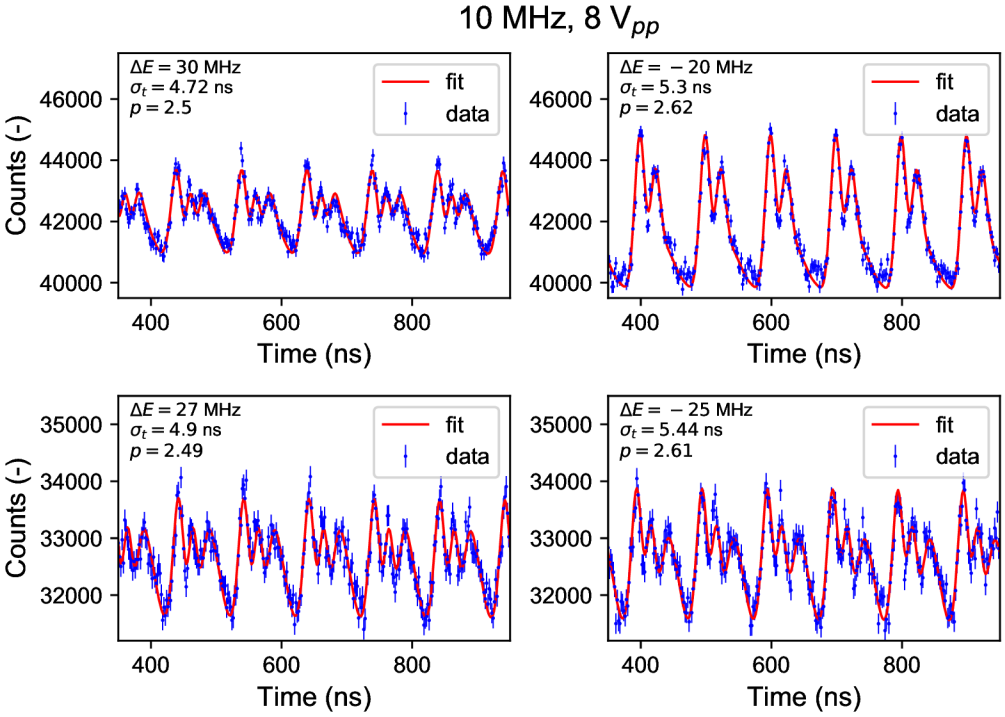

Figure 36: *Radiation intensity waveforms measured for determination of the apparatus time resolution. Double and triple pulse structures were obtained for four different levels of the energy detuning ΔE. Resultant time resolution σ_t was determined to be 5.1±0.3 ns. Fitted values of σ_t and p are shown in the particular graphs.*

3.4 Intensity Control Results

In this section, the results of the gamma radiation intensity control induced by four basic motion profiles of different amplitudes at divers energy detuning are presented to confirm the feasibility of the predictions made in Subsection 1.3.2. Specifically, the triangular, trapezoidal, square and bipolar-pulse like motion waveforms composed of six or twelve harmonics with fundamental frequency $f = 2\,\text{MHz}$ or $f = 1\,\text{MHz}$ respectively were utilised. For each of these, a corresponding driving voltage waveform had to be calculated. In this calculation, a particular ideal motion profile of specific amplitude was created first. Subsequently, this motion waveform was decomposed into Fourier series and reassembled from only six or twelve Fourier components, depending on the intended fundamental frequency. In this way, the required motion amplitudes and phases of each harmonic frequency were obtained. In the specific cases, the amplitudes of particular frequencies were manually reduced for the reasons that are described later in Subsection 3.4.2.

In the next step, the frequency response function was utilised to calculate the corresponding amplitudes and phases of the driving voltage waveform components. Since the frequency response was measured at certain points the values in between were linearly interpolated[10].

[10] A linear interpolation of the amplitude response function for low amplitudes of the driving voltage and motion was drawn from the origin to the first measured point. In the case of the phase response function, the interpolation value of the phase towards zero driving voltage was kept the same as in the nearest measured point.

The generated voltage waveforms were applied to the piezotransducer and the measured radiation intensity waveforms were compared to the predictions calculated from the expected motion profile. In practice, the parameters p and ϕ were fixed and only the number of counts N, and the countrate constant C_{bcg} were fitted. For the lower amplitude motions ($\Delta p < 3.5$, i.e. $< 48\,\mathrm{pm}$), which require relatively small amplitudes of higher frequency components, we got a very good agreement of the experiments with the predictions. These results are presented in following Subsection 3.4.1. In the opposite case, for the higher motion amplitudes, a deterioration of the intensity control was observed which is thought to be caused due to the nonlinear behaviour of the piezotransducer. These cases are presented and discussed in Subsection 3.4.2.

The radiation intensity waveforms presented in the following subsections are depicted in the normalised form $I_n(t)$, which shows approximately the normalised intensity $I(t)$ convolved with the time resolution function. Written in the equation, the $I_n(t)$ is obtained when the measured data $I_{exp}(t)$ are normalised and the background is subtracted as follows

$$I_n(t) = I_{\mathrm{exp}}(t) \left(\frac{1 + A_{\mathrm{bcg}}}{N e^{-\frac{t}{C_{\mathrm{bcg}}}}} \right) - A_{\mathrm{bcg}}\,. \tag{25}$$

This form was chosen because it allows comparison of intensity levels between the individual measurements.

The origin of the time axis of the displayed data is related to the beginning of the motion profile period. It is possible to notice that not the full $2\,\mu$s but a shorter time histogram is displayed. This is due to the cutting of the first 340 ns of the time histograms because the numerical fit in this region was disrupted by numerical artefacts.

3.4.1 Results of Individual Motion Profiles

Triangular Motion: Experimental results measured for two triangular motion profiles, which were composed of twelve and six harmonics with $f = 1$ and $f = 2\,\mathrm{MHz}$ respectively, are shown in Figure 37. In both measurements, the energy detuning of the source was $\Delta E = 3\,\mathrm{MHz}$ (foot of the resonant line). The absorber position changed of approximately 120 pm and 60 pm in 500 ns and 250 ns respectively, which gives the velocity $\pm 0.23\,\mathrm{mm/s}$ corresponding Doppler to energy modulation $\pm 2.8\,\mathrm{MHz}$. Thus the energy of the incident radiation was tuned by the motion of the absorber near to the resonance ($\Delta E = 0.2\,\mathrm{MHz}$) when moving in one direction and more out of the resonance ($\Delta E = 5.8\,\mathrm{MHz}$) in the other direction. Specifically, these results show that the triangular motion profile could be used for fast gating of the gamma radiation intensity with an approximate duty cycle of 50 %.

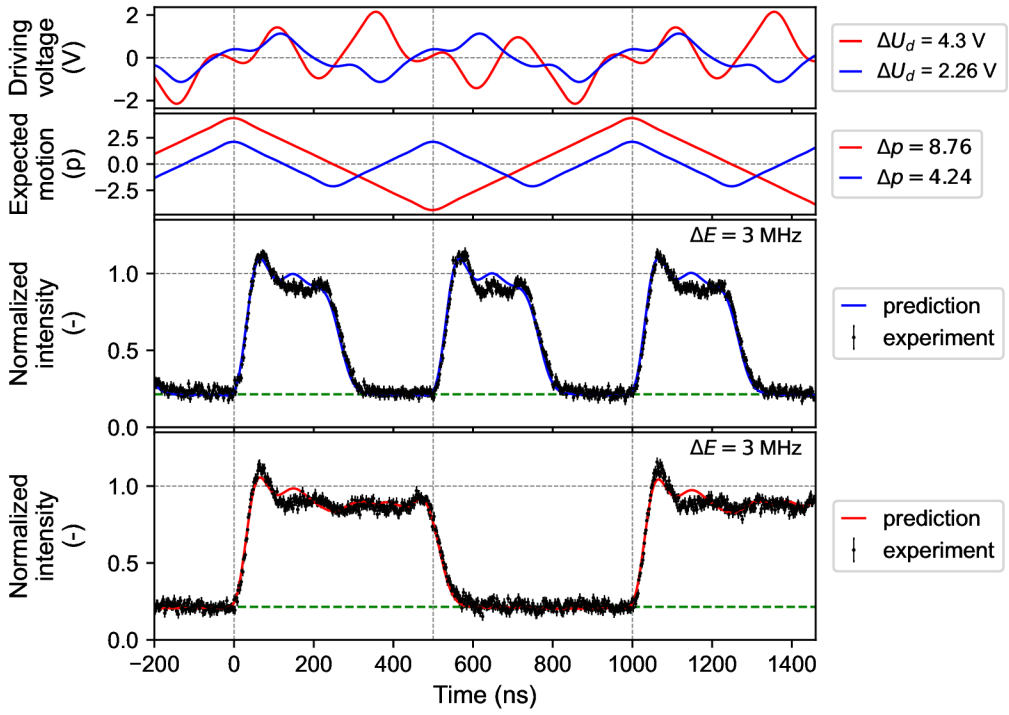

Figure 37: *Radiation intensity waveforms (black) induced by the absorber vibrating according to the triangular motion profiles. The corresponding driving voltage waveforms and predicted radiation intensities for the triangular motion profile consisting of 12 harmonics($f = 1\,MHz$) and 6 harmonics ($f = 2\,MHz$) are drawn in red and blue lines respectively. A green dashed line labels the radiation intensity in the resonance.*

Trapezoidal Motion: The single gamma pulses and the short-time absorption induced by two trapezoidal motion profiles are depicted in Figure 38. When the energy of the photons was tuned close to resonance ($\Delta E \approx 0.5$–1 MHz) the single gamma pulses about 55 ns wide (FWHM) with intensity exceeding the incident level 1.5 times were generated. Conversely, if the energy of the incident photon was tuned about 5 MHz outside the resonance, the absorption was induced for 60–80 ns.

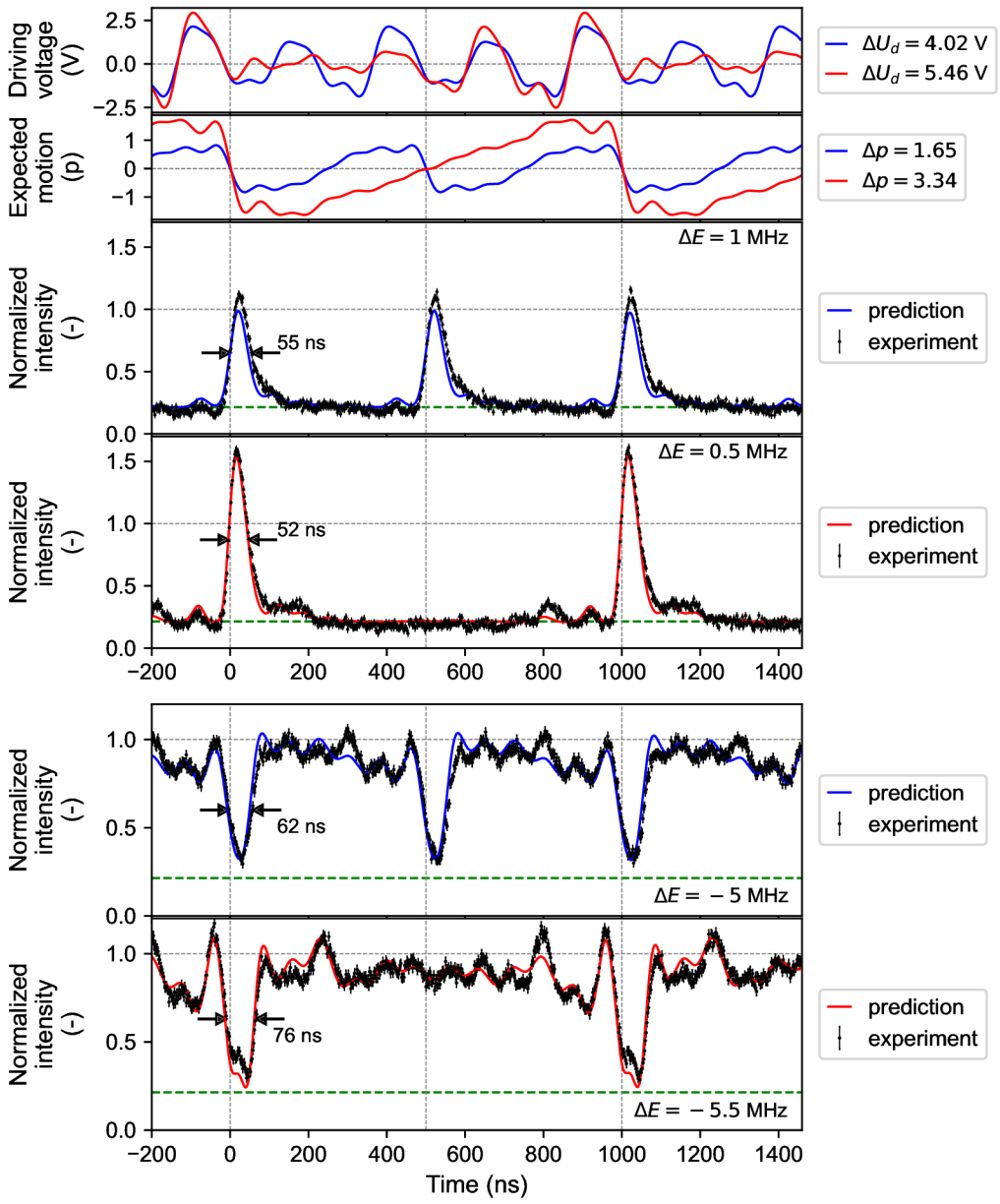

Figure 38: *Radiation intensity waveforms (black) of the single gamma pulses (the first two intensity graphs) and short-time induced absorption (the last two intensity graphs) generated by trapezoidal motion profiles of the absorber. The corresponding driving voltages and predicted radiation intensities for the trapezoidal motion profiles consisting of 12 harmonics ($f = 1$ MHz) and 6 harmonics ($f = 2$ MHz) are drawn in red and blue lines respectively. A green dashed line labels the radiation intensity in the resonance.*

Square Motion: Doubling of the gamma pulses frequency is demonstrated on the square motion profile. If the energy of the incident photons was tuned exactly to the resonance, then the both absorber jumps back and forth created almost identical single gamma pulses 50 ns wide (FWHM) with the intensity enhanced approximately 1.5 times. However, the fast jumps at the square motion profile can be utilised also to induce the short-term absorption same as the trapezoidal motion profile if the energy is tuned out of the resonance. However, only one direction jump have the required effect, see Figure 39.

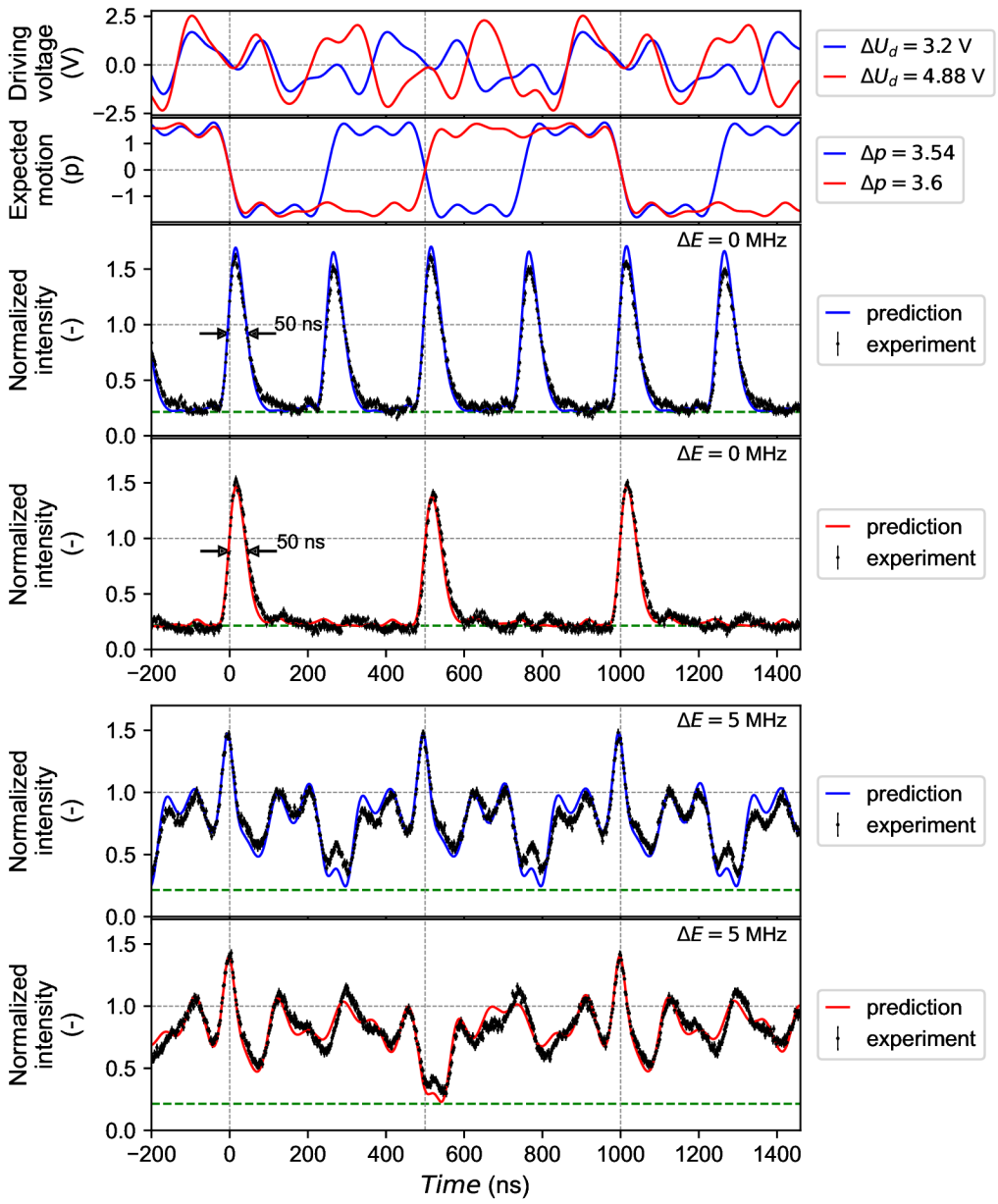

Figure 39: *Radiation intensity waveforms (black) of the single gamma pulses (the first two intensity graphs) and short-term induced absorption (the last two intensity graphs) generated by square motion profiles of the absorber. The corresponding driving voltages and predicted radiation intensities for the trapezoidal motion profile consisting of 12 harmonics ($f = 1$ MHz) and 6 harmonics ($f = 2$ MHz) are drawn in red and blue lines respectively. A green dashed line labels the radiation intensity in the resonance.*

Bipolar Pulse Motion: The generation of the single and double gamma pulses by the bipolar pulse motion profile, when the energy of the incident photons was tuned to the left ($\Delta E = -1\,\mathrm{MHz}$) and right ($\Delta E = 1.5\,\mathrm{MHz}$) side of the resonance, is shown in Figure 40. The positive energy detuning resulted in a generation of the single pulses with FWHM of 44 ns and the negative detuning created the double pulses, where each pulse has a FWHM about 30 ns.

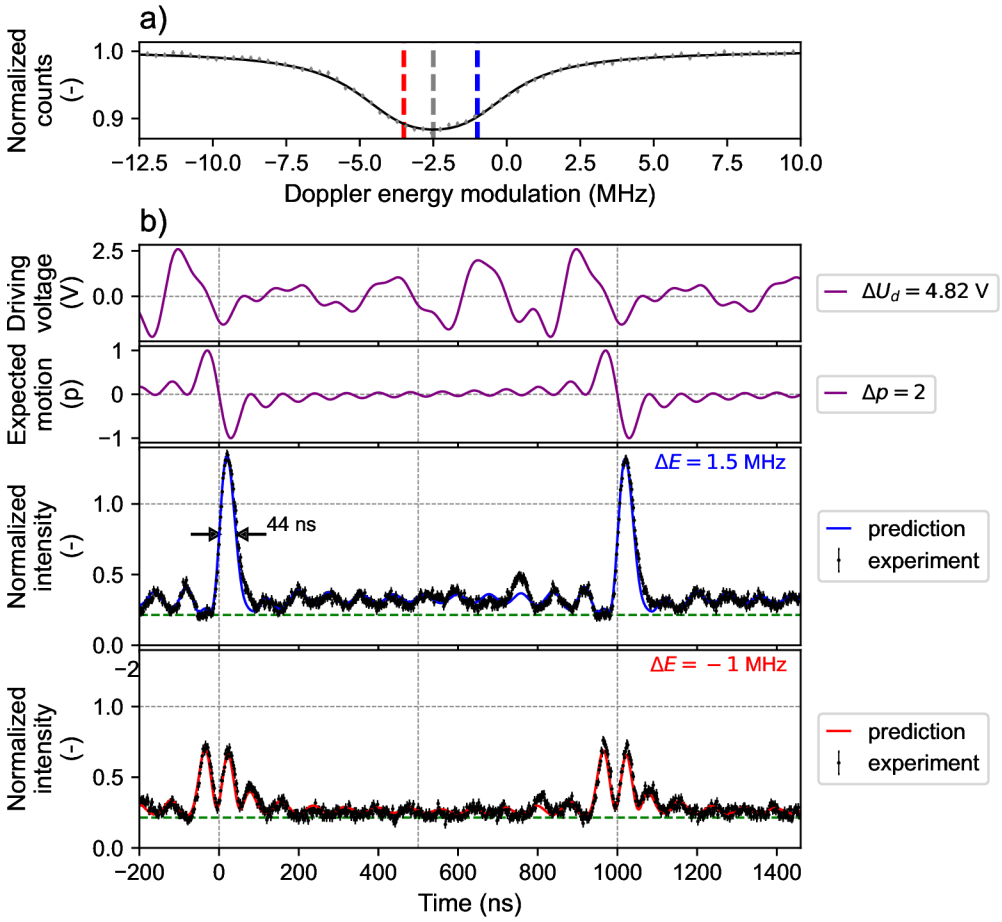

Figure 40: *Mössbauer spectrum of the absorber, part a), and radiation intensity waveforms of the single and double gamma pulses generated by the bipolar pulse shaped motion profile of the absorber for different energy detuning labelled by blue and red lines, part b). A green dashed line labels the radiation intensity in the resonance.*

3.4.2 Imperfections and Limits

A good agreement of the predictions with the experiments, which were shown in the previous section, was mostly achieved by a manual suppression of the amplitudes of the 4 MHz and 5 MHz frequency, i.e. the frequencies of the minimum amplitude response, recall Figure 28. Although this action slightly altered the expected motion profile, the effect on the measured intensity waveform and the maximum amplitude of the driving voltage was considerable. The impact of suppressing both or only one of the frequencies is shown in Figures 41 and 42 respectively. The amplitudes were reduced to the half except for the motion profile consisting of even frequencies, where the amplitude at 4 MHz was decreased to one third. The observed behaviour remains unexplained, but we offer a few hypotheses. The first is that the amplitude response at the local minimum actually varies rapidly in time and we are only measuring the average mechanical response. It means that the motion of the Mössbauer absorber is not ideally periodic and its deflections from the average cause the substantial changes in the radiation intensity waveforms. The second hypothesis is that we encounter some nonlinear behaviour of the piezotransducer at these frequencies.

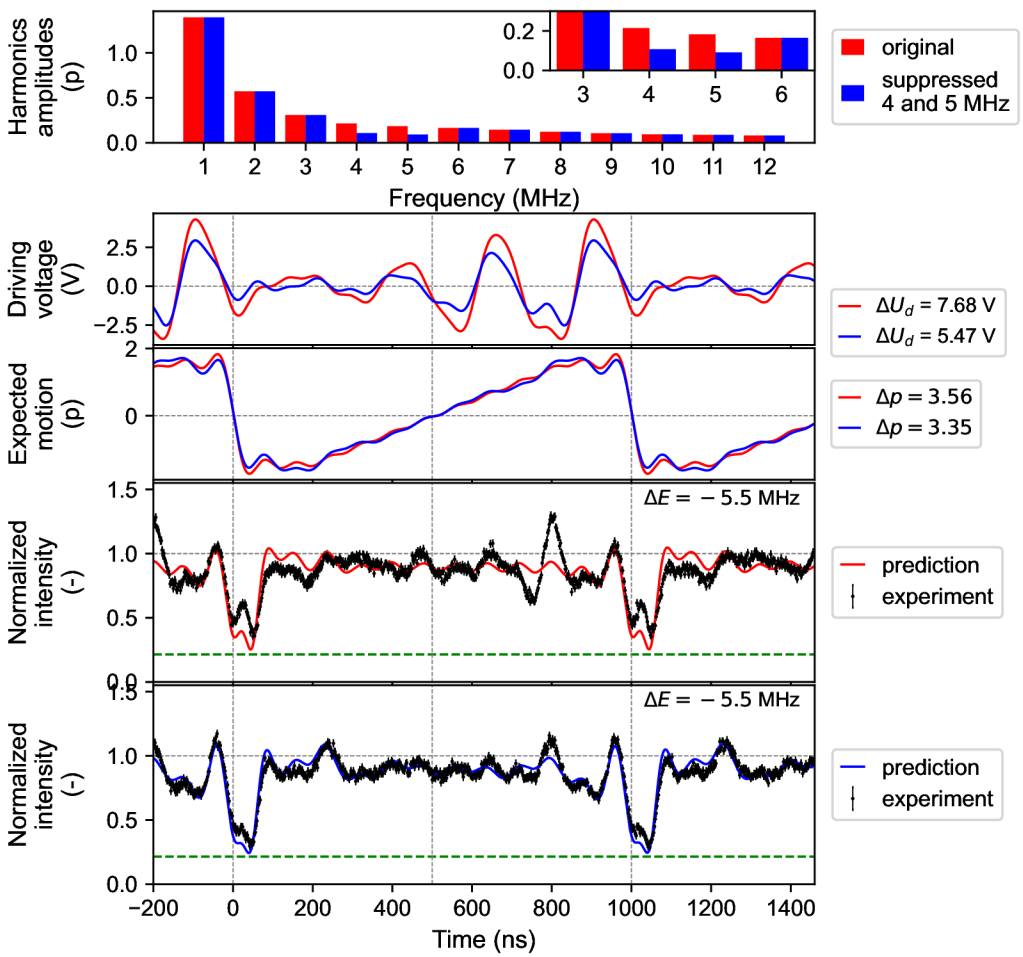

Figure 41: *Influence of the 4 and 5 MHz frequency suppression on the radiation intensity control. Amplitudes of both frequencies were decreased to the half. Corresponding harmonics amplitudes, driving voltage waveform, expected motion profile and predictions are labelled by red and blue colour.*

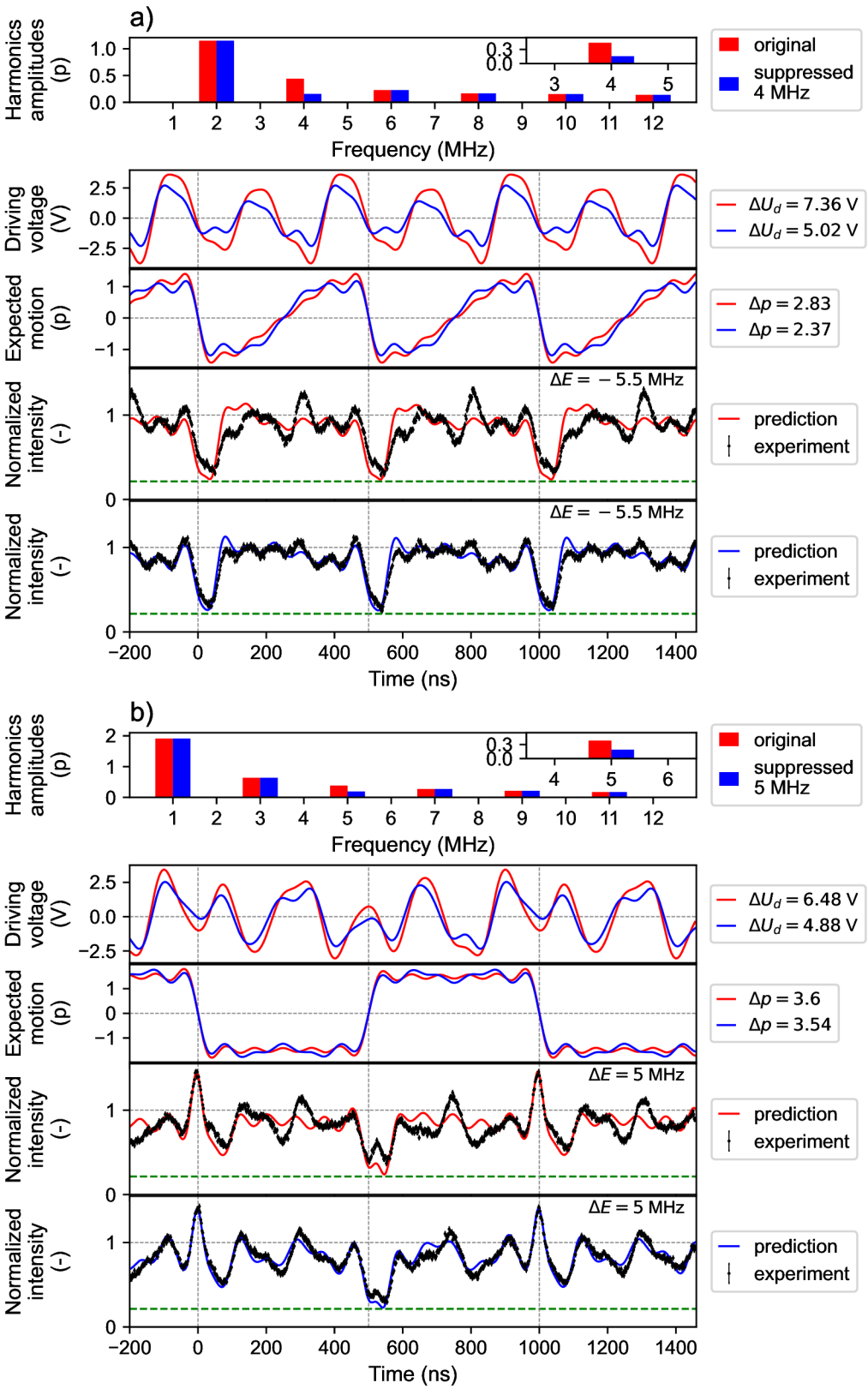

Figure 42: *Influence of merely 4 MHz, part a), and 5 MHz, part b), frequency suppression on the radiation intensity control. Amplitude of 4 MHz was reduced to the third and 5 MHz to the half. The corresponding harmonics amplitudes, driving voltage waveform, expected motion profile and predictions are labelled by red and blue colour.*

The second hypothesis is further supported by the fact that the attempts to control the radiation intensity using higher amplitude motion profiles with $\Delta p > 3.5$ were unsuccessful. Even though the two frequencies mentioned above were suppressed to a sufficiently low level (to the half or third), the discrepancy between the predictions and the experiment was larger when the absorber motion amplitude increased, see Figure 43. It is possible that we have omitted other problematic frequencies, but we think that we got into a nonlinear region of the piezotransducer. Nevertheless, it is evident that the higher absorber jumps led to the generation of more narrower (25 ns FWHM) and more intensive pulses exceeding the input intensity 1.7 times.

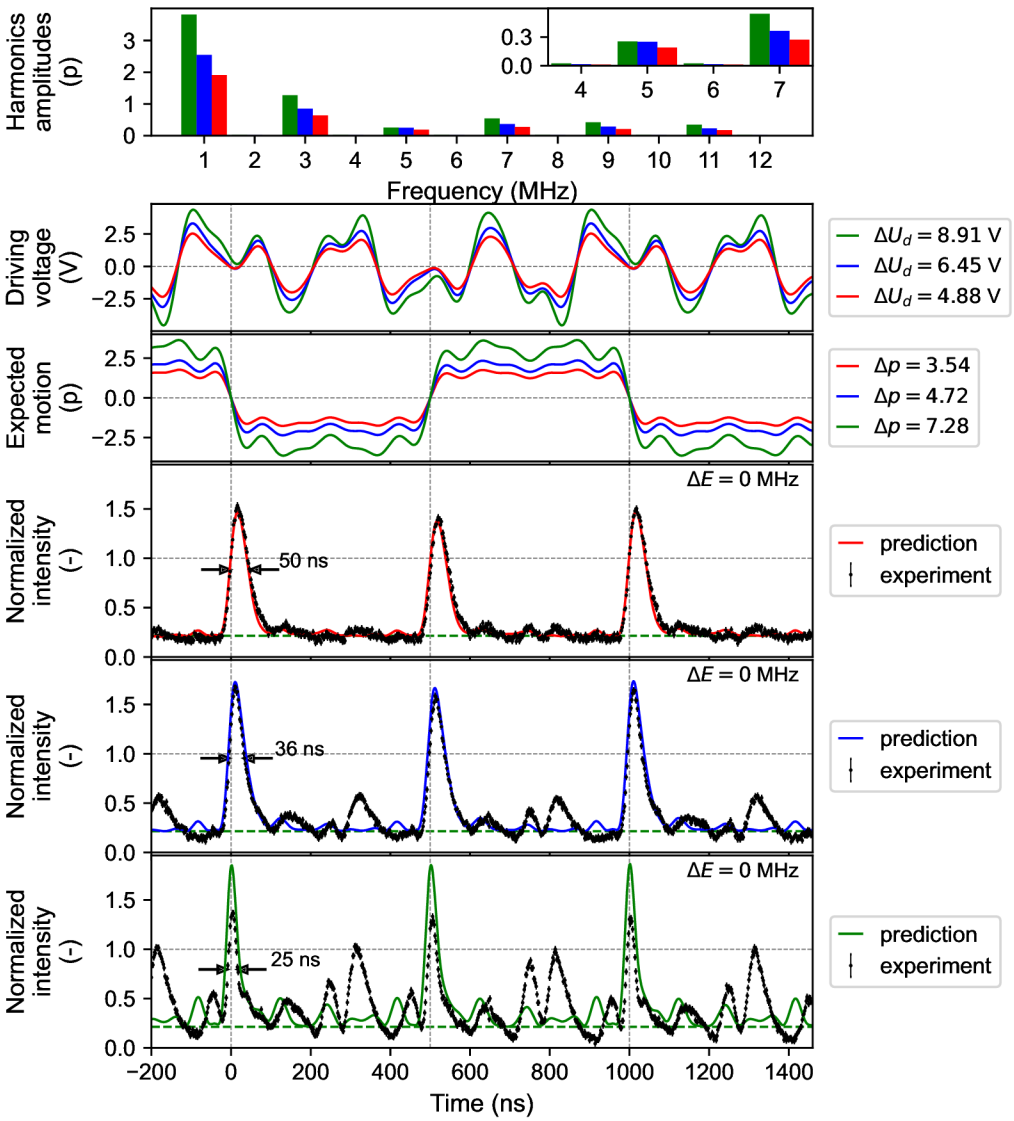

Figure 43: *Radiation intensity control for different amplitudes of the square-like motion profiles. Corresponding harmonics amplitudes, driving voltage waveform, expected motion profile and predictions are labelled by green, blue and red colour. Amplitude of the 5 MHz frequency was reduced to the third in the case of green waveform and to the half for the blue and red waveform.*

When searching for the cause of the deterioration of the radiation intensity control, a potential influence of the inhomogeneous absorber motion (incoherent model), see [27], was examined. Several experiments with different size of the square shape apertures (from 3x3 mm up to 8x9 mm) in front of the absorber were conducted, but any difference above the noise level was not observed. Next, the effect of the driving voltage waveform offset (±2 V) was studied, but it had no influence on the radiation intensity waveform. Only the comparison of the presented results indicates a correlation between the quality of the radiation intensity control and the maximum amplitude of the driving voltage waveform. It is certain that achieving the high intensity gamma pulses predicted in Subsection 1.3.2 is limited by the electromechanical properties of used piezotransducer.

3.5 Potential Applications and Further Development

The interference effects induced by the harmonically vibrating Mössbauer absorber bring a variety of potential applications. In this work, it was shown that the interference of the 14 keV gamma photons from a ^{57}Co source can be used for measuring the harmonic vibrations on the picometre scale at frequencies in the range of several megahertz. If less used Mössbauer sources [46, 96] were exploited, this concept could be further developed to measure the vibrations amplitudes in femtometre range and kilohertz or, contrarily, gigahertz frequencies. Thus, gamma radiation interference could be an interesting tool for the research of the fast low-amplitude vibration modes of the piezoelectric materials and their frequency characterisation. Furthermore, it was presented that the radiation intensity time structures of the specific shapes such as double and triple pulses can be used to determine the time resolution of the single gamma radiation detector.

The generation of the high-intensity, in-time narrow single gamma pulses by the presented technique enables the development of a table-top radioactive gamma pulse source. Such an instrument would be used to study nuclear quantum dynamics, and to perform the pump probe and interferometric experiments with gamma photons. Moreover, if a stainless steel absorber is replaced by the magnetically split one, it allows to generate polarized gamma pulses[11], which could be utilised, besides the gamma optics experiments, also for the construction of the table-top polarised Mössbauer spectrometer. Note that the method of gamma radiation control presented in this work is independent of the source activity, so the gamma pulser can reach high intensities.

The shaping of the gamma radiation intensity into the forms different from the single pulses brings other applications. The phenomenon of the short-time induced absorption observed in this work suggests the possibility of development of a time and energy selective gamma radiation detector. Moreover, a generation of the multi-pulse structures could be a subject of interest in the area of gamma single-photon mode entanglement, where in-time separated modes in the form of pulses were proposed [34]. In general, the arbitrary driving voltage should allow to generate various waveforms of the gamma radiation intensity, see Figure 44 where an example of arbitrary motion profile leads to a generation of three different pulses. Thus, sequences of the multiple structures (single pulses, double pulses, absorption) of various amplitudes, widths and time positions could be generated. In addition, if the non-periodic motions of the

[11] Few experiments with a harmonically vibrating magnetic α-iron foil have been already performed in our research group and the pulses with partially separated Π and σ polarisations were observed.

absorber, e.g. single jumps, were properly controlled, it would also be possible to manipulate the individual gamma photons in real time. This kind of gamma-photon control could be potentially applied in the field of quantum computing, quantum memories or quantum cryptography.

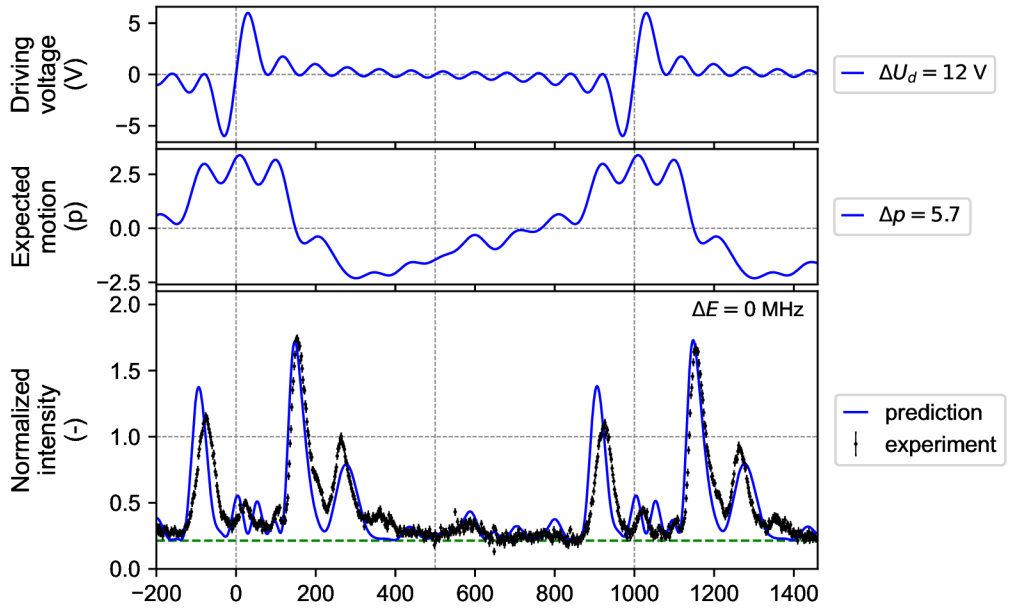

Figure 44: *Example of arbitrary radiation intensity waveform controlled by the bipolar-pulse shaped driving voltage. The expected absorber motion profile, which creates three gamma pulses with diverse amplitude in different times, was calculated using the driving voltage and frequency response function.*

The presented method of gamma radiation control can be further developed both practically and theoretically. On the technological side, the piezotransducers could be improved to manage larger amplitudes at higher frequencies. This involves not only adjusting the mechanical design of the PVDF foils or the absorber, but also the search for better piezoelectric materials. For example quartz-based ETNA piezotransducers utilised in [97] seem to be a promising candidate. It would also be quite interesting to find the piezoelement that manages to move the radioactive source at high frequencies, since the situation of vibrating source or absorber is equivalent. Additionally, some cooling technology ensuring a lower or even stable temperature could be useful to solve the problem with heating of the piezotransducer.

Frequency response of the piezotransducer could be further improved by decreasing the weight of the absorber. Assuming that 12 mg stainless steel absorber (on our piezotransducer) moves harmonically with 30 pm amplitude at 10 MHz frequency, the piezofoil has to exert the force of about 1 kN to move the absorber. If enriched absorbers were utilised, the weight could be reduced by a factor of about forty seven (2.119 % natural abundance ^{57}Fe) for the same effective thickness. Such a change could have a significant impact on the piezotransducer frequency response. In addition, the physical thickness of the enriched absorbers ranges from several hundreds of nanometres up to only a few micrometres, which means a significant reduction of the electronic absorption losses of the gamma radiation in the absorber. On the other hand, the production of such a thin foils is not common and, in general, a manual

gluing of the metal foils, especially the extra thin ones, to the piezoelements requires a skill. For this reason, other techniques such as sputtering or electrolysis of the absorber on the surface of the piezoelement could be used, which could also improve the reproducibility of the piezotransducers (compared to the manual gluing).

Next, the methodology of frequency response measuring could be accelerated by the application of more frequencies simultaneously. Indeed, it has to be ensured that the system behaves linearly, but the measurement of the response function could be reduced to units of measurements instead of several tens. However, this requires much more complicated fitting, which could perhaps be simplified if the theoretical description of the radiation intensity control by a multi-tone vibrating absorber was mastered analytically. The simplification of the calculation would also help to solve the inverse problem of what shape of motion profile has to be applied in order to obtain the required radiation intensity profile. In this work, only four basic motion profiles were introduced, but it is not excluded that there are other arbitrary motion profiles which allow to generate different radiation intensity structures as indicated in Figure 44. For example, the better motion profile could be found to acoustically induce the absorption of rectangular shape and specific time width.

Finally, we suggest some additional hints. In principle, the radiation control method could be further improved by adding more individually vibrating absorbers. Such a setup, where not only singlet but also doublet or sextet absorbers are employed in the experiment, could be interesting for a further investigation of gamma radiation slowing down [98]. More vibrating absorbers are also interesting from the point of view of the nuclear dynamics when the gamma photon interaction with two nuclei ensembles moving in opposite direction during the interaction, can be investigated.

Conclusion

In the present work, the coherent control of gamma radiation intensity by the Mössbauer absorber which vibrates according to motion profiles defined by Fourier series was described from the simulations to the experiment. Although no deeper analytical advance was made, the resonant scattering in the absorber vibrating with the arbitrary motion profile was solved numerically. The optimised Python script was appended to this work.

The numerical calculations were used to investigate the potential of gamma radiation intensity control specifically by triangular, trapezoidal, square and bipolar pulse motion profiles. The triangular motion profile was used to demonstrate that the gamma resonant scattering in the vibrating absorber can be understood as a result of the additional interference effect induced by the change of energy modulation within the excitation time. Further simulations showed that the variation of the absorber motion profile provides much broader possibilities for controlling the temporal properties of the gamma radiation intensity. Besides the narrow high-intensity single gamma pulses, short-time acoustically induced absorption and well separated high-intensity double pulses were predicted.

The necessary equipment for performing the radiation intensity control experiments was developed. Within this, the dual-channel Mössbauer spectrometer was upgraded to a universal DAQ system for nuclear quantum experiments, allowing to measure besides energy spectra also time histograms and TDMS spectra. The key part of the upgrade was implementation of the TDC and asynchronous amplitude discriminator in FPGA, which ensures data processing on hardware level. Further, the piezodriver and piezotransducer were created to move the Mössbauer absorber at megahertz frequencies and picometre amplitudes.

To control the motion profile of the absorber, it was necessary to measure frequency response of the piezotransducer system. For this purpose, the methodology based on gamma radiation scattering in the harmonically vibrating absorber was developed and described in detail. Using the frequency response function, the input driving voltage waveforms for the piezotransducer were calculated to generate the required motion profiles of the absorber. The predicted shaping of the gamma radiation intensity into single pulses, double pulses and short-time acoustically induced absorption was experimentally proven. For lower amplitudes of the absorber motion ($\Delta p < 3.5$), the results were in good agreement with the predictions. For higher amplitudes, the imperfections and limitations, specifically a nonlinearity of the piezotransducer, were discussed.

Possible applications of the presented technique for controlling the intensity of gamma radiation include the construction of the table-top source of gamma pulses, which could be even polarised, opening the doors to the table-top polarised Mössbauer spectrometer. The gamma pulses could be further exploited for studying the nuclear quantum dynamics or single photon quantum entanglement. At the end, the possible improvements were suggested. The intensity control technique can be further developed both experimentally and theoretically. For example, a proper analytical description is lacking, better piezotransducers and absorbers could be used, or the concept could be extended to more vibrating absorbers.

References

[1] N. N. Greenwood and T. C. Gibb, *Mössbauer Spectroscopy*. Springer Netherlands, 1971.

[2] G. N. Belozerski, *Mössbauer studies of surface layers*. Studies in Physical and Theoretical Chemistry, London, England: Elsevier Science, 1993.

[3] P. Gütlich, E. Bill, and A. X. Trautwein, *Mössbauer Spectroscopy and Transition Metal Chemistry*. Springer-Verlag Berlin Heidelberg, 2011.

[4] T. J. Bürvenich, J. Evers, and C. H. Keitel, "Nuclear quantum optics with X-Ray laser pulses," *Phys. Rev. Lett.*, vol. 96, p. 142501, 2006.

[5] J. Odeurs, G. Hoy, Y. Rostovtsev, and R. Shakhmuratov, "Towards more relaxed conditions for a gamma-ray laser: Methods to realize induced transparency for nuclear resonant gamma radiation," *Laser & Photonics Reviews*, vol. 4, no. 1, pp. 1–20, 2010.

[6] W. Liao, A. Pálffy, and C. H. Keitel, "Coherent storage and phase modulation of single hard-x-ray photons using nuclear excitons," *Phys. Rev. Lett.*, vol. 109, p. 197403, 2012.

[7] W. Liao, A. Pállfy, and C. H. Keitel, "Three-beam setup for coherently controlling nuclear-state population," *Phys. Rev. C*, vol. 87, p. 054609, 2013.

[8] E. Kuznetsova and O. Kocharovskaya, "Quantum optics with X-rays," *Nature Photonics*, vol. 11, no. 11, pp. 685–686, 2017.

[9] K. P. Heeg, A. Kaldun, C. Strohm, C. Ott, R. Subramanian, D. Lentrodt, J. Haber, H. Wille, S. Goerttler, R. Rüffer, C. H. Keitel, R. Röhlsberger, T. Pfeifer, and J. Evers, "Coherent X-ray-optical control of nuclear excitons.," *Nature*, vol. 590, pp. 401–404, 2021.

[10] F. J. Agee, "Review of induced gamma emission and gamma-ray laser research," *Hyperfine Interactions*, vol. 143, no. 1, pp. 1–6, 2002.

[11] L. Rivlin, "Nuclear gamma-ray laser: the evolution of the idea," *Quantum Electronics*, vol. 37, no. 8, p. 723, 2007.

[12] S. L. Ruby and D. I. Bolef, "Acoustically modulated γ rays from Fe^{57}," *Phys. Rev. Lett.*, vol. 5, pp. 5–7, 1960.

[13] T. E. Cranshaw and P. Reivari, "A Mössbauer study of the hyperfine spectrum of ^{57}Fe, using ultrasonic calibration," *Proceedings of the Physical Society*, vol. 90, no. 4, p. 1059, 1967.

[14] P. Helistö, I. Tittonen, M. Lippmaa, and T. Katila, "Gamma echo," *Phys. Rev. Lett.*, vol. 66, pp. 2037–2040, 1991.

[15] I. Tittonen, P. Helistö, M. Lippmaa, and T. Katila, "Mössbauer gamma echo," *Hyperfine Interactions*, vol. 71, 1992.

[16] I. Tittonen, M. Lippmaa, P. Helistö, and T. Katila, "Stepwise phase modulation of recoilless gamma radiation in a coincidence experiment: Gamma echo," *Phys. Rev. B*, vol. 47, pp. 7840–7846, 1993.

[17] G. J. Perlow, "Quantum beats of recoil-free γ radiation," *Phys. Rev. Lett.*, vol. 40, pp. 896–899, 1978.

[18] R. N. Shakhmuratov, F. Vagizov, and O. Kocharovskaya, "Radiation burst from a single γ-photon field," *Phys. Rev. A*, vol. 84, p. 043820, 2011.

[19] R. N. Shakhmuratov, "Transformation of subradiant states to superradiant states in a thick resonant medium," *Phys. Rev. A*, vol. 90, p. 013819, 2014.

[20] F. Vagizov, V. Antonov, Y. V. Radeonychev, R. N. Shakhmuratov, and O. Kocharovskaya, "Coherent control of the waveforms of recoilless γ-ray photons," *Nature*, vol. 508, no. 7494, pp. 80–83, 2014.

[21] Y. V. Radeonychev, I. R. Khairulin, F. G. Vagizov, M. Scully, and O. Kocharovskaya, "Observation of acoustically induced transparency for γ-ray photons," *Phys. Rev. Lett.*, vol. 124, p. 163602, 2020.

[22] I. R. Khairulin, Y. V. Radeonychev, V. A. Antonov, and O. Korchayovskaya, "Acoustically induced transparency for synchrotron hard x-ray photons," *Sci Rep*, vol. 11, no. 7930, 2021.

[23] P. Helistö, E. Ikonen, T. Katila, and K. Riski, "Coherent transient effects in Mössbauer spectroscopy," *Phys. Rev. Lett.*, vol. 49, pp. 1209–1213, 1982.

[24] V. A. Antonov, Y. V. Radeonychev, and O. Kocharovskaya, "γ-ray-pulse formation in a vibrating recoilless resonant absorber," *Phys. Rev. A*, vol. 92, p. 023841, 2015.

[25] R. N. Shakhmuratov, F. G. Vagizov, V. A. Antonov, Y. V. Radeonychev, M. O. Scully, and O. Kocharovskaya, "Transformation of a single-photon field into bunches of pulses," *Phys. Rev. A*, vol. 92, p. 023836, 2015.

[26] R. N. Shakhmuratov, "Transformation of the frequency-modulated continuous-wave field into a train of short pulses by resonant filters," *Phys. Rev. A*, vol. 95, p. 033805, Mar 2017.

[27] R. N. Shakhmuratov and F. G. Vagizov, "Application of the Mössbauer effect to the study of subnanometer harmonic displacements in thin solids," *Phys. Rev. B*, vol. 95, p. 245429, 2017.

[28] R. N. Shakhmuratov and F. G. Vagizov, "Mössbauer method for measuring sub-angstrom displacements of thin films," *JETP Letters*, vol. 108, no. 11, p. 772–776, 2018.

[29] S. S. Wang, Y. G. Ma, X. G. Cao, D. Q. Fang, and C. W. Ma, "Hard-photon production and its correlation with intermediate-mass fragments in a framework of a quantum molecular dynamics model," *Phys. Rev. C*, vol. 102, p. 024620, 2020.

[30] R. Röhlsberger, H.-C. Wille, K. Schlage, and B. Sahoo, "Electromagnetically induced transparency with resonant nuclei in a cavity," *Nature*, vol. 482, no. 7384, pp. 199–203, 2012.

[31] K. P. Heeg, A. Kaldun, C. Strohm, P. Reiser, C. Ott, R. Subramanian, D. Lentrodt, J. Haber, H.-C. Wille, S. Goerttler, R. Rüffer, C. H. Keitel, R. Röhlsberger, T. Pfeifer, and J. Evers, "Spectral narrowing of x-ray pulses for precision spectroscopy with nuclear resonances," *Science*, vol. 357, no. 6349, pp. 375–378, 2017.

[32] D. Lentrodt, K. P. Heeg, C. H. Keitel, and J. Evers, "Ab initio quantum models for thin-film x-ray cavity QED," *Phys. Rev. Res.*, vol. 2, p. 023396, 2020.

[33] O. Diekmann, D. Lentrodt, and J. Evers, "Inverse design approach to x-ray quantum optics with mössbauer nuclei in thin-film cavities," *Phys. Rev. A*, vol. 105, p. 013715, 2022.

[34] A. Pálffy, C. H. Keitel, and J. Evers, "Single-photon entanglement in the keV regime via coherent control of nuclear forward scattering," *Phys. Rev. Lett.*, vol. 103, p. 017401, 2009.

[35] S. Yip, *Nuclear Radiation Interactions*. World Scientific, 2014.

[36] S. Hüfner, *Photoelectron spectroscopy*. Advanced Texts in Physics, Berlin, Germany: Springer, 3 ed., 2013.

[37] R. Rohlsberger, *Nuclear condensed matter physics with synchrotron radiation*. Springer Tracts in Modern Physics, Berlin, Germany: Springer, 2010.

[38] M. Cooper, P. Mijnarends, N. Shiotani, N. Sakai, and A. Bansil, *X-ray Compton scattering*. Oxford Series on Synchrotron Radiation, London, England: Oxford University Press, 2004.

[39] W. Sturhahn and V. Kohn, "Theoretical aspects of incoherent nuclear resonant scattering," *Hyperfine Interactions*, vol. 123, pp. 367–399, 1999.

[40] R. L. Mössbauer, "Kernresonanzfluoreszenz von gammastrahlung in Ir^{191}," *Eur. Phys. J. A*, vol. 151, no. 2, pp. 124–143, 1958.

[41] M. Mašláň, *Mössbauerova spektroskopie*. Vydavatelství Univerzity Palackého, Olomouc, 1993.

[42] Y. V. Shvyd'ko, "Nuclear resonant forward scattering of x rays: Time and space picture," *Phys. Rev. B*, vol. 59, pp. 9132–9143, 1999.

[43] A. Q. Baron, "Resonant nuclear scattering of synchrotron radiation: Detector development and specular scattering from a thin layer of ^{57}Fe,"

[44] W. Sturhahn and E. Gerdau, "Evaluation of time-differential measurements of nuclear-resonance scattering of x rays," *Phys. Rev. B*, vol. 49, pp. 9285–9294, 1994.

[45] U. van Bürck, D. P. Siddons, J. B. Hastings, U. Bergmann, and R. Hollatz, "Nuclear forward scattering of synchrotron radiation," *Phys. Rev. B*, vol. 46, pp. 6207–6211, 1992.

[46] G. M. Kalvius, F. E. Wagner, and W. Potzel, "Methodology of "less used" Mössbauer isotopes," *J. Phys. Colloques*, vol. 37, no. 6, pp. 657–671, 1976.

[47] V. Chechev and N. Kuzmenko, "Table of radionuclides," 2014. [Online], [visited on 2023-04-03], Available from `http://www.lnhb.fr/nuclides/Co-57_tables.pdf`.

[48] P. Schaaf, A. Krämer, L. Blaes, G. Wagner, F. Aubertin, and U. Gonser, "Simultaneous conversion electron, conversion X-ray and transmission Mössbauer spectroscopy," *Nucl. Instr. Meth. Phys. Res. B*, vol. 53, no. 2, pp. 184–186, 1991.

[49] J. R. Gancedo, M. Gracia, and J. F. Marco, "CEMS methodology," *Hyperfine Interact.*, vol. 66, no. 1-4, pp. 83–93, 1991.

[50] V. Procházka, P. Novák, A. Stejskal, M. Dudka, and V. Vrba, "Lamb-Mössbauer factor determination by resonant Mössbauer spectrometer," *Physics Letters A*, p. 128195, 2022.

[51] I. R. Khairulin, V. A. Antonov, Y. V. Radeonychev, and O. Kocharovskaya, "Transformation of Mössbauer γ-ray photon waveform into short pulses in dual-tone vibrating resonant absorber," *Journal of Physics B: Atomic, Molecular and Optical Physics*, vol. 51, no. 23, p. 235601, 2018.

[52] I. R. Khairulin, Y. V. Radeonychev, V. A. Antonov, and O. A. Kocharovskaya, "Optimal motion law of a resonant nuclear absorber for the formation of short pulses of Mössbauer radiation," *Radiophysics and Quantum Electronics*, 2023.

[53] A. Stejskal, "Development of the dual Mössbauer spectrometer and the adaptation for dynamic measurement," master thesis, Palacky University Olomouc, Faculty of Science, 2019. Supervisor: Mgr. Petr Novák, Ph.D.

[54] A. Stejskal, "Shape filtration of signal in radiation detection," bachelor's thesis, Palacky University Olomouc, Faculty of Science, 2017. Supervisor: Mgr. Michal Dudka.

[55] A. Stejskal, V. Procházka, M. Dudka, V. Vrba, J. Kočiščák, P. Šretrová, and P. Novák, "A dual mössbauer spectrometer for material research, coincidence experiments and nuclear quantum optics," *Measurement*, vol. 215, p. 112850, 2023.

[56] P. Novák, V. Procházka, and A. Stejskal, "Universal drive unit for detector velocity modulation in Mössbauer spectroscopy," *Nucl. Instr. Meth. Phys. Res. A*, vol. 1031, p. 166573, 2022.

[57] V. Evdokimov, M. Mashlan, D. Zak, A. Fyodorov, A. Kholmetskii, and O. Misevich, "Mini and micro transducers for Mössbauer spectroscopy," *Nucl. Instr. Meth. Phys. Res. B*, vol. 95, no. 2, p. 278–280, 1995.

[58] V. Procházka, P. Novák, V. Vrba, A. Stejskal, and M. Dudka, "Autotuning procedure for energy modulation in Mössbauer spectroscopy," *Nucl. Instr. Meth. Phys. Res. B*, vol. 483, p. 55–62, 2020.

[59] P. Novak, V. Prochazka, A. Stejskal, J. Kopp, and J. Pechousek, "Pulse length and amplitude filtration of gamma radiation detection, utilization in the ^{57}Fe Mössbauer spectroscopy," *Nucl. Instr. Meth. Phys. Res. A*, vol. 940, p. 152–155, 2019.

[60] E. Ermis and C. Celiktas, "Time resolution investigations for general purpose plastic scintillation detectors in different thicknesses," *Journal of Radioanalytical and Nuclear Chemistry*, vol. 295, p. 523–536, 2013.

[61] P. Novák, J. Pechousek, V. Procházka, J. Navařík, L. Kouřil, P. Kohout, V. Vrba, and L. Machala, "Time differential ^{57}Fe Mössbauer spectrometer with unique 4π YAP:Ce 122.06 keV gamma-photon detector," *Nucl. Instr. Meth. Phys. Res. A*, vol. 832, pp. 292–296, 2016.

[62] P. Horowitz and W. Hill, *The Art of Electronics*. USA: Cambridge University Press, 3rd ed., 2015.

[63] Z. Song, Z. Zhao, H. Yu, J. Yang, X. Zhang, T. Sui, J. Xu, S. Xie, Q. Huang, and Q. Peng, "An 8.8 ps RMS resolution time-to-digital converter implemented in a 60 nm FPGA with real-time temperature correction," *Sensors*, vol. 20, no. 8, 2020.

[64] E. Bayer and M. Traxler, "A high-resolution ($<$ 10 ps RMS) 48-channel time-to-digital converter (TDC) implemented in a field programmable gate array (FPGA)," *IEEE Transactions on Nuclear Science*, vol. 58, no. 4, pp. 1547–1552, 2011.

[65] S. Tancock, E. Arabul, and N. Dahnoun, "A review of new time-to-digital conversion techniques," *IEEE Transactions on Instrumentation and Measurement*, vol. 68, no. 10, pp. 3406–3417, 2019.

[66] G. Mazin, A. Stejskal, M. Dudka, and M. Ježek, "Non-blocking programmable delay line with minimal dead time and tens of picoseconds jitter," *Review of Scientific Instruments*, vol. 92, p. 114712, 2021.

[67] S. N. Rao Borra, A. Muthukaruppan, S. Suresh, and V. Kamakoti, "A novel approach to the placement and routing problems for field programmable gate arrays," *Applied Soft Computing*, vol. 7, no. 1, pp. 455–470, 2007.

[68] M. Korzhik, G. Tamulaitis, and A. N. Vasil'ev, *Coincidence Time Resolution Measurements with Scintillators*, pp. 227–242. Cham: Springer International Publishing, 2020.

[69] Y.-H. Chen, "Dual-mode FPGA-based triple-TDC with real-time calibration and a triple modular redundancy scheme," *Electronics*, vol. 9, no. 4, 2020.

[70] P. Kwiatkowski, "Employing FPGA DSP blocks for time-to-digital conversion," *Metrology and Measurement Systems*, vol. vol. 26, no. 4, pp. 631–643, 2019.

[71] F. Dadouche, T. Turko, W. Uhring, I. Malass, N. Dumas, and J.-P. Le, "New design-methodology of high-performance TDC on a low cost FPGA targets," *Sensors and Transducers*, vol. 193, pp. 123–134, 2015.

[72] D. Spencer, J. Cole, M. Drigert, and R. Aryaeinejad, "A high-resolution, multi-stop, time-to-digital converter for nuclear time-of-flight measurements," *Nucl. Instr. Meth. Phys. Res. A*, vol. 556, no. 1, pp. 291–295, 2006.

[73] M. Büchele, H. Fischer, F. Herrmann, K. Königsmann, C. Schill, and S. Schopferer, "The GANDALF 128-channel time-to-digital converter," *Physics Procedia*, vol. 37, pp. 1827–1834, 2012. Proceedings of the 2nd International Conference on Technology and Instrumentation in Particle Physics (TIPP 2011).

[74] Y. Sano, Y. Horii, M. Ikeno, O. Sasaki, M. Tomoto, and T. Uchida, "Subnanosecond time-to-digital converter implemented in a Kintex-7 FPGA," *Nucl. Instr. Meth. Phys. Res. A*, vol. 874, pp. 50–56, 2017.

[75] M. Mattada and H. Guhilot, "62.5 ps LSB resolution multiphase clock time to digital converter (TDC) implemented on FPGA," *Journal of King Saud University - Engineering Sciences*, 2021.

[76] C. Hervé, J. Cerrai, and T. Le Caër, "High resolution time-to-digital converter (TDC) implemented in field programmable gate array (FPGA) with compensated process voltage and temperature (PVT) variations," *Nucl. Instr. Meth. Phys. Res. A*, vol. 682, pp. 16–25, 2012.

[77] Y. Song, H. Liang, L. Zhou, J. Du, J. Ma, and Z. Yue, "Large dynamic range high resolution digital delay generator based on FPGA," in *2011 International Conference on Electronics, Communications and Control (ICECC)*, pp. 2116–2118, 2011.

[78] J. Song, Q. An, and S. Liu, "A high-resolution time-to-digital converter implemented in field-programmable-gate-arrays," *IEEE Transactions on Nuclear Science*, vol. 53, no. 1, pp. 236–241, 2006.

[79] A. Ambrosy and K. Holdik, "Piezoelectric PVDF films as ultrasonic transducers," *Journal of Physics E: Scientific Instruments*, vol. 17, no. 10, p. 856, 1984.

[80] P. Reiser, "Time domain control of X-ray quantum dynamics," master thesis, University of Heidelberg, 2014. Supervisor: Priv.-Doz. Dr. Jörg Evers.

[81] V. Rathod, "A review of acoustic impedance matching techniques for piezoelectric sensors and transducers," *Sensors*, vol. 20, p. 4051, 2020.

[82] V. T. Rathod, "A review of electric impedance matching techniques for piezoelectric sensors, actuators and transducers," *Electronics*, vol. 8, no. 2, 2019.

[83] H. Huang and D. Paramo, "Broadband electrical impedance matching for piezoelectric ultrasound transducers," *IEEE Transactions on Ultrasonics, Ferroelectrics, and Frequency Control*, vol. 58, no. 12, pp. 2699–2707, 2011.

[84] M. Garcia-Rodriguez, J. Garcia-Alvarez, Y. Yañez, M. Garcia-Hernandez, J. Salazar, A. Turo, and J. Chavez, "Low cost matching network for ultrasonic transducers," *Physics Procedia*, vol. 3, no. 1, pp. 1025–1031, 2010. International Congress on Ultrasonics, Santiago de Chile, January 2009.

[85] Texas Instruments, "THS3491 900-MHz, 500-mA high-power output current feedback amplifier," 2018. [Online], [visited on 2023-06-26], Available from https://www.ti.com/lit/ds/symlink/ths3491.pdf.

[86] A. Benjeddou, "Field-dependent nonlinear piezoelectricity: a focused review," *International Journal of Smart and Nano Materials*, vol. 9, no. 1, pp. 68–84, 2018.

[87] M. Vacula, "Characterization of piezoelectric materials and components," bachelor's thesis, Palacky University Olomouc, Faculty of Science, 2016. Supervisor: doc. RNDr. Jiří Pechoušek, Ph.D.

[88] K. Omote and H. Ohigashi, "Temperature dependence of shear piezoelectric properties of poly(vinylidene fluoride) studied by piezoelectric resonance method," *Japanese Journal of Applied Physics*, vol. 35, no. 3R, p. 1818, 1996.

[89] D. O'Connor, "The effect of line broadening of Mössbauer resonant sources and absorbers on the resonance absorption," *Nuclear Instruments and Methods*, vol. 21, pp. 318–322, 1963.

[90] S. Margulies and J. Ehrman, "Transmission and line broadening of resonance radiation incident on a resonance absorber," *Nuclear Instruments and Methods*, vol. 12, pp. 131–137, 1961.

[91] M. Mashlan, A. Kholmetskii, V. Yevdokimov, J. Pechousek, O. Verich, R. Zboril, and R. Tsonchev, "Mössbauer spectrometer with resonant detector," *Nucl. Instr. Meth. Phys. Res. B*, vol. 243, no. 1, pp. 241–246, 2006.

[92] D. A. Sarychev, N. M. Novikovskiy, V. V. Stashenko, V. V. Kitaev, D. N. Sivokon, and A. A. Spivakov, "Characteristics optimization of the resonant detector for Mössbauer spectroscopy using resonance ^{57}Fe," *IEEE Transactions on Nuclear Science*, vol. 64, no. 10, pp. 2729–2732, 2017.

[93] L. Levy, L. Mitrani, and S. Ormandjiev, "Properties of a resonance scintillation counter," *Nuclear Instruments and Methods*, vol. 31, no. 2, pp. 233–236, 1964.

[94] K. Mitrofanov, V. Gor'kov, M. Plotnikova, and S. Reiman, "Determination of the Mössbauer effect probability using resonance detectors," *Nuclear Instruments and Methods*, vol. 155, no. 3, pp. 539–542, 1978.

[95] T. J. Paulus, "Timing electronics and fast timing methods with scintillation detectors," *IEEE Transactions on Nuclear Science*, vol. 32, no. 3, pp. 1242–1249, 1985.

[96] W. POTZEL, "^{67}Zn Mössbauer spectroscopy," *Hyperfine Interactions*, vol. 71, no. 1, pp. 1515–1522, 1992.

[97] R. Shakhmuratov, F. G. Vagizov, and V. Y. Gaiduk, "Methods of coherent control of spectral and temporal properties of gamma photons and their potential applications," *Crystallography Reports*, vol. 65, pp. 409–411, 2020.

[98] I. R. Khairulin, Y. V. Radeonychev, and O. Kocharovskaya, "Slowing down x-ray photons in a vibrating recoilless resonant absorber," *Scientific Reports*, vol. 12, no. 1, 2022.

List of Symbols and Abbreviations

A_n	normalized transition amplitudes in magnetically split absorber
A_{bcg}	normalised amplitude of non-resonant background
$\tilde{A}(w)$	absorption function
a_e	measurement effect
a_n	normalised absorption amplitude
B_{hf}	hyperfine (effective) magnetic field
B_k	Fourier amplitude of k-th harmonics
C_{bcg}	countrate decay constant
c	speed of light in vacuum
d	absorber (physical) thickness
d_{eff}	absorber effective thickness
E	energy
E_0	initial energy
ΔE	Doppler energy detuning
$\mathcal{E}$	electric intensity of gamma photon field
$\mathcal{E}_0$	amplitude of electric intensity
$\tilde{\mathcal{E}}_{\mathrm{out}}(w)$	energy spectrum of scattered gamma photon field
$\mathcal{E}_m$	modulated electric intensity of gamma photon field
f	vibrations frequency
f_{LM}	Lamb-Mössbauer factor
$G(t)$	Gaussian time response function
I	spin
$I(t)$	normalized radiation intensity
$I_{exp}(t)$	radiation intensity fitted to experimental data
$I_n(t)$	experimental normalised radiation intensity
$I_{\mathrm{out}}(t)$	radiation intensity for particular t_0
$I_s(t)$	scaled radiation intensity
i	imaginary unit
J_k	Bessel function of the first kind of k-th order
K	number of harmonics in Fourier series
$L(\omega)$	normalised Lorentzian function
m	magnetic spin quantum number
N	number of counts or number of stages
P	momentum
p	amplitude modulation parameter
$\bar{\mathrm{p}}$ (-)	average value of parameter p
Δp	absorber motion maximum span
δp	parameter p difference
R	vibrations amplitude
$S_{\mathrm{tr}}(\omega_s)$	transmission integral
$S(\omega_s)$	Mössbauer spectrum
$S_k(\omega_s)$	k-th spectral component in Mössbauer spectrum
t	time
t_0	time of excited state origin
t_1	simulation time length
t_{life}	mean lifetime of excited state

$U_{piez.}$	voltage on the piezotransducer
U_d	driving voltage set on generator
ΔU_d	driving voltage maximum span
v	velocity
$z(t)$	absorber position
z_0	absorber initial position
$z'(t)$	normalised absorber motion profile

δ	shift of absorber resonance with respect to radioactive source
η	number of Mössbauer nuclei per unit volume
Γ_0	natural linewidth
Γ_a	absorption linewidth of the absorber
Γ_s	emission linewidth of the source
$\hbar$	reduced Planck constant
λ	wavelength of gamma photon
Ω	vibrations angular frequency or Ohm unit
ω	angular frequency of a photon
ω_0	angular frequency of energy transition in radioactive source
ω_a	angular frequency of nuclear transition in absorber
ω_s	angular frequency of photons emitted from the source
$\Delta\omega_{m,n}$	transitions energy differences induced by magnetic splitting
ϕ	absorber motion phase shift
ϕ_k	Fourier phase of k-th harmonics
θ	Heaviside step function
τ	evaluation delay of an asynchronous amplitude discriminator
τ_{max}	the maximum evaluation delay
τ_{min}	the minimum evaluation delay
σ_0	differential cross section of nuclear resonant interaction
σ_t	apparatus time resolution
φ_0	photon initial random phase

AAD	asynchronous amplitude discriminator
ADC	analog-to-digitial converter
ASIC	application specific integrated circuit
BL	base line
CEMS	conversion electron Mössbauer spectroscopy
CXMS	conversion X-ray Mössbauer spectroscopy
DAC	digital-to-analog converter
DAQ	data acquisition system
DNL	differential nonlienarity
FFT	fast Fourier transform
FPGA	field programmable gate array
FWHM	full width at half maximum
IGA	internal grant agency
LL	lower level
L × W × H	Length × Width × Height
LSB	least significant bit
LUT	look-up table
MCU	microcontroller unit
PC	personal computer
PLL	phase-locked loop
PMT	photomultiplier
PSD	pulse shape discriminator
PVT	process, voltage and temperature
PVDF	polyvinylidene fluoride
RAM	random access memory
RC	resistor-capacitor
TDMS	time differential Mössbauer spectroscopy
TDC	time-to-digital converter
UL	upper level
VHDL	VHSIC hardware description language
VHSIC	very high speed integrated circuit program
YAP:Ce	yttrium aluminium perovskite dopped by cerium

List of Publications

I. P. Novak, V. Prochazka, **A. Stejskal**, J. Kopp, and J. Pechousek, "Pulse length and amplitude filtration of gamma radiation detection, utilization in the 57Fe Mössbauer spectroscopy", *Nucl. Instr. Meth. Phys. Res. A*, vol. 940, pp. 152–155, 2019.

II. V. Procházka, P. Novák, V. Vrba, **A. Stejskal**, and M. Dudka, "Autotuning procedure for energy modulation in Mössbauer spectroscopy", *Nucl. Instr. Meth. Phys. Res. B*, vol. 483, pp. 55–62, 2020.

III. **A. Stejskal**, V. Procházka, P. Novák, and M. Dudka, "Mössbauer spectrometer designed for measurements of fast processes", *Nucl. Instr. Meth. Phys. Res. A*, vol. 984, p. 164597, 2020.

IV. G. Mazin, **A. Stejskal**, M. Dudka, and M. Ježek, "Non-blocking programmable delay line with minimal dead time and tens of picoseconds jitter", *Review of Scientific Instruments*, vol. 92, no. 11, p. 114712, 2021.

V. P. Novák, V. Procházka, and **A. Stejskal**, "Universal drive unit for detector velocity modulation in Mössbauer spectroscopy", *Nucl. Instr. Meth. Phys. Res. A*, vol. 1031, p. 166573, 2022.

VI. V. Procházka, P. Novák, **A. Stejskal**, M. Dudka, and V. Vrba, "Lamb-Mössbauer factor determination by resonant Mössbauer spectrometer", *Physics Letters A*, vol. 442, p. 128195, 2022.

VII. J. Kočiščák, P. Novák, **A. Stejskal**, J. Kopp, and V. Procházka, "High time and energy resolution semi-transparent scintillation detectors for application in γ optics and Mössbauer spectroscopy", *Measurement*, vol. 206, p. 112225, 2023.

VIII. **A. Stejskal**, V. Procházka, M. Dudka, V. Vrba, J. Kočiščák, P. Šretrová and P. Novák "A dual Mössbauer spectrometer for material research, coincidence experiments and nuclear quantum optics", *Measurement*, vol. 215, p. 112850, 2023.

Appendix

The script is also freely available online at GitHub repository and can be inserted and run in an online python compiler. For example, compiler Trinket, which is available at `https://trinket.io/embed/python3`, can be used.

```
### README ###
##############################################################################
# Multitone_gamma_conrol.py is the script for numerical calculation of the gamma
# radiation intensity behind the vibrating Moessbauer absorber whose motion profile
# is defined by Fourier series.
#
# The code is optimized for speed. For that reason several preparatory calculations
# appear in the code.

# Cut out the first 340 nanoseconds of the numerical simulation which contain
# numerical artefacts
#
# The script was run by Python version 3.7.4
# with the libraries versions:
# numpy             1.21.6
# matplotlib        3.5.3
##############################################################################

### Libraries ###
import numpy as np
import matplotlib.pyplot as plt


### Simulation parameteres ###
minus_t = 0.5               # [us] lower limit of the time integration over t0
time_range = 2.000          # [us] simulation time range - upper integration limit
num_of_points = 1000        # [-] number of points in time domain

vibration_freq = 10         # [MHz] fundamental vibration frequency
E_tuned = 10               # [MHz] Doppler energy modulation

p = 2.4                     # [-] vibration amplitude
harm_num = 1    # [-] number of harmonics in the Fourier series of motion profile
motion_shift = 0.0  # [us] time shift of absorber motion
motion_invertion = "yes" # inversion of motion profile "yes" = inverted, others = original

d_eff = 19.0                # [-] effective thickness
absorption_shift = 0        # [MHz] shift of the absorption function relative to the source
bhyf = 0.0                  # [T] hyperfine magnetic field


source_broadening = 1.00    # emission line broadening in multiple of natural linewidth
absorber_broadening = 1.00  # absorption line broadening in multiple of natural linewidth

### Fourier series parameteres - amplitudes and phases ###
### trapezoidal fast step [50 harmonics]
F_amps = [1.567, 0.697, 0.4, 0.267, 0.208, 0.182, 0.167, 0.151, 0.132, 0.115,
0.101, 0.092, 0.087, 0.083, 0.078, 0.073, 0.067, 0.062, 0.059, 0.057, 0.055,
0.053, 0.05, 0.048, 0.046, 0.044, 0.043, 0.042, 0.041, 0.039, 0.037, 0.036,
0.035, 0.034, 0.034, 0.033, 0.031, 0.03, 0.03, 0.029, 0.029,0.028, 0.027,
 0.026, 0.026, 0.025, 0.025, 0.024, 0.024, 0.023]
F_phases = [0.002, 0.006, 0.017, 0.03, 0.038, 0.044, 0.042, 0.046, 0.053,
 0.061, 0.079, 0.087, 0.08, 0.084, 0.09, 0.096, 0.104, 0.112, 0.118,
 0.122, 0.127, 0.131, 0.139, 0.148, 0.154, 0.161, 0.165, 0.169, 0.173,
 0.182, 0.192, 0.197, 0.203, 0.209, 0.209, 0.215, 0.229, 0.237, 0.237,
 0.245, 0.245, 0.254, 0.263, 0.273, 0.273, 0.284, 0.284, 0.295, 0.295, 0.308]

###square  [50 harmonics]
# F_amps = [2.292, 0.014, 0.764, 0.014, 0.458, 0.014, 0.327, 0.014, 0.254,
#  0.014, 0.208, 0.014, 0.176, 0.014, 0.152, 0.014, 0.134, 0.014, 0.12,
#  0.014, 0.109, 0.014, 0.099, 0.014, 0.091, 0.014, 0.084, 0.014, 0.078,
#  0.014, 0.073, 0.014, 0.068, 0.014, 0.064, 0.014, 0.061, 0.014, 0.058,
#  0.014, 0.055, 0.014, 0.052, 0.014, 0.05, 0.014, 0.047, 0.014, 0.045, 0.014]
# F_phases = [0.0, 0, 0.0, 0, 0.0, 0, 0.0, 0, 0.0, 0, 0.0, 0, 0.0, 0,
#  0.0, 0, 0.0, 0, 0.0, 0, 0.0, 0, 0.0, 0, 0.0, 0, 0.0, 0, 0.0, 0,
#  0, 0.0, 0, 0.0, 0, 0.0, 0, 0.0, 0, 0.0, 0, 0.0, 0, 0.0, 0, 0.0, 0, 0.0, 0]

###bipolar pulse [60 harmonics]
# F_amps = [1,1,1,1,1,1,1,1,1,1,1,1,1,1,1,1,1,1,1,1,1,1,1,1,1,1,1,1,1,1,1,1,
# 1,1,1,1,1,1,1,1,1,1,1,1,1,1,1,1,1,1,1,1,1,1,1,1,1,1,1,1,1,1,1,1,
# 1,1,1,1,1,1,1,1,1,1]
# F_phases = [0,0,0,0,0,0,0,0,0,0,0,0,0,0,0,0,0,0,0,0,0,0,0,0,0,0,0,0,0,0,0,0,
# 0,0,0,0,0,0,0,0,0,0,0,0,0,0,0,0,0,0,0,0,0,0,0,0,0,0,0,0,0,0,0,0,
# 0,0,0,0,0,0,0,0,0,0]

# dualtone
# F_amps = [1.9,0.9]
# F_phases = [0,0]
##############################################################################

##############################################################################
### function definitions ###
def generate_motion (t,harm_num,F_amps,F_phases,w,time_delay):
    val=0
    t = np.subtract(t,time_delay) # shift of the time axis for generation of shifted motion profile
    for i in range(1,harm_num+1):
        val += F_amps[i-1]*np.sin(w*i*t-F_phases[i-1]) # sum over all harmonics
    return val

def normalize (array):
```

```
    norm_constant = np.max(np.abs(array)) # normalize array by its maximum absolute value
    return np.multiply(array,1/norm_constant)
    # return np.multiply(array,1/norm_constant)
# generation of the to the absorber incident gamma photon field
def generate_photon_field (t,A,j_w_s_plus_gmmma_over_2,p_over_w_s,z_motion):
    return A*np.heaviside(t,1)*np.exp(-(j_w_s_plus_gmmma_over_2)*(t-p_over_w_s*z_motion))
# calculation of the absorption lines positions induced by mangetic splitting

def magnetic_splitting (bhyf,absorption_shift):
    gg = 0.18125 # gyromagnetic ration of ground state
    ge = -0.10348 # gyromagnetic ratio of excited state
    un = 7.6226077 # nuclear magneton in [MHz]

    un_bhyf = un*bhyf/2 # preparatory calculation
    # calculation of individual lines
    E1 = (-gg+3*ge)*un_bhyf+absorption_shift
    E2 = (-gg+ge)*un_bhyf+absorption_shift
    E3 = (-gg-ge)*un_bhyf+absorption_shift
    E4 = (gg+ge)*un_bhyf+absorption_shift
    E5 = (gg-ge)*un_bhyf+absorption_shift
    E6 = (gg-3*ge)*un_bhyf+absorption_shift
    lines_positions = [E1,E2,E3,E4,E5,E6] # assembling in list

    lines_amps =[3,2,1,1,2,3] # sextet lines amplitudes
    normalized_lines_amps = np.divide(lines_amps,sum(lines_amps)) # normalization of amplitudes

    return lines_positions, normalized_lines_amps

def absorption_function (f,bhyf,absorption_shift,gamma_0):
    lines_positions,lines_amplitudes = magnetic_splitting(bhyf,absorption_shift) # get the lines
        positions and amplitudes by magnetic splittin function

    # conversion into the angular frequencies: w = 2*pi*f
    lines_positions_w = np.multiply (lines_positions,2*np.pi)
    absorption_shift_w = np.multiply(absorption_shift,2*np.pi)
    gamma_0_w = np.multiply(gamma_0,2*np.pi)
    w = np.multiply(f,2*np.pi)


    j_gamma_0w_2 = j*gamma_0_w/2 # preparatory calculation

    val = 0
    for i in range(len(lines_positions)):
        val+= lines_amplitudes[i]*(j_gamma_0w_2)/(w-lines_positions_w[i]+j_gamma_0w_2)#  sum of
            complex conjugated Lorentzian, complex conjugation is necessary due to numpy FFT
            algorithm definition   complex conjugate in energy domain causes the reversal in the
            time domain

    return val
################################################################################

################################################################################
### elementary constants ###
gamma_0 = 1.126830 # [1/us] natural linewidth in [MHz] (0.097 mm/s * 11.61685)
E0 = 14413                      # resonant transition energy level [eV]
q = 1.602176*10**(-19)          # elementary charge [C]
c = 299.792458                  # speed of light in vacuum [m/us]
h = 6.62607015*10**(-34)        # Planck constant [J/s]
j = complex(0,1)                # complex unit

### preparatory calculations ###
dt = time_range/num_of_points       # [us] time axis step
gamma_source = gamma_0*source_broadening # [1/us] source linewidth
gamma_absorber = gamma_0*absorber_broadening # [1/us] absorber linewidth

dt = time_range/num_of_points           # [us] time axis step
# [rad/us] maximum angular frequency of the wave for simulation given by two times
# lower frequency than the maximum frequency range ((2*Pi)/dt)

### conversion of parameters to angular frequencies
w_0 = np.pi/(dt)
w_s = w_0 + 2*np.pi*E_tuned
vibration_w = 2*np.pi*vibration_freq
gamma_source_w = gamma_source*(2*np.pi)
gamma_absorber_w = gamma_absorber*(2*np.pi)
absorption_shift_w = absorption_shift*(2*np.pi)

w_E0 = 10**(-6)*2*np.pi*E0*q/h   # [rad/us] angular frequency of the 14.413 keV transition
wavelength = 10**(12)*(2*np.pi*c/w_E0)   # [pm] gamma photon wavelength
Amp = p*c/(w_E0)                 # [m] amplitude of vibrations

### time intensity t0 integration range
num = int((minus_t/(time_range/num_of_points)))+num_of_points # num of t0 points
t0_range = np.linspace(-minus_t,time_range,num)
################################################################################

################################################################################
### Numerical calculation start ###

### generation of the time and energy domain axis ###
time_axis = np.linspace(0,((num_of_points-1)*dt),num=(num_of_points)) # time axis generation
frequency_axis = np.fft.fftfreq(num_of_points, d=dt) # frequency axis generation

# frequency axis shift for FFT and multiplying to avoid the complex conjugate in energy domain
frequency_axis = np.multiply(np.fft.fftshift(frequency_axis),-1)
w_axis = np.multiply(frequency_axis,2*np.pi)# angular frequency axis generation

### iniciation of the gamma radiation intensity array ###
wave_intensity = np.zeros(num_of_points)
```

```
# print the vibration amplitude, wavelength and energy resoluton
print("Vibration amplitude: "+str(round(Amp*10**(12),1))+" pm")
print("Wavelength: "+str(round(wavelength,1))+" pm")
max = max(frequency_axis)
min = min(frequency_axis)
print("Energy resolution [MHz] "+str((max-min)/(len(frequency_axis)-1)))

##############################################################################
### generation of movement waveform
absorber_motion = generate_motion(time_axis,harm_num,F_amps,F_phases,vibration_w,motion_shift)
abs_motion_norm = normalize(absorber_motion)
if motion_invertion == "yes":
    # inversion of the absorber motion profile
    abs_motion_norm = np.multiply(abs_motion_norm,-1)

### generation of absorption function of absorber
absorption = absorption_function(w_axis,bhyf,absorption_shift_w,gamma_absorber_w)

### Calculate exponential values for absorption_function array
exponential_absorption = np.exp(-(d_eff/2)*absorption)

### preparatory calculations for generation of the incident photon field
prep1 = j*w_s+gamma_source_w/2
prep2=p/w_s
wave_amp = np.sqrt(gamma_source_w)

counter = 0 ### counter for watching the
##############################################################################
### Numerical integration over t0
for t0 in t0_range:

    time_axis_t0 = np.subtract(time_axis,t0) # preparatory calculation (time axis shift)

    ### generation of electric intensity wave
    incident_wave = generate_photon_field(time_axis_t0,wave_amp,prep1,prep2,abs_motion_norm)

    ##FFT transforamtion of the electric intensity from the time domain to energy domain
    incident_field_energy_domain = np.fft.fft(incident_wave)

    ### Absorption process
    energy_domain_after_absorption = incident_field_energy_domain * exponential_absorption

    ### Conversion of the energy domain by inverse FFT back to time domain ###
    wave_after_absorption = np.fft.ifft(energy_domain_after_absorption)

    ### Elctric field intensity calculation ###
    wave_intensity += np.abs(wave_after_absorption)**2 * dt

    counter+=1
    if counter%500 == 0:
        print(str(round((counter/len(t0_range))*100,0))+" % done",end='\r')

print("Calculation done")
### End of integration
##############################################################################

##############################################################################
### Display the absorber motion profile and gamma radiation intensity ###
fig = plt.figure(figsize=(8,8))
plt.subplots_adjust(left=0.10,
                    bottom=0.10,
                    right=0.70,
                    top=0.90,
                    wspace=0.0,
                    hspace=0.30)
plt1 = fig.add_subplot(2,1,1)
plt1.set_title("Absorber motion",fontsize=12)
plt1.set_xlabel("Time [ns]",fontsize=12)
plt1.set_ylabel("Amplitude [pm]",fontsize=12)
plt1.plot(time_axis*1000,np.multiply(abs_motion_norm,Amp*(10**(12))),'.-',markersize=2,
linewidth=0.5,label='z amplitude')
plt1.set_xlim(((motion_shift))*1000,((time_range)*1000))
plt1.text(1.05,0.65,
" p ='%02.1f'\n $\Delta$E [MHz] = '%02.1f'\n f [MHz] = '%02.1f\n Harm. [-] = '%02.0i'"
%(p,E_tuned,vibration_freq,harm_num),horizontalalignment='left',
verticalalignment='center', transform=plt1.transAxes)

plt2 = fig.add_subplot(2,1,2)
plt2.set_title("Gamma radiation intensity behind absorber",fontsize=12)
plt2.set_xlabel("Time [ns]",fontsize=12)
plt2.set_ylabel("Normalized intensity [-]",fontsize=12)
plt2.plot(time_axis*1000,wave_intensity,'.-',markersize=2,linewidth=0.5,label='z modul')
plt2.legend()
plt2.axhline(y=0.0, color='g', linestyle='--')
plt2.axhline(y=1, color='g', linestyle='--')
plt2.set_xlim(0,(time_range)*1000)
plt.show()
##############################################################################
###End of the script
```

Palacký University Olomouc
Faculty of Science

Summary of doctoral thesis

Coherent Control of Gamma-radiation Intensity by Vibrating Resonant Medium

Author: Mgr. Aleš Stejskal
Supervisor: doc. Mgr. Vít Procházka, Ph.D.
Study field: Applied Physics
Study form: full-time
Year: 2023

I declare that I have written this thesis by myself, using the cited sources, and that the thesis has not been submitted, in whole or in part, in any previous application for an academic degree. The text was improved by suggestions from DeepL Write, the open source generative artificial intelligence tool.

In Olomouc ....
Signature

Author: Mgr. Aleš Stejskal
Department of Experimental Physics
Faculty of Science
Palacký University Olomouc
Czech Republic

Supervisor: doc. Mgr. Vít Procházka, Ph.D.
Department of Experimental Physics
Faculty of Science
Palacký University Olomouc
Czech Republic

Opponent: doc. Mgr. Jaroslav Kohout, Dr.
Department of Low Temperature Physics
Faculty of Mathematics and Physics
Charles University in Prague
Czech Republic

Opponent: prof. RNDr. Miroslav Mašláň, CSc.
Department of Experimental Physics
Faculty of Science
Palacký University Olomouc
Czech Republic

Date and place of thesis defense:

.....

The doctoral thesis is available at the study department of Faculty of Science of Palacký University Olomouc, residing at the same address.

Abstract

This study explores the coherent control of gamma-ray intensity by the resonant recoilless interaction, the so-called Mössbauer effect, in the vibrating resonant medium. The Mössbauer effect is traditionally used to analyse material properties, but recent findings in the field of nuclear quantum optics have increased interest in this phenomenon. Inspired by the current state of the art, this work follows on previous publications that used harmonically vibrating resonant absorbers to manipulate gamma radiation in the time and energy domain, which led to the discovery of gamma pulses or acoustically induced transparency. In this work, the concept of gamma radiation intensity control by vibrating absorber is generalised to multi-tone vibrations. More harmonic frequencies are used to create diverse profiles of the absorber motion, which extends the possibilities of controlling of the gamma radiation intensity waveforms. The generation of narrow well-separated, high-intensity, single and double gamma pulses, or the newly discovered short-time acoustically induced absorption, is predicted by numerical simulations and proven experimentally. A significant part of the presented work is devoted to the description of the purpose-built experimental equipment and the methodology for measuring the frequency response function of the piezoelectric transducer vibrating at high frequencies with picometre amplitudes. At the end, the experimental imperfections and limitations of the gamma radiation intensity control by vibrating absorber are discussed, and possible applications and further improvements are suggested.

Abstrakt

Tato práce se zabývá koherentním ovládáním intenzity gama záření pomocí rezonanční bezodrazové interakce, tzv. Mössbauerova jevu, ve vibrujícím rezonančním prostředí. Mössbauerův jev se tradičně používá k analýze vlastností materiálů, ale nedávné poznatky v oblasti jaderné kvantové optiky zvýšily zájem o tento jev. Práce je inspirovaná nejnovějšími objevy a navazuje na nedávné publikace, které využívaly harmonicky vibrující rezonanční absorbátory pro manipulaci s gama zářením v časové a energetické doméně, což vedlo k objevení gama pulzů nebo akusticky indukované transparence. Koncept řízení intenzity gama záření pomocí vibrujícího absorbátoru je v této práci zobecněn na vibrace složené z více harmonických frekvencí, což umožňuje generování různorodých tvarů vibrací absorbátoru, které rozšiřují možnosti ovládání průběhů intenzity gama záření. Generování úzkých v čase oddělených jednoduchých a dvojitých gama pulzů o vysoké intenzitě nebo nově objevená krátkodobá akusticky indukovaná absorpce, jsou předpovězeny numerickými simulacemi a následně prokázány experimentálně. Podstatná část práce je věnována popisu speciálně vyvinutého experimentálního vybavení a metodice měření frekvenční odezvy piezoelektrického transduceru, který kmitá na vysokých frekvencích s pikometrovými amplitudami. V závěru práce jsou pak diskutovány experimentální nedokonalosti a omezení ovládání intenzity gama záření pomocí vibrujícího absorbátoru a jsou navrženy možné aplikace a další zlepšení.

Contents

Introduction

The aim of this work is to introduce the coherent manipulation of gamma radiation by the vibrating resonant absorber. For this purpose, the coherent resonant recoilless interaction of the gamma radiation with the nuclear energy levels, the so-called Mössbauer effect, is utilised. For many decades, the Mössbauer effect has been exploited primarily for the investigation of material properties [1–3]. Recently, however, it has again become a subject of interest in the field of nuclear quantum optics, which extends the principles of classical optics to the gamma-ray and hard X-ray regimes [4–9]. Especially the phenomena related to the gamma laser are of great interest [10,11]. Although experiments manipulating the gamma photons by harmonically vibrating absorbers, which led to the observation of comb-like structures [12,13], gamma echos [14–16] or quantum beats [17], were conducted from the 60s of the 20th century, the impact of the harmonic vibrations on the energy and time domain of the gamma photon field was explained properly recently [18–20].

Since then, the effects of a single-frequency vibrating absorber, such as acoustically induced transparency [21, 22] or gamma pulses generation [23–26], were described and the potential applications in the field of metrology [27, 28], quantum computing [25], nuclear quantum dynamics [29] etc. were proposed. Moreover, similar type of quantum optics experiments are performed not only with the radioactive source, but also with the synchrotron radiation. At these facilities, phenomena such as electromagnetically induced absorption [30] or radiation spectral narrowing [31] were observed. In addition, another theoretical works are devoted to the topics such as thin film X-ray cavities [32,33] or single photon mode quantum entanglement [34].

This work is inspired by the state of the art in the rapidly developing field of nuclear quantum optics and focuses on the particular topic of shaping gamma radiation intensity by vibrating absorber. Up to date, only the control of radiation intensity by harmonic vibrations, which provides limited possibilities, was properly described and experimentally proved. The work has two objective: the first is the investigation of the coherent gamma radiation intensity control by the multi-tone vibrating absorber, which should extend this concept in a general form. The second is the development of the experimental equipment which is necessary for performing the nuclear quantum experiments, which require investigation of the gamma photon field in both the energy and time domain.

The present thesis is divided into three main chapters. In the first chapter, the theoretical overview is provided, including the special terms and units used, and numerical calculations and predictions are made. The second chapter deals with the experimental equipment developed for the needs of the experiments. Finally, the third chapter describes the methodology and the experiments for the control of the gamma radiation intensity by the multi-tone vibrating absorber.

1 Gamma Radiation Scattering in Resonant Environment

Scattering of gamma radiation in the matter consisting of nuclei and electrons covers several fundamental processes such as the photoelectric effect, Compton scattering, nuclear resonant scattering, etc., which are exploited for various gamma-ray and X-ray spectroscopy techniques [35–38]. These interactions can basically be classified as either resonant or non-resonant, incoherent or coherent, elastic or inelastic [35,39]. In the present work we, are only interested in the coherent elastic resonant nuclear scattering, i.e. the so-called Mössbauer effect discovered in 1958 by Rudolf Mössbauer [40]. The other interactions are unwanted and lead to noise detections that contribute to the non-resonant background in the Mössbauer experiments. Mössbauer spectroscopy is utilised for investigation of material properties ,however it is not of interest in present work, because we exploit here the Mössbauer effect and the relevant equipment primarily for coherent manipulation with the gamma photons.

1.1 Resonant Scattering in Harmonically Vibrating Absorber

Let's assume a single line absorber that, unlike the standard Mössbauer spectroscopy experiment, vibrates harmonically, so that its position in time can be written as

$$z(t) = z_0 + R\sin\left(2\pi f t + \phi\right) , \tag{1}$$

where z_0 is the initial position, and R, f and ϕ describe the amplitude, frequency and phase of the vibrations respectively. For the further description, we define also the angular frequency of the vibrations $\Omega = 2\pi f$ and take into consideration that the vibration frequency is comparable to the reciprocal value of the decay lifetime (6.75 MHz for ^{57}Fe) and the amplitude is comparable to the gamma photon wavelength (86 pm for 14.41 keV). The impact of the absorber vibrations on gamma radiation scattering was comprehensively explained recently in the reference [20], despite the fact that the first experiments were conducted several decades earlier [12,13,17]. It was explained that the uniformly vibrating single line absorber sees the incident photon field like a structure of multiple absorption lines (spectral components) which are equidistantly spaced by the frequency Ω.

The modulation of the spectral components in the energy domain by the absorber vibrations has interesting consequences also in the time domain. In the paper [20], it is further explained that tuning the energy of the radioactive source to the first peak (sideband) leads to the generation of periodic gamma pulse intensity structure whose period is given by frequency of the vibrations and whose intensity exceeds the incident radiation level. The harmonically vibrating absorber can also be utilised also for the generation of double and triple pulse bunches by tuning the gamma photons energy to the second and the third sideband respectively [24–26]. However, the temporal properties of the gamma pulses in this concept can be modified only to a limited extent by changing the absorber characteristics, incident photon energy or frequency and amplitude of the vibrations. Specifically, the single vibration frequency cannot generate pulses narrower than about $1/(4f)$ [25], which determines the lowest positive duty cycle of about 25 %. Thus, the absolute pulse width can be reduced only if the repetition frequency f is increased. Furthermore, the intensity of the pulses reaches its maximum at certain vibrations amplitudes, e.g. the most intense single pulses are

obtained for $R = 24.6\,\mathrm{pm}$, [20], and the shape of the pulses at the maximum intensity can be modified only in a limited way by absorber characteristics and energy detuning.

We would like to point out that, with respect to the theoretical description of the interference phenomena induced by the vibrating absorber and the notation used in this field, it is more natural to express the energy in megahertz units and the amplitude of the vibrations by the dimensionless parameter p. The conversion relations between the mentioned units are the following: $1\,\mathrm{mm/s} = 11.615\,\mathrm{MHz}$ and $p = 1.0 = 13.694\,\mathrm{pm}$ ($\lambda = 86\,\mathrm{pm}$).

1.2 Resonant Scattering in Multi-Tone Vibrating Absorber

One of the goals of the nuclear quantum optics is the generation of the narrow high-intensity pulses whose temporal properties could be easily controlled. For this reason, the improvement of the concept of the harmonically vibrating absorber is of interest. A recent theoretical work [41] predicts that the narrower gamma pulses of higher intensity can be obtained if the second harmonic frequency of appropriate amplitude and phase is added to the vibrational motion of the absorber. The additional intensity enhancement is explained by the synchronization of more spectral components which appear in the spectrum owing to the second harmonic. From another point of view, the interference result is influenced by adding the second frequency because it changes the absorber motion profile, which results in a different phase shift modulation of the scattered wave in time.

In the present work, we develop the idea of adding more harmonics, which allows the creation of more complicated periodical motion of the absorber. Taking into account the infinite series of harmonics, we get the Fourier series, which offers the possibility of assembling any arbitrary but still periodic motion profile, whose period is determined by the fundamental frequency. Each harmonic frequency in the absorber motion introduces two variables (amplitude and phase) that influence the temporal properties of the gamma pulses. The question is, what are the optimal amplitudes and phases of these harmonics – in other words – what is the optimal absorber motion profile for generating the high-intensity narrow pulses? The clue can be partially found in the publications regarding the study of the gamma echoes [14,16,18,23] and in the work describing the spectral narrowing of synchrotron radiation [9].

Since the analytical description of the scattering in the multi-tone vibrating absorber was difficult to handle, we decided to solve it numerically. The calculation procedure of the gamma radiation intensity is described later in Subsection 1.2.1. Analysis of the numerical results proved that the step-like motion creates intensive single gamma pulses. Moreover, observation of the various simulations revealed that the concept of the multi-tone vibrating absorber can be further generalised to arbitrary control of the gamma radiation. It means that there can exist various motion profiles that create not only the single gamma pulses, but also the arbitrary structures containing the enhanced pulses and absorptions of different widths and amplitudes as well. Since the palette of possible motion profiles is too broad and searching for the optimal ones would deserve a thorough analysis, we have focused only on the basic profiles such as triangle, square, trapezoid and bipolar pulse in this work. The application of these motion profiles to gamma radiation intensity control and discussion of the corresponding results of the numerical simulations are presented in Subsection 1.2.2.

1.2.1 Numerical Calculations

For the numerical calculation of the gamma radiation intensity behind the multi-tone vibrating absorber, we assume the absorber motion in time $z(t)$ in the form

$$z(t) = z_0 + Rz'(t) = z_0 + R\sum_{k=1}^{K} B_k \sin\left(2\pi k f t + \phi_k\right) , \tag{2}$$

where z_0 is the absorber initial position, R defines the amplitude of the absorber maximum displacement and $z'(t)$ is the normalised shape of the absorber motion profile ($\max|z'(t)| = 1$), which is defined by the sum of the Fourier series. In it, K defines the number of harmonics, f is the fundamental frequency of the motion, B_k are the normalised amplitudes and ϕ_k are the phases of the k-th harmonic.

The gamma photon originating from the deexcitation of the first excited state is in the distance z from the radioactive source described as a quasi-monochromatic electromagnetic wave with electric intensity

$$\mathcal{E}(t) = \mathcal{E}_0\,\theta\left(t - t_0 - \frac{z}{c}\right) \times \exp\left[-\left(i\omega_0 + \frac{\Gamma_0}{2}\right)\left(t - t_0 - \frac{z}{c}\right) + i\varphi_0\right] , \tag{3}$$

where $\mathcal{E}_0$ is the normalisation constant whose value is equal to $\sqrt{\Gamma_0}$, θ is the Heaviside step function with argument $t - t_0 - \frac{z}{c}$ which describes the emission of the photon after time t_0 from the excited state origin, the fraction $\frac{z}{c}$ describes the time delay caused by the propagation of the photon through space, ω_0 is the transition energy in the radioactive source, φ_0 is an initial random phase and i is the imaginary unit. Note that the phase φ_0 can be neglected in the further description, because it plays role only in the multiple photon interference. In the case of nuclear resonant scattering, the single photons dominantly interfere in the scattering process and the result is independent of the initial phase of the incident photon.

Let's consider now that the gamma photon propagates towards the vibrating absorber and its energy is Doppler-modulated by the constant velocity motion of the source. The total relative movement of the source from the absorber view can be written as

$$z(t) = -z_0 + vt - Rz'(t) , \tag{4}$$

where v is the constant velocity of the source. Then the absorber sees the frequency modulated electric intensity $\mathcal{E}_m(t)$ in the form

$$\begin{aligned} \mathcal{E}_m(t) = \mathcal{E}_0\,\theta&\left(t - t_0 - \frac{z_0}{c} + \frac{vt}{c} - \frac{Rz'(t)}{c}\right) \\ \times \exp&\left[-\left(i\omega_0 + \frac{\Gamma_0}{2}\right)\left(t - t_0 - \frac{z_0}{c} + \frac{vt}{c} - \frac{Rz'(t)}{c}\right)\right] . \end{aligned} \tag{5}$$

In this equation, we can neglect the expression z_0/c, since it causes an irrelevant constant time delay and the corresponding phase shift. In the same way, any disturbing mechanical vibrations can be neglected due to their low frequency (in comparison with absorber vibrations) even though, in practice, they can change the distance z_0 by several micrometres. In the argument of the Heaviside function, all parameters except t_0 can be neglected because their effect is eleven and more orders of magnitude lower.

In the exponential, the expression vt/c can be recognised as the constant velocity Doppler energy modulation $\Delta E = \frac{v}{c}\omega_0$ provided by the transducer. Since the term $\Gamma_0/2$ is thirteen orders of magnitude lower than ω_0, the multiplication with the exponential decay can be neglected and the exponent can be simplified by merging the energy modulation with ω_0 into $\omega_s = \omega_0 + \Delta E$. Next, the expression $Rz'(t)/c$ describes the effect of the high-frequency multi-tone vibrations, which basically also perform the Doppler energy modulation, but five orders of magnitude faster than the transducer. In order to replace the maximum vibration displacement R by the parameter p, the expression can be rewritten using the emitted photon energy ω_s as follows

$$\frac{R}{c} z'(t) = \frac{p}{w_s} z'(t)\,. \tag{6}$$

Taking into account the above mentioned adjustments, the modulated electric intensity can be expressed in the form

$$\mathcal{E}_m(t) = \mathcal{E}_0\,\theta\,(t - t_0) \times \exp\left[-\left(i\omega_s + \frac{\Gamma_0}{2} \right) \left(t - t_0 - \frac{pz'(t)}{\omega_s} \right) \right]. \tag{7}$$

Note here that from the absorber reference frame, the situation when the electric intensity is modulated by the motion of either the absorber or the radioactive source is equivalent, because the relative motion between the source and the absorber is important. Thus, the high frequency modulation can be performed also by the radioactive source. However, in the laboratory reference frame it has to be ensured that the source moves in the opposite direction than the absorber in order to induce the same effects.

The photon field $\mathcal{E}_m(t)$ interacts with the absorber, which is described in the energy domain by the absorption function $\tilde{A}(w)$. Unlike the transmission integral, in the numerical calculations, this function has to be expressed in the complex form in order to capture the imaginary part. The complex single Lorentzian absorber is described as follows

$$\tilde{A}(w) = \frac{i\frac{\Gamma_0}{2}}{(\omega - \omega_0 - \delta) + i\frac{\Gamma_0}{2}}\,, \tag{8}$$

where δ is the shift of the centre of the absorption function with respect to the source emission line. For the needs of the experiments, we consider a more complicated model of magnetically split absorber, whose absorption function is given by the sum of the six lines

$$\tilde{A}(w) = \sum_{n=1}^{6} A_n \frac{i\frac{\Gamma_0}{2}}{(\omega - \omega_0 - \delta - \Delta\omega_{m,n}) + i\frac{\Gamma_0}{2}}\,, \tag{9}$$

where $A_n = \frac{3}{12}, \frac{2}{12}, \frac{1}{12}, \frac{1}{12}, \frac{2}{12}, \frac{3}{12}$ for $n = 1, \ldots, 6$ are the normalised amplitudes of the sextet lines and the term $\omega_0 - \delta - \Delta\omega_{m,n}$ defines their energies. The expression $\Delta\omega_{m,n}$ depends on the hyperfine magnetic field B_{hf} and determines the energy shifts induced by magnetic interaction. The calculation of $\Delta\omega_{m,n}$ values can be found in Appendix (function "magnetic_splitting") or can be derived from the literature [2, 37] by subtracting the corresponding excited and ground state energy levels.

The procedure of the numerical calculation of the output intensity is similar to the analytical derivation of the transmission integral. The electric intensity $\mathcal{E}_m(t)$ of the incident photon field is transformed into the energy domain by the fast Fourier transform (FFT). Subsequently, the scattering process is performed by multiplying the

energy domain of the photon field $\tilde{\mathcal{E}}_m(\omega)$ and the absorption function $\tilde{A}(w)$ according to the equation

$$\tilde{\mathcal{E}}_{\mathrm{out}}(w) = \tilde{\mathcal{E}}_m(\omega) \times \exp\left(-\frac{d_{\mathrm{eff}}}{2}\tilde{A}(w)\right) , \tag{10}$$

where the effective thickness of the absorber plays an important role. The scattered output wave $\tilde{E}_{out}(w)$ is subsequently transformed back into the time domain by inverse FFT. The experimentally measurable radiation intensity $I_{\mathrm{out}}(t)$ is then obtained as a modulus of the output electric intensity $\mathcal{E}_{out}(t)$ using the complex conjugate

$$I_{\mathrm{out}}(t) = E_{\mathrm{out}}(t)E^*_{\mathrm{out}}(t) =\mid E_{\mathrm{out}}(t) \mid^2 . \tag{11}$$

However, this is not the end because the calculation was performed for a specific value of t_0. Since we are interested in the radiation intensity measured with respect to the absorber motion profile, the random nature of the radioactive decay has to be considered. Deexcitation at time t_0 after the excited state origin has an exponential distribution, but the excited state originates at random times, so the resultant distribution of the parameter t_0 is uniform, corresponding to the random process. For this reason, the resultant experimentally observable gamma radiation intensity, which we label the normalised radiation intensity $I(t)$, is given by integral

$$I(t) = \int_{-\infty}^{\infty} I_{\mathrm{out}}(t, t_0)\, dt_0 . \tag{12}$$

The linewidth of the emission Γ_s and absorption Γ_a line is intentionally listed separately because the natural linewidth Γ_0 is not always used. For experimental data fitting, when the precise parameters of the absorber or especially the source are unknown, the linewidths may be slightly increased to describe the line broadening [21]. For example, $\Gamma_s = 1.2\Gamma_0$ is considered in our experiments and the same approach can be used also for the absorber linewidth.

Since only a single line absorber is used in this work, it is advantageous to relate the Doppler energy modulation ΔE to the spectrum shift δ. In this way, both parameters can be merged in ΔE, which hereafter has the meaning of the energy detuning from the resonance. This step helps to simplify the description of the energy detuning of gamma photons in simulations and experiments.

The calculation procedure was implemented in Python and the optimised script to simulate the normalized intensity waveforms $I(t)$ is available with comments in Appendix. Since the numerical simulation works with a finite time resolution in units or tenths of nanoseconds, the real angular frequency $w_s = 3.49 \times 10^{18}$ rad/s is too high to be used due to the sampling theorem. The maximum numerical angular frequency range $\Delta\omega$ of the simulation is determined by the time resolution dt according to the relation $\Delta\omega = 2\pi/dt$ which gives a maximum angular frequency range 3.14×10^9 rad/s (500 MHz) for 2 ns time resolution. For that reason, the lower angular frequency w_s, specifically the value equal to half of $\Delta\omega$, i.e $w_s = \pi/dt$, which fulfils the condition of the sampling theorem, is used in the calculation.

Another numerical aspect is the determination of the finite integration limits for t_0. It was experimentally verified that the sufficient integration interval is from -0.5 μs to the required time length of the simulation, i.e. for the time length $\langle 0, t_1\rangle$ the t_0 should be integrated at least in the range $\langle -0.5, t_1\rangle$. Going further into the past does not improve the simulation results. Nevertheless, some numerical artefacts still occur in the first approximately 350 ns. We were unable to identify the cause of these artefacts, so we simply cut this region out when fitting the experimental data.

1.2.2 Simulations

In this subsection, we demonstrate the potential of the multi-tone vibrating absorber to control the temporal properties of the gamma radiation intensity by four different velocity profiles: triangle, trapezoid, square and bipolar pulse, see Figures 1,2,3,4,5. For the simulations shown here, we take into account the single line absorber ($B_{\mathrm{hf}} = 0$), the radioactive source with $\Gamma_s = \Gamma_a = \Gamma_0$ and the effective thickness of the absorber $d_{\mathrm{eff}} = 10$ (equivalent of about $30\,\mu$m thick stainless steel foil). The energy detuning ΔE and the parameters influencing the absorber motion profile, i.e. p and K, are varied. The fundamental frequency f, which controls the period of the radiation intensity pattern, is chosen at either 1 MHz or 2 MHz. For practical reasons, we further describe the motion amplitude by the maximum span of the absorber position $\Delta p = \max[z(t)] - \min[z(t)]$ when $\Delta p = 2p$ applies for all profiles symmetrical along the time axis.

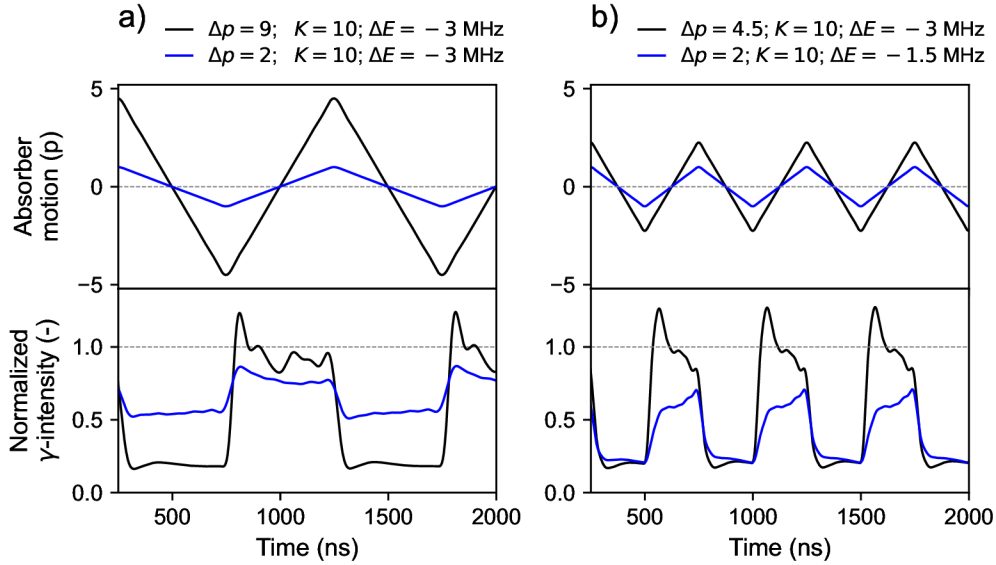

Figure 1: *Radiation intensity waveforms controlled by a triangular motion profile with fundamental frequency 1 MHz, part a), and 2 MHz, part b). The highest deviations from the two constant levels occur when the Doppler modulation rapidly changes when the absorber turns the direction of its motion.*

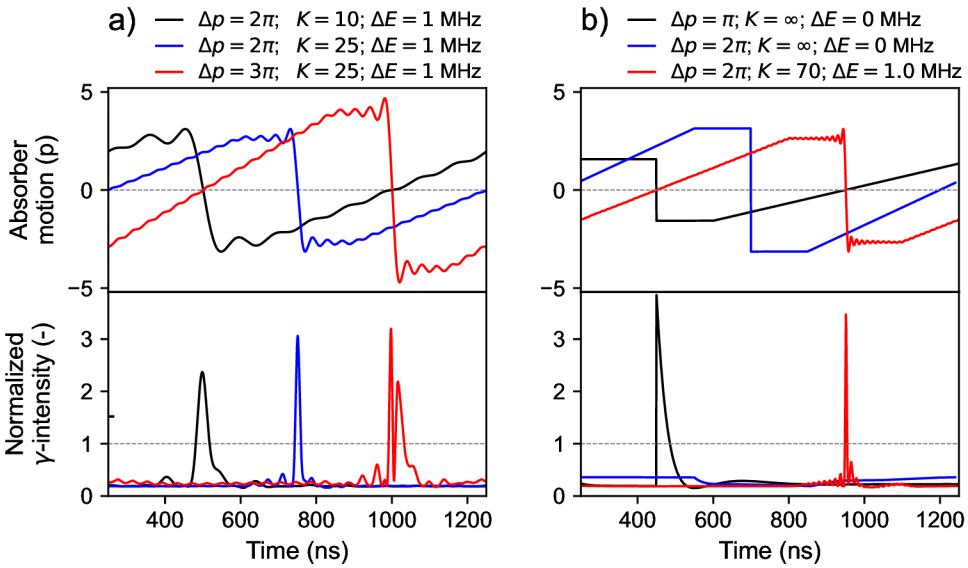

Figure 2: *Radiation intensity waveforms controlled by a trapezoidal motion profile with a fundamental frequency 1 MHz. The influence of the number of harmonics and vibrations amplitude on the pulse shape generated by finite jump is demonstrated in part a) and comparison of finite and infinite step jump ($K = \infty$) is shown in part b).*

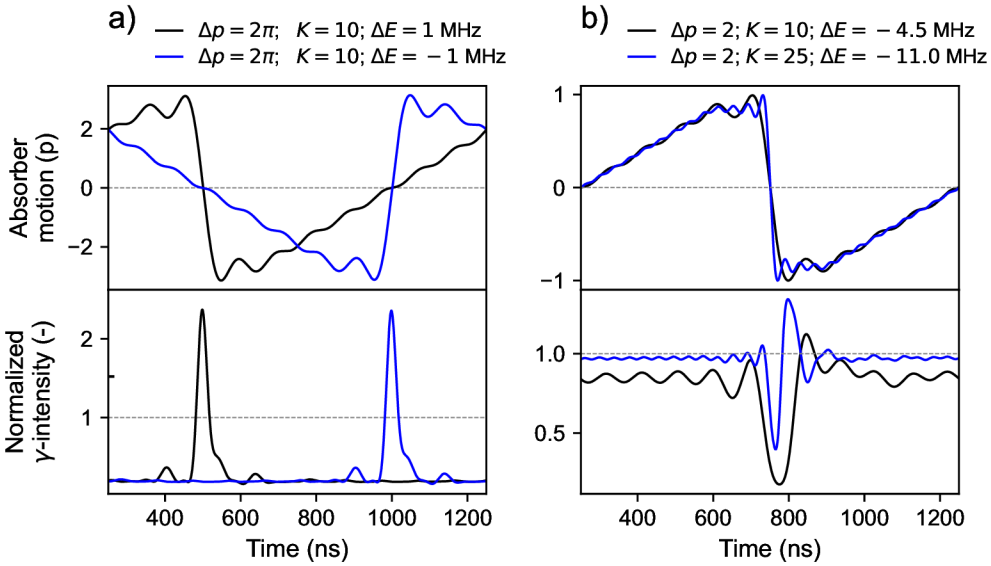

Figure 3: *Symmetry of energy detuning and absorber motion direction, part a) and short time acoustically induces absorption, part b).*

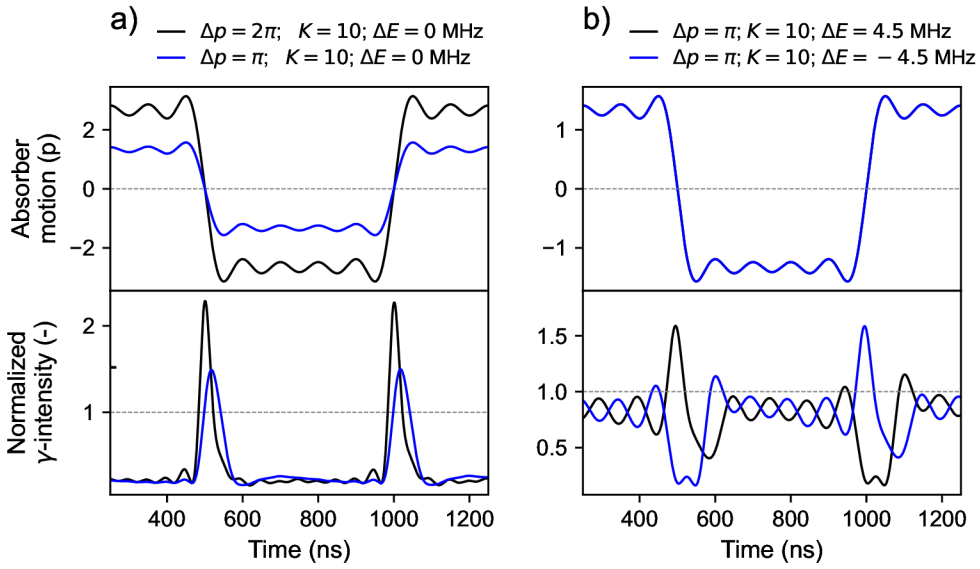

Figure 4: *Radiation intensity control by a square motion profile. Both, rising and falling edges of the profile allow easily double the frequency of the pulses, part a), but when detuned out of the resonance, one edge creates pulses and another induces the absorption, part b).*

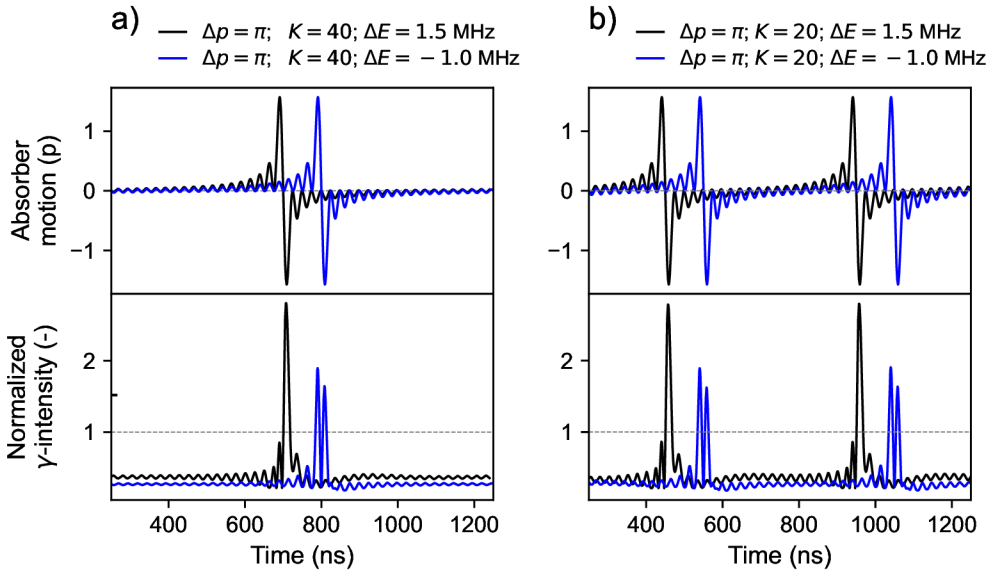

Figure 5: *Generation of single or double gamma pulses by a bipolar pulse shaped motion profile with a fundamental frequency 1 MHz, part a), and 2 MHz, part b).*

The presented simulations show that the multi-tone vibrations allow to control the temporal properties of the gamma radiation in a broader way than a simple frequency vibrations. The period of the pulses can be tuned while maintaining their width, which can be adjusted by the low-to-high time of the absorber jump. The output intensity can exceed up to three times the incident intensity and the pulse width can be narrowed to a few nanoseconds. Moreover, the intensity waveforms may be shaped in various ways by changing the energy detuning and the absorber motion profile.

2 Experimental Equipment

The nuclear quantum experiments described in the previous chapter require specific equipment. In addition to the sufficiently fast piezotransducers to vibrate the absorber at high frequencies, a DAQ system combining the functionality of the Mössbauer spectrometer and a time-tag is necessary. As the area of nuclear quantum optics is relatively new, it is not possible to purchase specialised equipment for this purpose. One possibility is to assemble the DAQ system from many general-purpose modules (e.g. from Ortec) [18, 20, 25]. However, assembling and setting up such a system is time-consuming and changing its functionality is complicated. Therefore, we have developed our own system based on the Mössbauer spectrometer that has been developed at our department in recent years [42, 43]. Specifically, the firmware and software of the spectrometer has been upgraded in order to develop a compact, purpose-built DAQ system for nuclear quantum experiments in general, which provides data processed on the hardware level.

2.1 Mössbauer Spectrometer for Nuclear Quantum Experiments

The aforementioned upgraded Mössbauer spectrometer as a whole is properly described in the author's paper [44]. The scope of this section is only the description of the spectrometer improvements regarding the signal processing for the time measurements, because the fully-fledged Mössbauer spectrometer was developed as a part of the author's previous theses [42, 43].

For nuclear quantum experiments, it is essential to analyse the gamma radiation not only in the energy domain, but mainly in the time domain. For this reason, an upgrade of the spectrometer, which diagram is in Figure 6, involved the implementation of the time-to-digital converter (TDC), asynchronous amplitude discriminator (AAD) and asynchronous delay lines. These components are necessary to perform the required time-of-flight measurements on two separated inputs between the pulses having the demanded amplitude. To avoid the hardware modifications, the required components (entities) were implemented on the level of the FPGA firmware. The diagram of the signal processing in the FPGA with upgrade highlighted is shown in Figure 7.

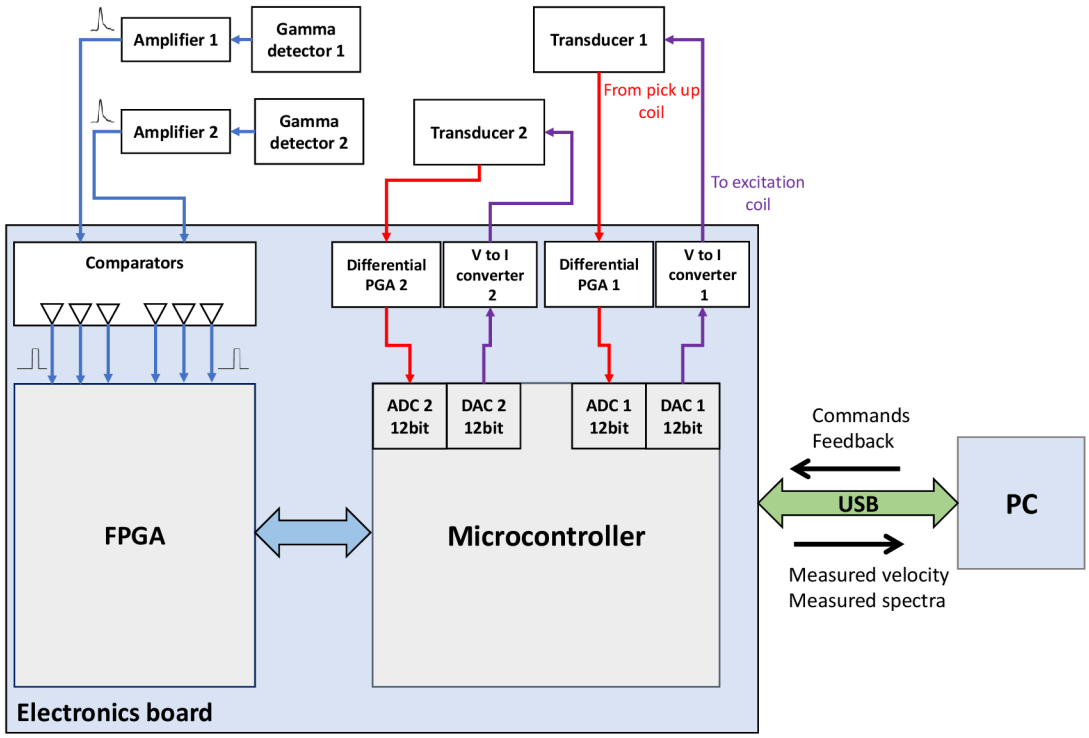

Figure 6: *Diagram of the dual Mössbauer spectrometer. Abbreviations: ADC – analog-to-digital converter, DAC – digital-to-analog converter, PGA – programmable gain amplifier.*

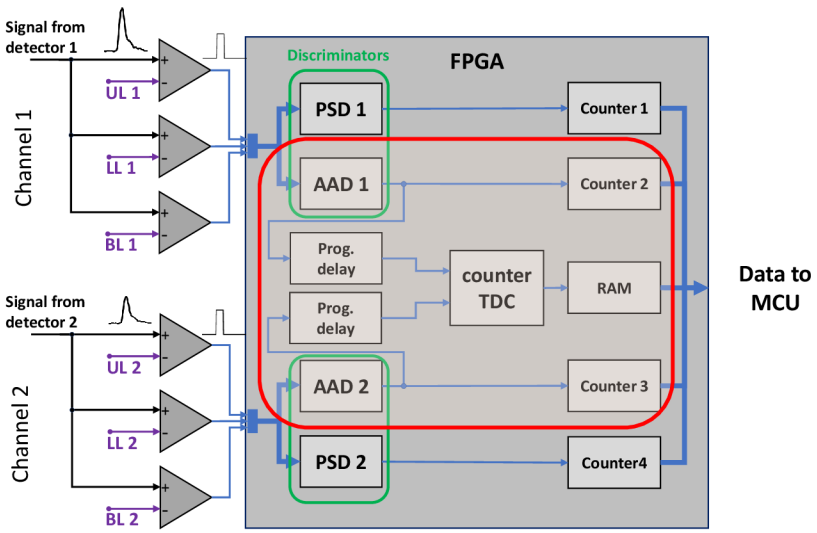

Figure 7: *Diagram of the signal processing in the FPGA. Red line encircles the newly developed parts for the nuclear quantum experiments. Abbreviations: PSD – pulse shape discriminator, AAD – asynchronous amplitude discriminator, TDC – time-to-digital converter.*

2.2 Piezotransducer

Gamma radiation intensity control requires a high-frequency motion of the resonant absorber at amplitude levels comparable to the gamma photon wavelength. Piezoelements are the best way to achieve the well-controlled low amplitude motion, even on the scale of picometres. Specifically, the beta phase of the organic polymer polyvinylidene fluoride (β-PVDF) exhibits suitable piezoelectric properties such as a sufficient electromechanical coupling and high frequency response [45] for this purpose. Unlike other piezoelectric materials, such as quartz or piezoceramics, the PVDF can be easily formed into thin foils (tens of μs) which exhibit negligible gamma radiation absorption. This makes the PVDF a suitable piezomaterial for the realization of the low-amplitude motion in gamma optical experiments. As the high-frequency positioning of the Mössbauer absorber at a picometre scale is a specific task, no suitable transducer or actuator was found on the market. For this reason, the purpose-built piezotransducer was developed, see Figure 8.

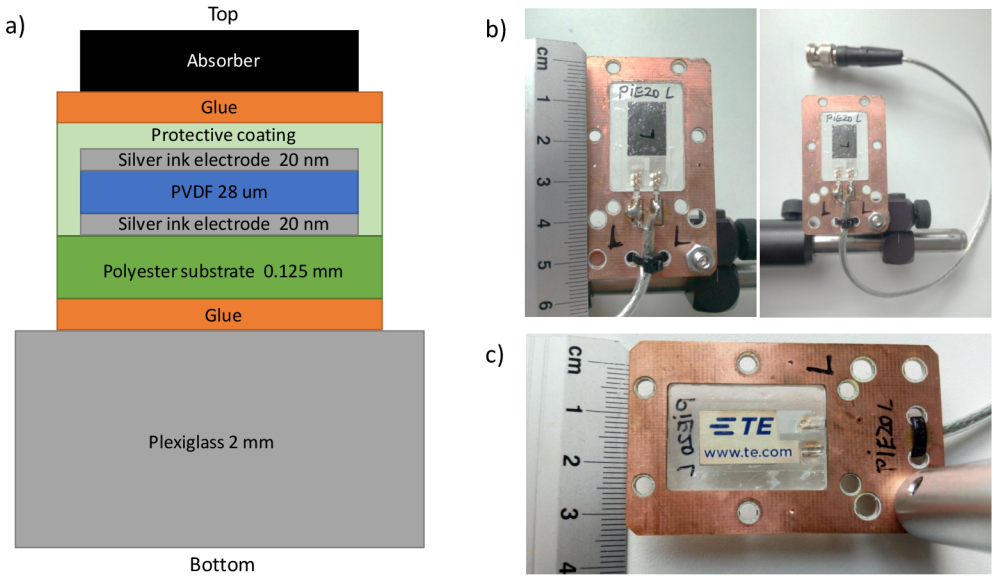

Figure 8: *A cross section, part a), and the photos of the created PVDF piezotransducer from the top, part b), and the bottom side, part c). Plexiglass is surrounded by a holder milled from the cuprextit which serves for the cable mounting.*

2.3 Piezotransducer Driver

Driving the developed piezotransducers at high frequencies (1–50 MHz) was problematic due to their low impedance at high frequencies and the associated difficulties in providing sufficient power. In addition, the driver needed to be small enough to be placed close to the transducer, minimising the radiated electromagnetic field. For this reason, a special high-frequency piezodriver with small dimensions and low output impedance was developed, see its schematic and photo in Figures 9 and 10 respectively.

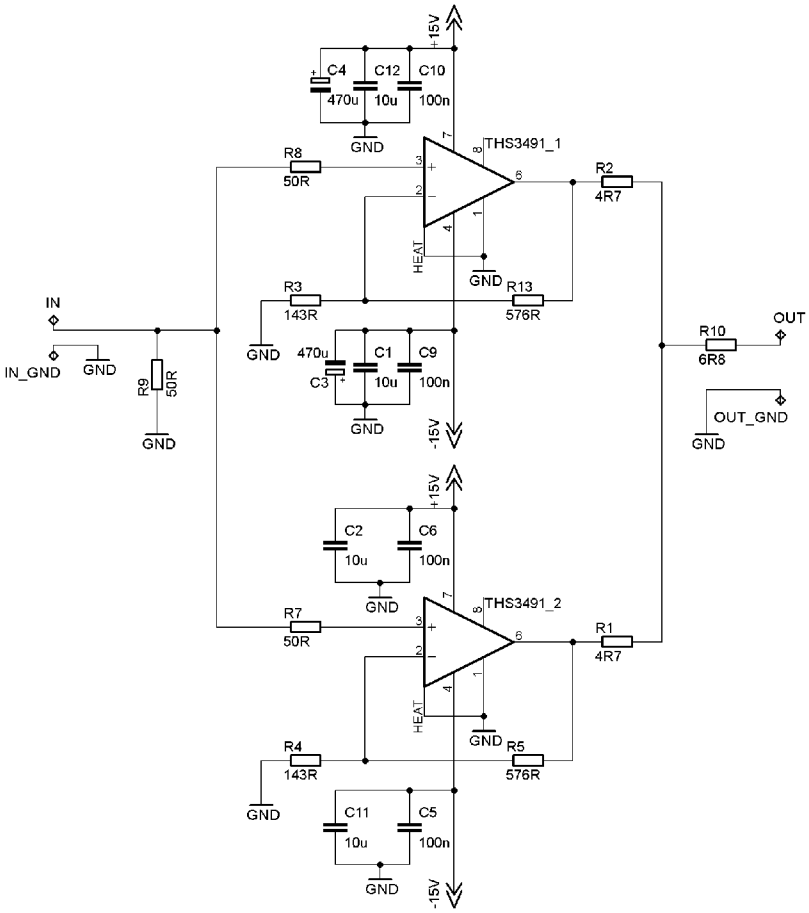

Figure 9: *Schematic of the piezodriver based on the operational amplifier THS3491.*

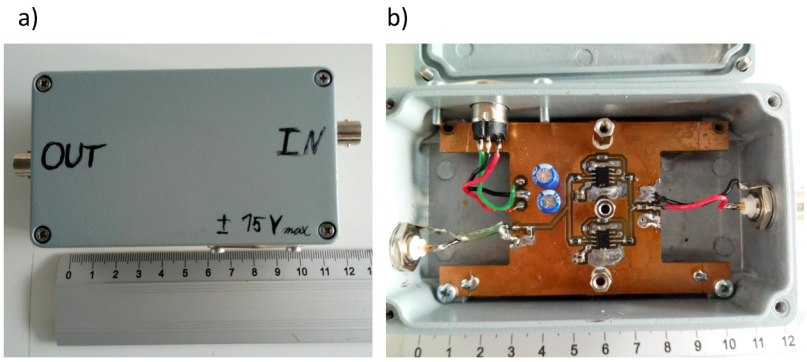

Figure 10: *Developed piezodriver: outside view, part a), and inside view, part b).*

3 Gamma Radiation Intensity Control

This chapter contains the complete description of the experimental work concerning the coherent control of the gamma radiation intensity by the vibrating Mössbauer absorber, which was presented in Chapter 1. First, the experimental setup and the type of measurements are described in detail. Subsequently, a methodology for determining the frequency response of the piezotransducer system is explained. Specifically, the dependence of the amplitude and the phase of the Mössbauer absorber vibrations on the driving voltage are the subject of interest because it is crucial for realization of more complex absorber motion profiles composed of more than one harmonics. Related to that, one section is devoted to the fitting of the measured time histograms. Since the numerical calculations rely on few parameters, which are undesirably correlated, it was necessary to fix some of them in order to get a correct results.

3.1 Experimental setup

Experimental investigation of the gamma radiation intensity control by the multitone vibrating absorber requires measuring the time-of-flight histograms of the 14 keV gamma photons which energy is tuned to the certain level. The time-of-flight is measured between the starting pulse synchronized with the high-frequency motion of the Mössbauer absorber and the detection of the 14 keV photon. The diagram of experimental setup, which utilizes components described in Chapter 2, i.e. the spectrometer, piezodriver and piezotransducer, is shown in Figure 11.

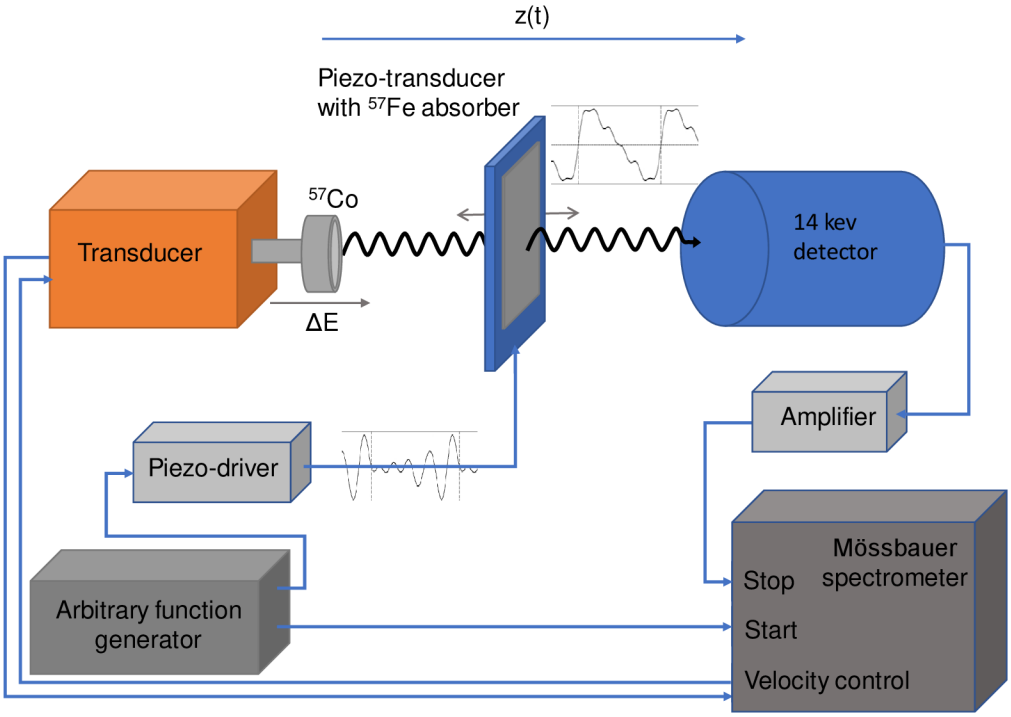

Figure 11: *Experimental setup for measurement of the gamma radiation intensity controlled by a vibrating absorber.*

3.2 Piezotransducer Frequency Response Measurement

It is already known that the Mössbauer absorber glued to the PVDF piezofoil moves harmonically when driven by harmonic voltage [25–28]. However, if more complicated motion profiles are required, they are difficult to be achieved if the system is not linear, i.e. the principle of superposition does not hold true. In general, the piezoelectric materials are non-linear. Their electromechanical frequency response depends on the shape of the piezoelement, its microstructure, mounting, intensity of applied electric field, its temperature etc. [46–48]. The excitation by sinusoidal voltage does not have to result in sinusoidal motion of the piezosurface. However, for some materials and under certain conditions, e.g. low excitation voltage, the non-linearities are so small that the system can be approximated as linear. Since the complex analysis of the properties of our piezotransducer would be demanding, it was simply assumed that it could be a linear system. Under this assumption, the relation between the driving voltage and the real motion of the absorber can be described by a complex frequency response function where the real part defines the relation of the amplitudes and the imaginary part determines the differences of the phase shifts.

One way, how to get the required response function, is to know the frequency response of individual parts, i.e. piezodriver, piezotransducer including the cable, electromechanical coupling of the piezofoil and mechanical coupling between the piezofoil and the absorber. However, obtaining all of them would be too complicated. Since they are assumed to be linear systems, the response function of the entire system can be measured directly between the on generator set driving voltage (hereinafter only driving voltage) and the motion of the absorber.

The driving voltage is under our control so it remains to measure the real motion of the Mössbauer absorber which vibrates, however, on the level of units, maximally tens of picometres. Fortunately, the most natural way to measure such a low amplitude is to use the interference effects which are caused by the motion itself. Such a method for determining the amplitude of the high-frequency harmonic motion has already been published [27, 28] and an outstanding spacial resolution in units of picometres was achieved. It was based on the measuring of the comb structure in the Mössbauer spectrum. However, this method was unsuitable in our case, because it does not provide the information about the phase shift. For this reason, it is necessary to measure the time structure of the photon field, because it allows to obtain not only the information about the amplitude response, but also the phase of the absorber motion relative to the phase of the driving voltage. In addition, the time domain measurement is much more sensitive. Especially low amplitudes vibrations, which are hardly distinguishable in the energy domain, are well visible in the time domain in the form of oscillations.

In general, the entire frequency response function can be acquired within one single measurement if the spectral-broad input signal, e.g. the step function, excites the system. Response coefficients for individual frequencies are then obtained by the comparison of the input and output Fourier spectrum. However, in our case, when the linearity of the system was only supposed, the results of such a complex measurement would be unreliable and data fitting would be much more complicated because of higher amount of parameters. For that reason, the response function was measured point by point for single frequencies. Since the preliminary measurements in the time domain showed that the dependence of the vibration amplitude and phase on the driving voltage is not linear, the response function was acquired also for different

values of the driving voltage. The only disadvantage of this approach is that the numerous time consuming measurements have to be conducted.

Resultant frequency response of the entire system, i.e. between the driving voltage and absorber motion, is shown in Figure 12 in parts a) and b). One can see miscellaneous trends in the amplitude and phase response, whose explanation is far beyond the scope of the present thesis. Dependence of the response function merely on the frequency for constant driving voltage 1 V_{pp} is shown in Figure 12 in parts c) and d). The maximum amplitude response was observed for 1 MHz and local maxima for 6 MHz and 10 MHz. On the other hand, the lowest amplitude response was for 4 MHz and local minima for 7 MHz. A huge step in the phase characteristics for 9 MHz is caused by displaying the values in interval $\langle 0, 2\pi \rangle$.

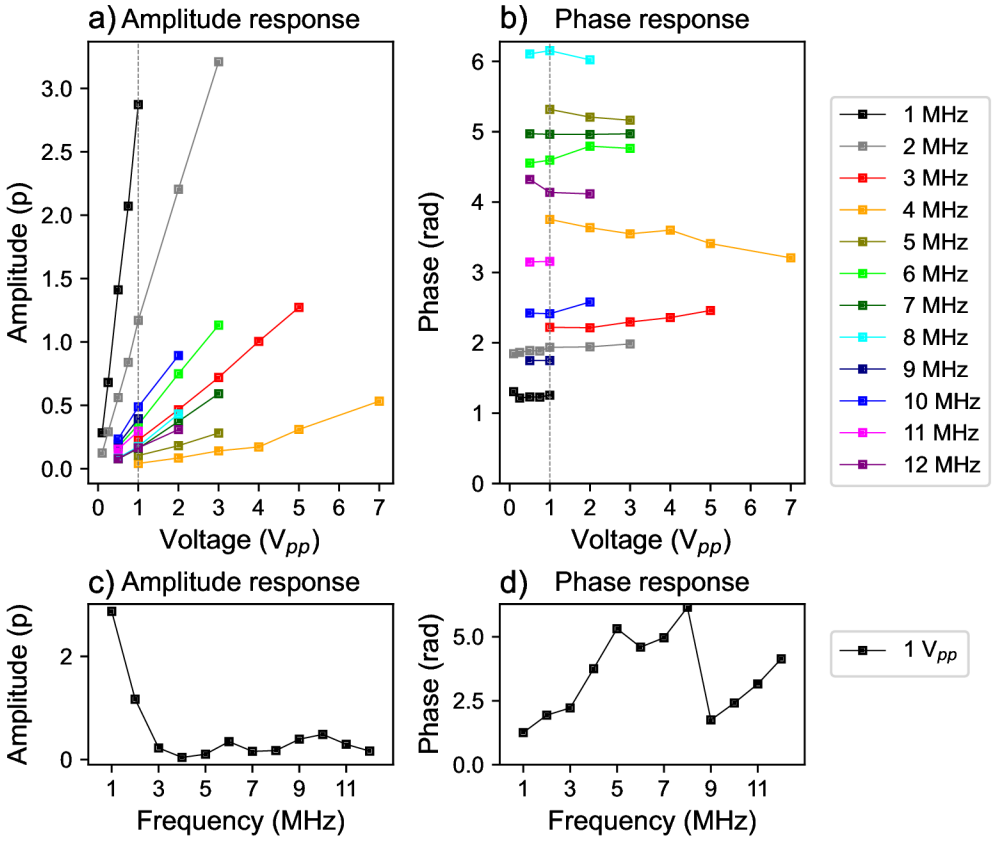

Figure 12: *Frequency response function between driving voltage and absorber motion. Amplitude and the phase response in the dependence on the driving voltage for individual frequencies are shown in the parts a) and b) respectively. The amplitude and phase response for constant driving voltage 1 V_{pp} are shown in the parts c) and d) respectively.*

3.3 Data Fitting

The proper method of fitting the time histograms is crucial for obtaining the correct values of the harmonic motion parameters ,i.e. for measuring the frequency response, and also for comparing the simulations with the experiments. This task is not so simple because, in our case, the function describing the intensity of radiation in time depends on twelve parameters. In addition, some of the parameters are un-

desirably correlated which affects the precision of the results. For this reason, it is necessary to measure and fix as many parameters as possible, and the instructions on how to carry this out are provided in the present section.

Let's list all the parameters, which are involved in the fitting of the radiation intensity scattered in the harmonically vibrating absorber. In such case, the normalised radiation intensity $I(t)$, depends on frequency f, amplitude p and phase ϕ of the Mössbauer absorber motion, the energy detuning ΔE, linewidth of the source Γ_s and the Mössbauer absorber parameters such as absorber linewidth Γ_a, effective thickness d_{eff} and hyperfine magnetic field B_{hf}. Furthermore, the fitting of the experimental data requires other parameters such as the number of counts N, time resolution of the apparatus σ_t, normalised amplitude of the non-resonant background A_{bcg} and the exponential countrate decay constant C_{bcg}. The latter parameter is introduced to describe a gentle inclination in the number of counts, which is observed for the longer time intervals in the time histograms. This is due to the way the time interval is measured. Only the first 14 keV photon is registered after the start pulse, not all of them. Since the photons arrive randomly relative to the start pulse, the probability that the longer time interval is measured decreases exponentially in dependence on the countrate of the 14 keV photons.

The function utilised for fitting the experimental data $I_{exp}(t)$ is given by a convolution of the radiation intensity scaled to the experimental data $I_s(t)$ and the Gaussian time resolution $G(t)$ of the apparatus,

$$I_{exp}(t) = I_s(t) * G(t), \tag{13}$$

where

$$G(t) = \frac{1}{\sqrt{2\pi}\sigma_t} e^{-\left(\frac{t}{\sqrt{2}\sigma_t}\right)^2} \tag{14}$$

covers the parameter σ_t which is related to the FWHM of the time resolution as FWHM $\approx 2.35\sigma_t$. The other experimental parameters N, A_{bcg} and C_{bcg} are included in the scaled radiation intensity $I_s(t)$, which has a form

$$I_s(t) = \left(\frac{I(t) + A_{\text{bcg}}}{1 + A_{\text{bcg}}}\right) N e^{-\frac{t}{C_{\text{bcg}}}}. \tag{15}$$

The rest of the parameters, i.e. Γ_s, Γ_a, p, ϕ, f, ΔE, d_{eff} and B_{hf}, are covered in the normalised radiation intensity $I(t)$.

From the parameters listed above, the p and ϕ are the subjects of interest. The frequency f Doppler energy detuning ΔE and hyperfine parameters of the source belongs among the parameters which can be fixed easily. Frequency generation is well controlled and very precise. In the case of the energy modulation control, the precision of $\pm\, 0.2$ MHz was expected, which was supposed to be sufficient. Since the parameters of the radioactive source are not easy to be measured, we used, in accordance with the work [21], the single Lorentzian line shape having the linewidth $\Gamma_s = 1.2\Gamma_0$. For the absorber, we took the natural linewidth $\Gamma_a = \Gamma_0$ in account. But then, it is essential to measure precisely and fix the absorber effective thickness d_{eff} and hyperfine magnetic field B_{hf}. Since the obtaining of these values from the common transmission Mössbauer spectrum we find to be misleading, the better method of utilising the resonant detector is introduced.

The fixation of the eight parameters mentioned above is not enough. When trying to fit the data this way, there were significant differences in the motion amplitudes

p, time resolutions σ_t and background amplitude levels A_{bcg} obtained from the first and second time histogram. However, it cannot be true, since these three parameters have to be the same for both time histograms. This reveals that there is a mutual correlation between these parameters.

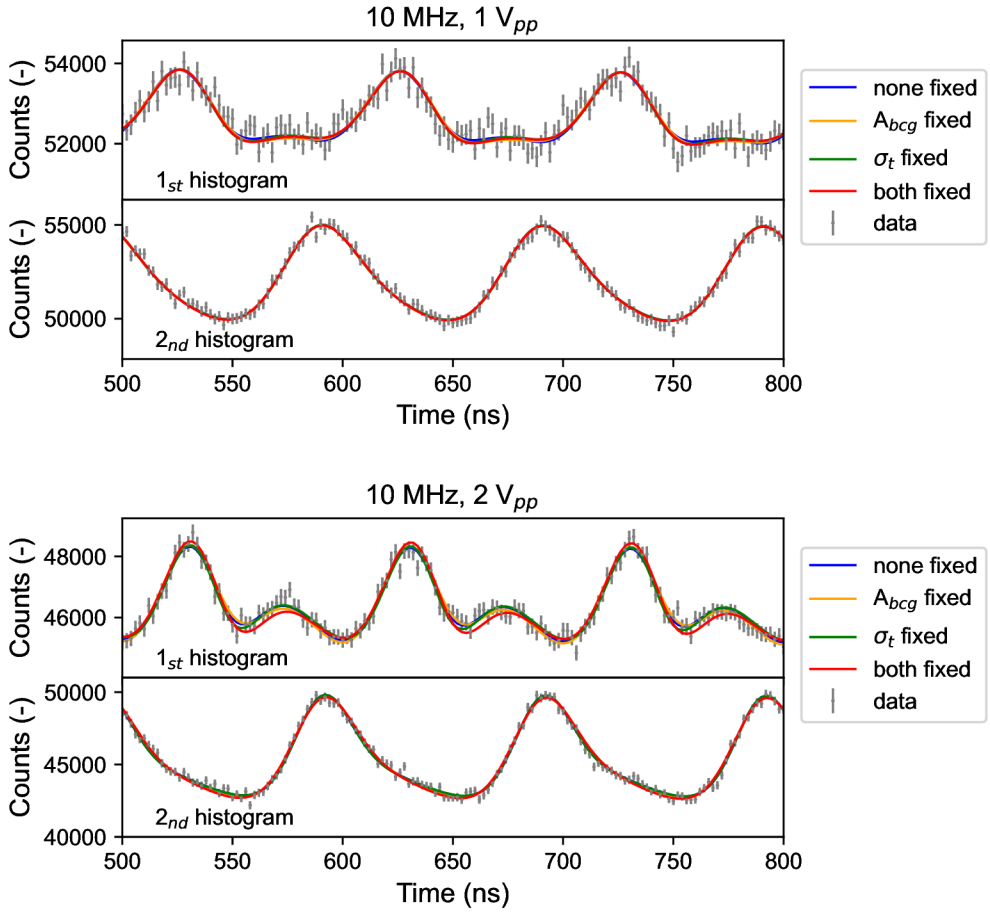

Figure 13: *Demonstration of the different curves fitted in two pairs of time histograms of the harmonically vibrating absorber at 10 MHz driven by voltage 1 V_{pp} and 2 V_{pp}. Individual fits differ in fixing the parameters A_{bcg} and σ_t.*

We believe that the most relevant results are obtained when the time resolution and the background level are precisely measured and fixed because then the fitted parameters from the both time histograms are maximally unified. Nevertheless, in few measurements (mostly for higher driving voltages) the parameter p differs by almost 13 % between the first and the second time histogram. We understand this as a result of possible errors in the fixed parameters or also the inhomogeneous motion of the absorber [27], whose influence on the shape of the radiation intensity in the time domain has not yet been properly investigated in this work.

After the fixation of the σ_t and A_{bcg}, last four parameters remain free in the fitted function. Specifically, besides the p and ϕ, the number of counts N, and the countrate constant C_{bcg} are fitted. All of these parameters are independent. The parameter p defines the shape of the intensity waveform and ϕ moves it along the time axis. Number of counts positions the time waveform according to y-axis and the countrate constant determines its inclination.

3.4 Intensity Control Results

In this section, the results of the gamma radiation intensity control induced by four basic motion profiles of different amplitudes at divers energy detunings are presented to confirm the feasibility of the predictions made in Subsection 1.2.2. Specifically, the triangular, trapezoidal, square and bipolar-pulse like motion waveforms composed of six or twelve harmonics with fundamental frequency $f = 2\,\mathrm{MHz}$ or $f = 1\,\mathrm{MHz}$ respectively were utilised. For each of these, a corresponding driving voltage waveform had to be calculated. In this calculation, a particular ideal motion profile of specific amplitude was created first. Subsequently, this motion waveform was decomposed into Fourier series and reassembled from only six or twelve Fourier components, depending on the intended fundamental frequency. In this way, the required motion amplitudes and phases of each harmonic frequency were obtained.

In the next step, the frequency response function was utilised to calculate the corresponding amplitudes and phases of the driving voltage waveform components. Since the frequency response was measured at certain points the values in between were linearly interpolated[1].

The generated voltage waveforms were applied to the piezotransducer and the measured radiation intensity waveforms were compared to the predictions calculated from the expected motion profile. In practice, the parameters p and ϕ were fixed and only the number of counts N, and the countrate constant C_{bcg} were fitted. For the lower amplitude motions ($\Delta p < 3.5$, i.e. $< 48\,\mathrm{pm}$), which require relatively small amplitudes of higher frequency components, we got a very good agreement of the experiments with the predictions. These results are presented in Subsection 3.4.1. In the opposite case, for the higher motion amplitudes, a deterioration of the intensity control was observed which is thought to be caused due to the nonlinear behaviour of the piezotransducer. These cases are presented and discussed in Subsection 3.4.2.

The radiation intensity waveforms presented in the following subsections are depicted in the normalised form $I_n(t)$, which shows approximately the normalised intensity $I(t)$ convolved with the time resolution function. Written in the equation, the $I_n(t)$ is obtained when the measured data $I_{exp}(t)$ are normalised and the background is subtracted as follows

$$I_n(t) = I_{\mathrm{exp}}(t) \left(\frac{1 + A_{\mathrm{bcg}}}{N e^{-\frac{t}{C_{\mathrm{bcg}}}}} \right) - A_{\mathrm{bcg}}\,. \tag{16}$$

This form was chosen because it allows comparison of intensity levels between the individual measurements. Further, the origin of the time axis of the displayed data is related to the beginning of the motion profile period. It is possible to notice that not the full 2μs but a shorter time histogram is displayed. This is due to the cutting of the first 340 ns of the time histograms because the numerical fit in this region was disrupted by numerical artefacts.

[1] A linear interpolation of the amplitude response function for low amplitudes of the driving voltage and motion was drawn from the origin to the first measured point. In the case of the phase response function, the interpolation value of the phase towards zero driving voltage was kept the same as in the nearest measured point.

3.4.1 Results of Individual Motion Profiles

Triangular Motion: Experimental results measured for two triangular motion profiles, which were composed of twelve and six harmonics with $f = 1$ and $f = 2\,\mathrm{MHz}$ respectively, are shown in Figure 14. In both measurements, the energy detuning of the source was $\Delta E = 3\,\mathrm{MHz}$ (foot of the resonant line). The absorber position changed of approximately 120 pm and 60 pm in 500 ns and 250 ns respectively, which gives the velocity $\pm 0.23\,\mathrm{mm/s}$ corresponding Doppler to energy modulation $\pm 2.8\,\mathrm{MHz}$. Thus the energy of the incident radiation was tuned by the motion of the absorber near to the resonance ($\Delta E = 0.2\,\mathrm{MHz}$) when moving in one direction and more out of the resonance ($\Delta E = 5.8\,\mathrm{MHz}$) in the other direction. Specifically, these results show that the triangular motion profile could be used for fast gating of the gamma radiation intensity with an approximate duty cycle of 50 %.

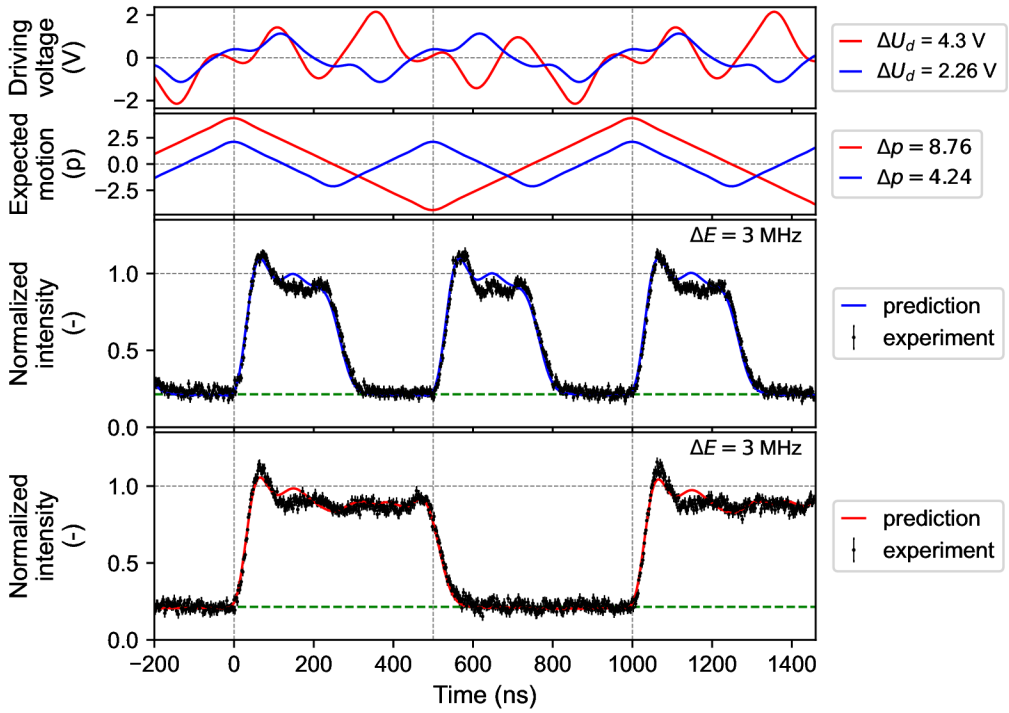

Figure 14: *Radiation intensity waveforms (black) induced by the absorber vibrating according to the triangular motion profiles. The corresponding driving voltage waveforms and predicted radiation intensities for the triangular motion profile consisting of 12 harmonics($f = 1\,MHz$) and 6 harmonics ($f = 2\,MHz$) are drawn in red and blue lines respectively. A green dashed line labels the radiation intensity in the resonance.*

Trapezoidal Motion: The single gamma pulses and the short-time absorption induced by two trapezoidal motion profiles are depicted in Figure 15. When the energy of the photons was tuned close to resonance ($\Delta E \approx 1\,\mathrm{MHz}$) the single gamma pulses about 55 ns wide (FWHM) with intensity exceeding the incident level 1.5 times were generated. Conversely, if the energy of the incident photon was tuned about 5 MHz outside the resonance, the absorption was induced for 60–80 ns.

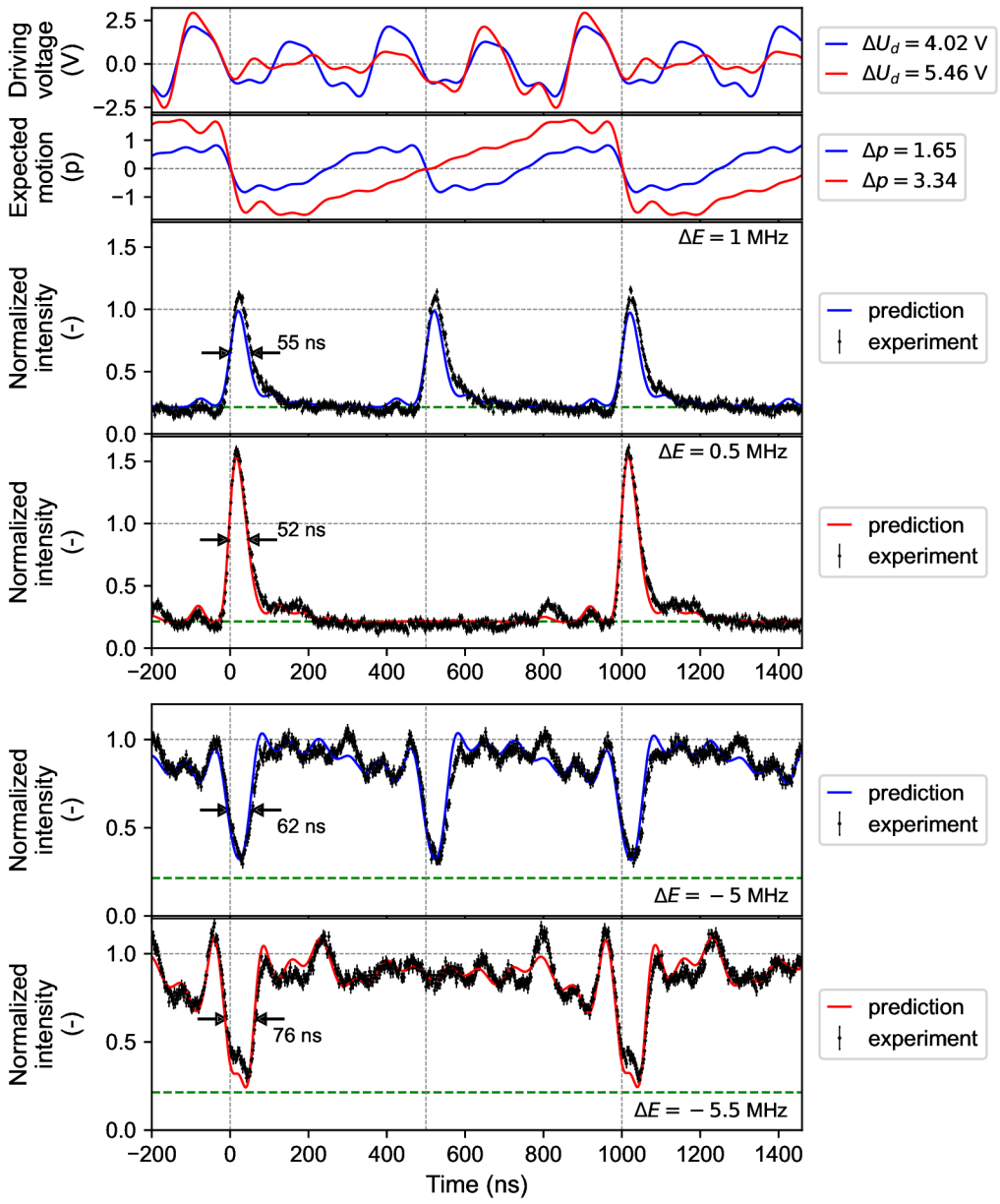

Figure 15: *Radiation intensity waveforms (black) of the single gamma pulses (the first two intensity graphs) and short-time induced absorption (the last two intensity graphs) generated by trapezoidal motion profiles of the absorber. The corresponding driving voltages and predicted radiation intensities for the trapezoidal motion profiles consisting of 12 harmonics ($f = 1\,MHz$) and 6 harmonics ($f = 2\,MHz$) are drawn in red and blue lines respectively. A green dashed line labels the radiation intensity in the resonance.*

Square Motion: Doubling of the gamma pulses frequency is demonstrated on the square motion profile. If the energy of the incident photons was tuned exactly to the resonance, then the both absorber jumps back and forth created almost identical single gamma pulses 50 ns wide (FWHM) with the intensity enhanced approximately 1.5 times. However, the fast jumps at the square motion profile can be utilised also to induce the short-term absorption same as the trapezoidal motion profile if the energy is tuned out of the resonance. However, only one direction jump have the required effect, see Figure 16.

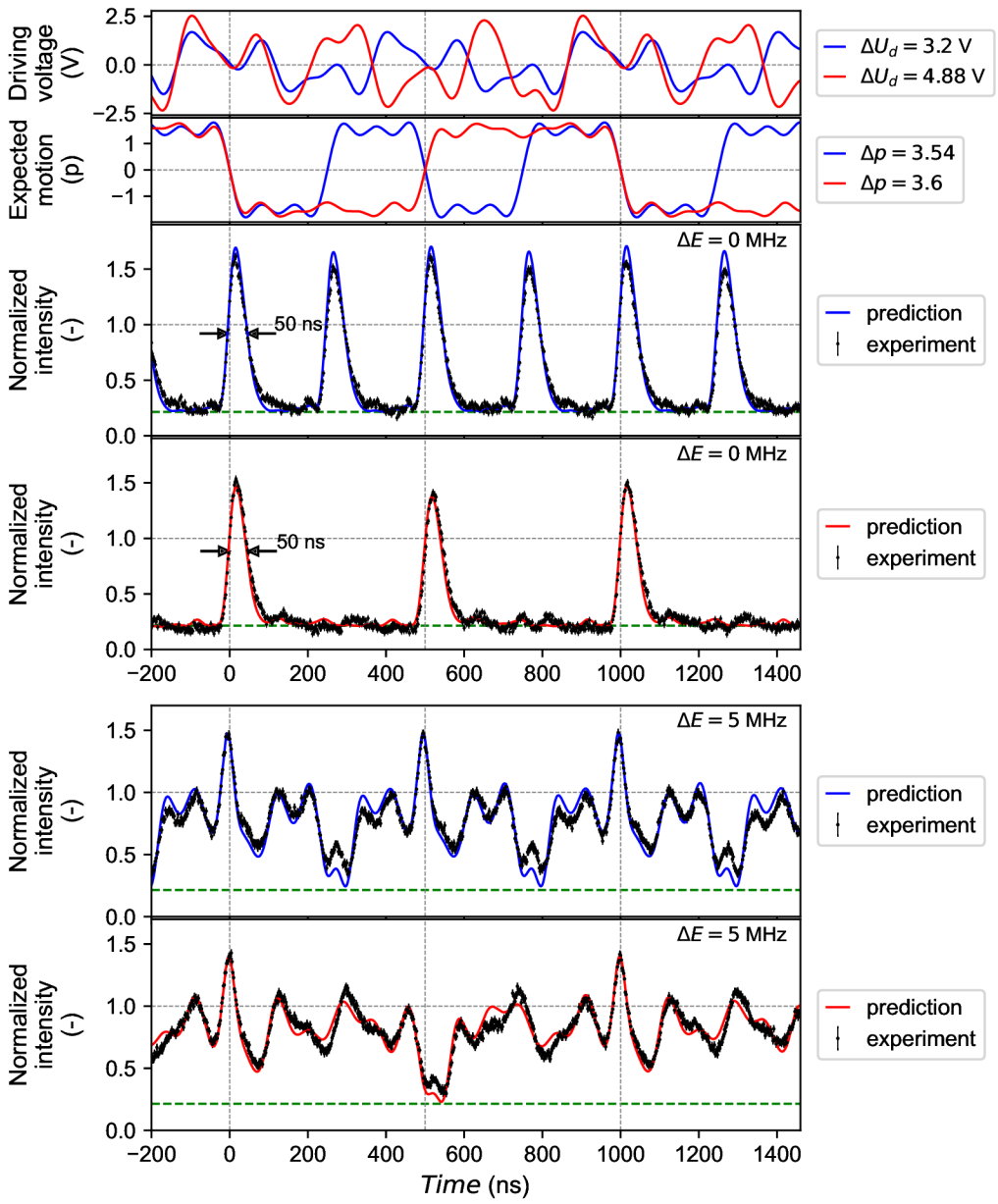

Figure 16: *Radiation intensity waveforms (black) of the single gamma pulses (the first two intensity graphs) and short-term induced absorption (the last two intensity graphs) generated by square motion profiles of the absorber. The corresponding driving voltages and predicted radiation intensities for the trapezoidal motion profile consisting of 12 harmonics ($f = 1$ MHz) and 6 harmonics ($f = 2$ MHz) are drawn in red and blue lines respectively. A green dashed line labels the radiation intensity in the resonance.*

Bipolar Pulse Motion: The generation of the single and double gamma pulses by the bipolar pulse motion profile, when the energy of the incident photons was tuned to the left ($\Delta E = -1\,\mathrm{MHz}$) and right ($\Delta E = 1.5\,\mathrm{MHz}$) side of the resonance, is shown in Figure 17. The positive energy detuning resulted in a generation of the single pulses with FWHM of 44 ns and the negative detuning created the double pulses, where each pulse has a FWHM about 30 ns.

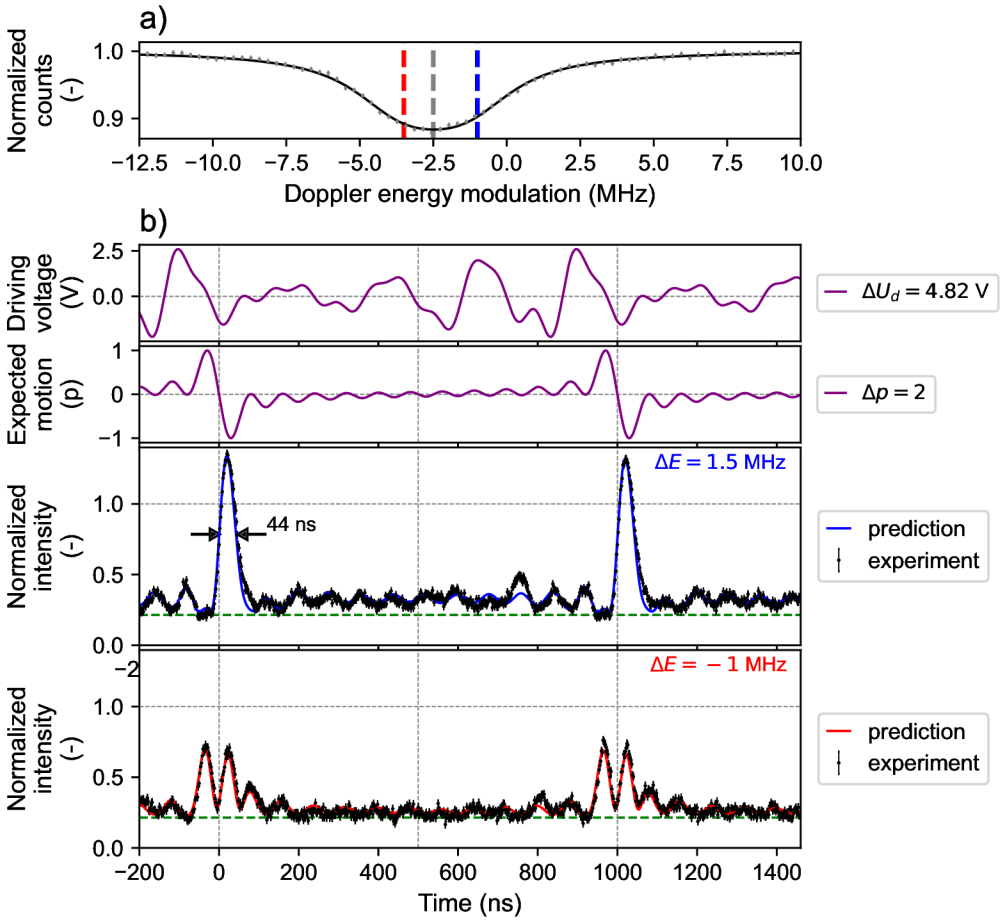

Figure 17: *Mössbauer spectrum of the absorber, part a), and radiation intensity waveforms of the single and double gamma pulses generated by the bipolar pulse shaped motion profile of the absorber for different energy detuning labelled by blue and red lines, part b). A green dashed line labels the radiation intensity in the resonance.*

3.4.2 Imperfections and Limits

A good agreement of the predictions with the experiments, which were shown in the previous section, was mostly achieved by a manual suppression of the amplitudes of the 4 MHz and 5 MHz frequency, i.e. the frequencies of the minimum amplitude response, recall Figure 12. Although this action slightly altered the expected motion profile, the effect on the measured intensity waveform and the maximum amplitude of the driving voltage was considerable. The impact of suppressing these frequencies is shown in Figure 18. The amplitudes were reduced to the half except for the motion profile consisting of even frequencies, where the amplitude at 4 MHz was decreased to one third. The observed behaviour remains unexplained, but we offer a few hypotheses. The first is that the amplitude response at the local minimum actually varies rapidly in time and we are only measuring the average mechanical response. It means that the motion of the Mössbauer absorber is not ideally periodic and its deflections from the average cause the substantial changes in the radiation intensity waveforms. The second hypothesis is that we encounter some nonlinear behaviour of the piezotransducer at these frequencies.

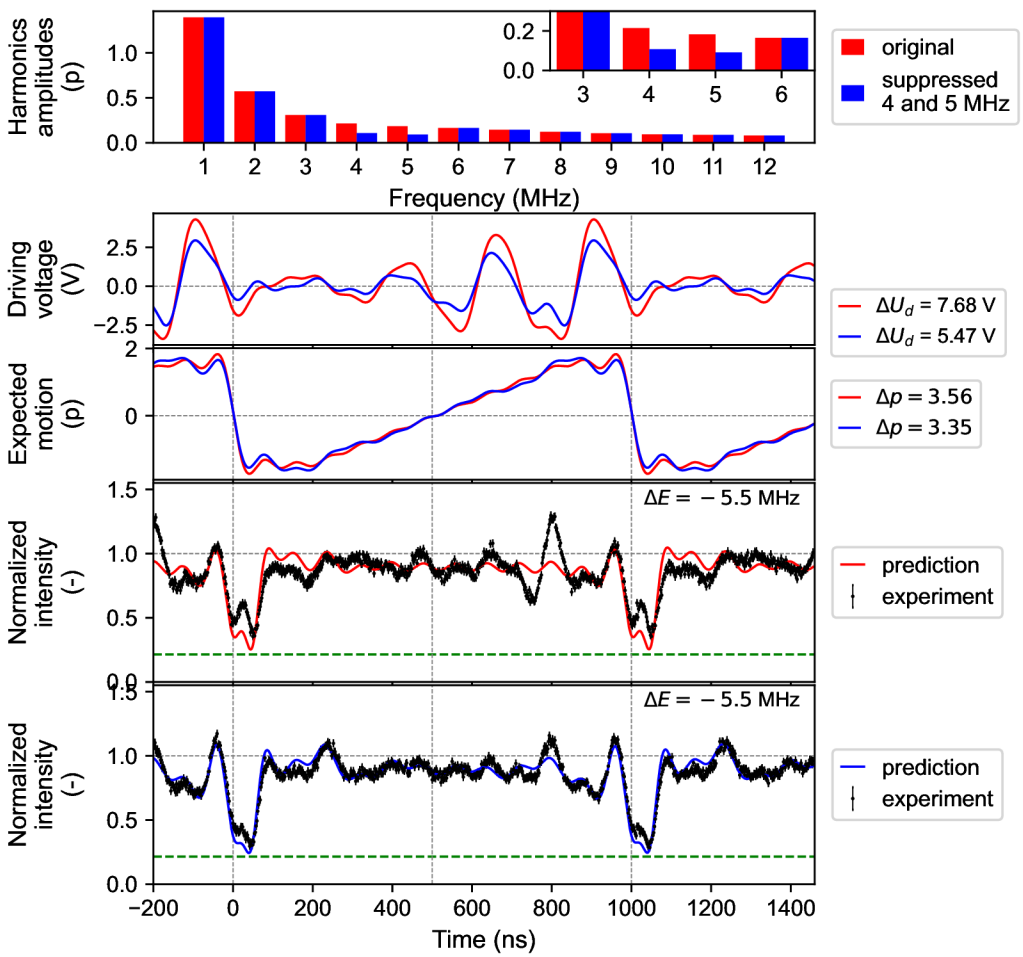

Figure 18: *Influence of the 4 and 5 MHz frequency suppression on the radiation intensity control. Amplitudes of both frequencies were decreased to the half. Corresponding harmonics amplitudes, driving voltage waveform, expected motion profile and predictions are labelled by red and blue colour.*

The second hypothesis is further supported by the fact that the attempts to control the radiation intensity using higher amplitude motion profiles with $\Delta p > 3.5$ were unsuccessful. Even though the two frequencies mentioned above were suppressed to a sufficiently low level (to the half or third), the discrepancy between the predictions and the experiment was larger when the absorber motion amplitude increased, see Figure 19. It is possible that we have omitted other problematic frequencies, but we think that we got into a nonlinear region of the piezotransducer. Nevertheless, it is evident that the higher absorber jumps led to the generation of more narrower (25 ns FWHM) and more intensive pulses exceeding the input intensity 1.7 times.

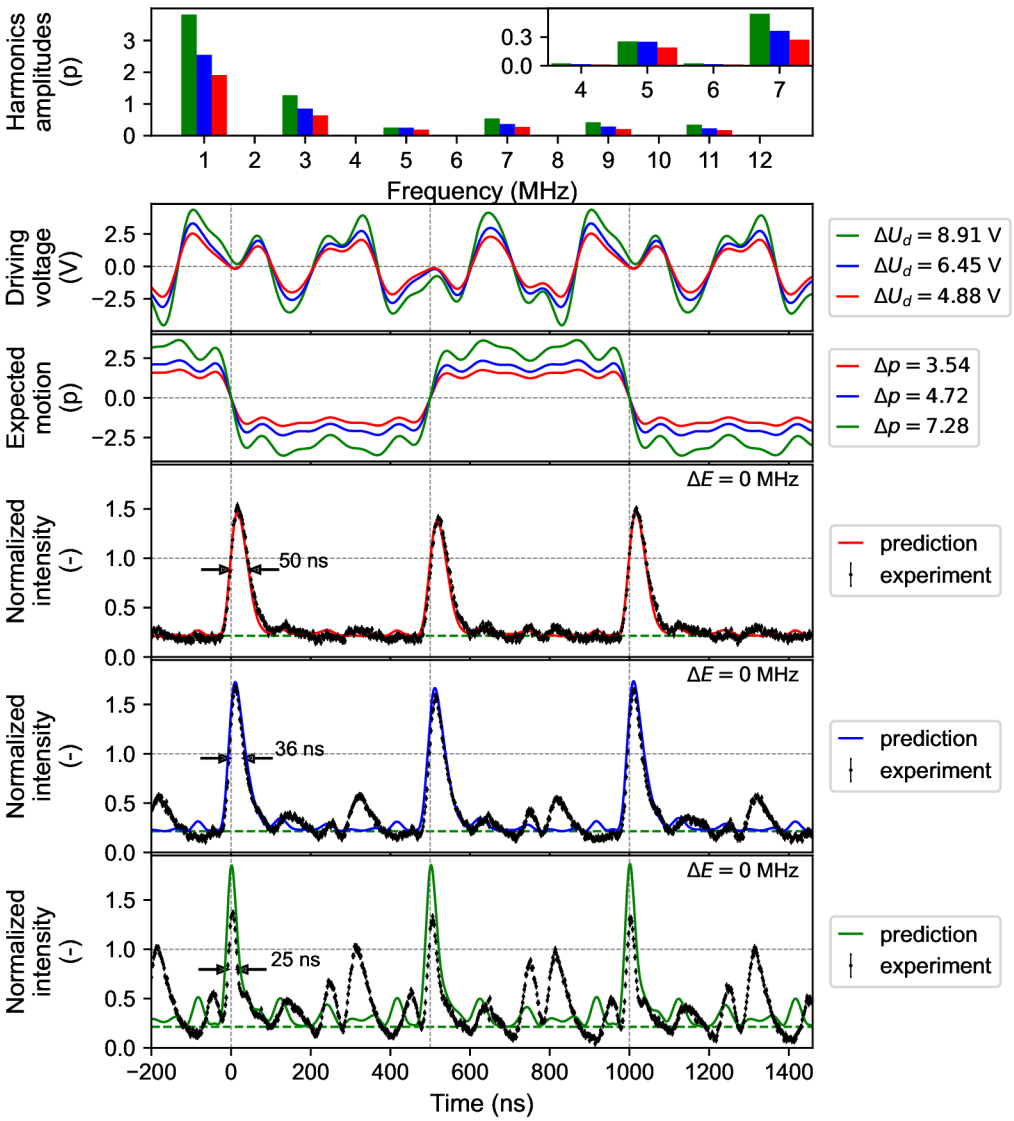

Figure 19: *Radiation intensity control for different amplitudes of the square-like motion profiles. Corresponding harmonics amplitudes, driving voltage waveform, expected motion profile and predictions are labelled by green, blue and red colour. Amplitude of the 5 MHz frequency was reduced to the third in the case of green waveform and to the half for the blue and red waveform.*

3.5 Potential Applications and Further Development

The interference effects induced by the harmonically vibrating Mössbauer absorber bring a variety of potential applications. In this work, it was shown that the interference of the 14 keV gamma photons from a ^{57}Co source can be used for measuring the harmonic vibrations on the picometre scale at frequencies in the range of several megahertz. If less used Mössbauer sources [49, 50] were exploited, this concept could be further developed to measure the vibrations amplitudes in femtometre range and kilohertz or, contrarily, gigahertz frequencies. Thus, gamma radiation interference could be an interesting tool for the research of the fast low-amplitude vibration modes of the piezoelectric materials and their frequency characterisation. Furthermore, it was presented that the radiation intensity time structures of the specific shapes such as double and triple pulses can be used to determine the time resolution of the single gamma radiation detector.

The generation of the high-intensity, in-time narrow single gamma pulses by the presented technique enables the development of a table-top radioactive gamma pulse source. Such an instrument would be used to study nuclear quantum dynamics, and to perform the pump probe and interferometric experiments with gamma photons. Moreover, if a stainless steel absorber is replaced by the magnetically split one, it allows to generate polarized gamma pulses[2], which could be utilised, besides the gamma optics experiments, also for the construction of the table-top polarised Mössbauer spectrometer. Note that the method of gamma radiation control presented in this work is independent of the source activity, so the gamma pulser can reach high intensities.

The shaping of the gamma radiation intensity into the forms different from the single pulses brings other applications. The phenomenon of the short-time induced absorption observed in this work suggests the possibility of development of a time and energy selective gamma radiation detector. Moreover, a generation of the multi-pulse structures could be a subject of interest in the area of gamma single-photon mode entanglement, where in-time separated modes in the form of pulses were proposed [34]. In general, the arbitrary driving voltage should allow to generate various waveforms of the gamma radiation intensity, see Figure 20 where an example of arbitrary motion profile leads to a generation of three different pulses. Thus, sequences of the multiple structures (single pulses, double pulses, absorption) of various amplitudes, widths and time positions could be generated. In addition, if the non-periodic motions of the absorber, e.g. single jumps, were properly controlled, it would also be possible to manipulate the individual gamma photons in real time. This kind of gamma-photon control could be potentially applied in the field of quantum computing, quantum memories or quantum cryptography.

The presented method of gamma radiation control can be further developed both practically and theoretically. On the technological side, the piezotransducers could be improved to manage larger amplitudes at higher frequencies. This involves not only adjusting the mechanical design of the PVDF foils or the absorber, but also the search for better piezoelectric materials. For example quartz-based ETNA piezotransducers utilised in Ref [51] seem to be a promising candidate. It would also be quite interesting to find the piezoelement that manages to move the radioactive source at high frequencies, since the situation of vibrating source or absorber is equivalent. Additionally, some cooling technology ensuring a lower or even stable temperature could be useful

[2] Few experiments with a harmonically vibrating magnetic α-iron foil have been already performed in our research group and the pulses with partially separated Π and σ polarisations were observed.

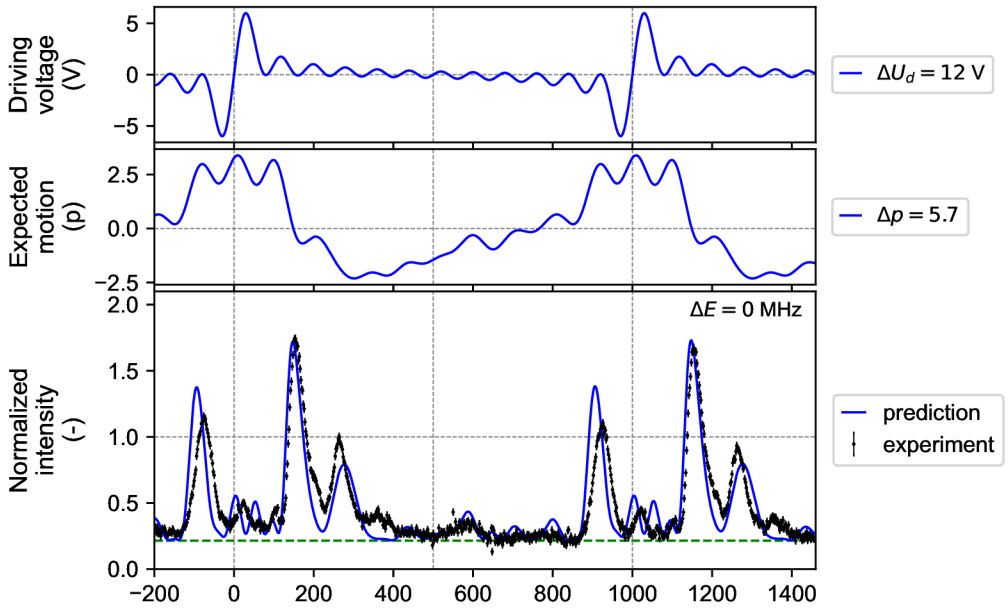

Figure 20: *Example of arbitrary radiation intensity waveform controlled by the bipolar-pulse shaped driving voltage. The expected absorber motion profile, which creates three gamma pulses with diverse amplitude in different times, was calculated using the driving voltage and frequency response function.*

to solve the problem with heating of the piezotransducer.

Frequency response of the piezotransducer could be further improved by decreasing the weight of the absorber. Assuming that 12 mg stainless steel absorber (on our piezotransducer) moves harmonically with 30 pm amplitude at 10 MHz frequency, the piezofoil has to exert the force of about 1 kN to move the absorber. If enriched absorbers were utilised, the weight could be reduced by a factor of about forty seven (2.119 % natural abundance ^{57}Fe) for the same effective thickness. Such a change could have a significant impact on the piezotransducer frequency response. In addition, the physical thickness of the enriched absorbers ranges from several hundreds of nanometres up to only a few micrometres, which means a significant reduction of the electronic absorption losses of the gamma radiation in the absorber. On the other hand, the production of such a thin foils is not common and, in general, a manual gluing of the metal foils, especially the extra thin ones, to the piezoelements requires a skill. For this reason, other techniques such as sputtering or electrolysis of the absorber on the surface of the piezoelement could be used, which could also improve the reproducibility of the piezotransducers (compared to the manual gluing).

Next, the methodology of frequency response measuring could be accelerated by the application of more frequencies simultaneously. Indeed, it has to be ensured that the system behaves linearly, but the measurement of the response function could be reduced to units of measurements instead of several tens. However, this requires much more complicated fitting, which could perhaps be simplified if the theoretical description of the radiation intensity control by a multi-tone vibrating absorber was mastered analytically. The simplification of the calculation would also help to solve the inverse problem of what shape of motion profile has to be applied in order to obtain the required radiation intensity profile. In this work, only four basic motion

profiles were introduced, but it is not excluded that there are other arbitrary motion profiles which allow to generate different radiation intensity structures as indicated in Figure 20. For example, the better motion profile could be found to acoustically induce the absorption of rectangular shape and specific time width.

Finally, we suggest some additional hints. In principle, the radiation control method could be further improved by adding more individually vibrating absorbers. Such a setup, where not only singlet but also doublet or sextet absorbers are employed in the experiment, could be interesting for a further investigation of gamma radiation slowing down [52]. More vibrating absorbers are also interesting from the point of view of the nuclear dynamics when the gamma photon interaction with two nuclei ensembles moving in opposite direction during the interaction, can be investigated.

Conclusion

In the present work, the coherent control of gamma radiation intensity by the Mössbauer absorber which vibrates according to motion profiles defined by Fourier series was described from the simulations to the experiment. Although no deeper analytical advance was made, the resonant scattering in the absorber vibrating with the arbitrary motion profile was solved numerically. The optimised Python script was appended to this work.

The numerical calculations were used to investigate the potential of gamma radiation intensity control specifically by triangular, trapezoidal, square and bipolar pulse motion profiles. The triangular motion profile was used to demonstrate that the gamma resonant scattering in the vibrating absorber can be understood as a result of the additional interference effect induced by the change of energy modulation within the excitation time. Further simulations showed that the variation of the absorber motion profile provides much broader possibilities for controlling the temporal properties of the gamma radiation intensity. Besides the narrow high-intensity single gamma pulses, short-time acoustically induced absorption and well separated high-intensity double pulses were predicted.

The necessary equipment for performing the radiation intensity control experiments was developed. Within this, the dual-channel Mössbauer spectrometer was upgraded to a universal DAQ system for nuclear quantum experiments, allowing to measure besides energy spectra also time histograms and TDMS spectra. The key part of the upgrade was implementation of the TDC and asynchronous amplitude discriminator in FPGA, which ensures data processing on hardware level. Further, the piezodriver and piezotransducer were created to move the Mössbauer absorber at megahertz frequencies and picometre amplitudes.

To control the motion profile of the absorber, it was necessary to measure frequency response of the piezotransducer system. For this purpose, the methodology based on gamma radiation scattering in the harmonically vibrating absorber was developed and described in detail. Using the frequency response function, the driving voltage waveforms for the piezotransducer were calculated to generate the required motion profiles of the absorber. Subsequently, The predicted shaping of the gamma radiation intensity into single pulses, double pulses and short-time acoustically induced absorption was experimentally proven. For lower amplitudes of the absorber motion ($\Delta p < 3.5$), the results were in good agreement with the predictions. For higher amplitudes, the imperfections and limitations, specifically a nonlinearity of the piezotransducer, were discussed.

Possible applications of the presented technique for controlling the intensity of gamma radiation include the construction of the table-top source of gamma pulses, which could be even polarised, opening the doors to the table-top polarised Mössbauer spectrometer. The gamma pulses could be further exploited for studying the nuclear quantum dynamics or single photon quantum entanglement. At the end, the possible improvements were suggested. The intensity control technique can be further developed both experimentally and theoretically. For example, a proper analytical description is lacking, better piezotransducers and absorbers could be used, or the concept could be extended to more vibrating absorbers.

Shrnutí v českém jazyce

Práce popisuje od simulací až po experiment koherentní řízení intenzity gama záření pomocí vibrujícího Mössbauerova absorbátoru, jehož pohybový profil je definovaný Fourierovou řadou. Ačkoliv nebyl učiněn pokrok v analytické části, byl rezonanční rozptyl v absorbátoru vibrujícím s libovolným průběhem pohybu vyřešen numericky. Optimalizovaný výpočetní skript psaný v Pythonu je přílohou této práce.

Numerickými simulacemi byly zkoumány možností řízení intenzity gama záření pomocí vybraných průběhů pohybu absorbátoru konkrétně trojúhelníkového, lichoběžníkového, čtvercového a průběhu ve tvaru bipolárního pulzu. Na trojúhelníkovém průběhu pohybu bylo demonstrováno, že lze rezonanční rozptylu gama záření na vibrujícím absorbátoru chápat jako aditivní interferenční efekt, který je vyvolán rychlou změnou modulace energie v době existence excitovaného stavu. Další simulace ukázaly, že ladění pohybového profilu absorbátoru poskytuje mnohem bohatší možnosti řízení časové struktury intenzity gama záření. Kromě úzkých jednoduchých gama pulzů vysoké intenzity byly dále předpovězeny krátkodobé akusticky indukovaná absorpce a v čase dobře oddělené dvojité pulzy vysoké intenzity.

Pro provádění experimentů řízení intenzity gama záření bylo vyvinuto potřebné vybavení. V rámci toho byl dvoukanálový Mössbauerův spektrometr vylepšen do podoby univerzálního systému pro sběr dat v experimentech jaderné kvantové optiky, který umožňuje měřit kromě energetických spekter také časové histogramy a časově rozlišená Mössbauerovská spektra. Klíčovou součástí vylepšení byla implementace převodníku pro měření času a asynchronního amplitudového diskriminátoru v FPGA, což umožňuje zpracování dat na hardwarové úrovni. Dále byl vytvořen piezodriver a piezotransducer, které umožňují pohybovat Mössbauerovým absorbátorem na megahertzových frekvencích a s pikometrovými amplitudami.

Aby mohl být průběhu pohybu absorbátoru správně kontrolován, bylo nutné změřit frekvenční odezvu celého systému piezotransduceru. Pro tento účel byla vyvinuta a podrobně popsána metodika, která je založená na rozptylu gama záření v harmonicky kmitajícím absorbátoru. S použitím funkce frekvenční odezvy pak byly vypočteny průběhy řídicího napětí pro piezotransducer, které vedly ke generování požadovaných profilů pohybu absorbátoru. Předpovídané tvarování intenzity záření gama do jednoduchých pulzů, dvojitých pulzů a krátkodobá akusticky indukovaná absorpce byly experimentálně prokázány. Pro nižší amplitudy pohybu absorbátoru ($\Delta p < 3,5$) byly výsledky ve velice dobré shodě s předpověďmi. V případě vyšších amplitud pak byly diskutovány nedokonalosti a omezení, konkrétně nelineární chování piezotransduceru.

Možné aplikace prezentované techniky řízení intenzity gama záření zahrnují konstrukci stolního zdroje gama pulzů, které by mohly být i polarizované, což by otevřelo dveře stolnímu polarizovanému Mössbauerovu spektrometru. Impulsy gama by mohly být dále využity ke studiu jaderné kvantové dynamiky nebo kvantového provázání jednotlivých fotonů. Na závěr byla navržena možná vylepšení. Tato technika řízení intenzity může být dále rozvíjena jak experimentálně, tak teoreticky. Například chybí lepší analytický popis, mohly by se použít jiné piezotransducery a absorbátory nebo by koncept řízení mohl zahrnovat více vibrujících absorbátorů.

References

[1] N. N. Greenwood and T. C. Gibb, *Mössbauer Spectroscopy*. Springer Netherlands, 1971.

[2] G. N. Belozerski, *Mössbauer studies of surface layers*. Studies in Physical and Theoretical Chemistry, London, England: Elsevier Science, 1993.

[3] P. Gütlich, E. Bill, and A. X. Trautwein, *Mössbauer Spectroscopy and Transition Metal Chemistry*. Springer-Verlag Berlin Heidelberg, 2011.

[4] T. J. Bürvenich, J. Evers, and C. H. Keitel, "Nuclear quantum optics with X-Ray laser pulses," *Phys. Rev. Lett.*, vol. 96, p. 142501, 2006.

[5] J. Odeurs, G. Hoy, Y. Rostovtsev, and R. Shakhmuratov, "Towards more relaxed conditions for a gamma-ray laser: Methods to realize induced transparency for nuclear resonant gamma radiation," *Laser & Photonics Reviews*, vol. 4, no. 1, pp. 1–20, 2010.

[6] W. Liao, A. Pálffy, and C. H. Keitel, "Coherent storage and phase modulation of single hard-x-ray photons using nuclear excitons," *Phys. Rev. Lett.*, vol. 109, p. 197403, 2012.

[7] W. Liao, A. Pállfy, and C. H. Keitel, "Three-beam setup for coherently controlling nuclear-state population," *Phys. Rev. C*, vol. 87, p. 054609, 2013.

[8] E. Kuznetsova and O. Kocharovskaya, "Quantum optics with X-rays," *Nature Photonics*, vol. 11, no. 11, pp. 685–686, 2017.

[9] K. P. Heeg, A. Kaldun, C. Strohm, C. Ott, R. Subramanian, D. Lentrodt, J. Haber, H. Wille, S. Goerttler, R. Rüffer, C. H. Keitel, R. Röhlsberger, T. Pfeifer, and J. Evers, "Coherent X-ray-optical control of nuclear excitons.," *Nature*, vol. 590, pp. 401–404, 2021.

[10] F. J. Agee, "Review of induced gamma emission and gamma-ray laser research," *Hyperfine Interactions*, vol. 143, no. 1, pp. 1–6, 2002.

[11] L. Rivlin, "Nuclear gamma-ray laser: the evolution of the idea," *Quantum Electronics*, vol. 37, no. 8, p. 723, 2007.

[12] S. L. Ruby and D. I. Bolef, "Acoustically modulated γ rays from Fe^{57}," *Phys. Rev. Lett.*, vol. 5, pp. 5–7, 1960.

[13] T. E. Cranshaw and P. Reivari, "A Mössbauer study of the hyperfine spectrum of ^{57}Fe, using ultrasonic calibration," *Proceedings of the Physical Society*, vol. 90, no. 4, p. 1059, 1967.

[14] P. Helistö, I. Tittonen, M. Lippmaa, and T. Katila, "Gamma echo," *Phys. Rev. Lett.*, vol. 66, pp. 2037–2040, 1991.

[15] I. Tittonen, P. Helistö, M. Lippmaa, and T. Katila, "Mössbauer gamma echo," *Hyperfine Interactions*, vol. 71, 1992.

[16] I. Tittonen, M. Lippmaa, P. Helistö, and T. Katila, "Stepwise phase modulation of recoilless gamma radiation in a coincidence experiment: Gamma echo," *Phys. Rev. B*, vol. 47, pp. 7840–7846, 1993.

[17] G. J. Perlow, "Quantum beats of recoil-free γ radiation," *Phys. Rev. Lett.*, vol. 40, pp. 896–899, 1978.

[18] R. N. Shakhmuratov, F. Vagizov, and O. Kocharovskaya, "Radiation burst from a single γ-photon field," *Phys. Rev. A*, vol. 84, p. 043820, 2011.

[19] R. N. Shakhmuratov, "Transformation of subradiant states to superradiant states in a thick resonant medium," *Phys. Rev. A*, vol. 90, p. 013819, 2014.

[20] F. Vagizov, V. Antonov, Y. V. Radeonychev, R. N. Shakhmuratov, and O. Kocharovskaya, "Coherent control of the waveforms of recoilless γ-ray photons," *Nature*, vol. 508, no. 7494, pp. 80–83, 2014.

[21] Y. V. Radeonychev, I. R. Khairulin, F. G. Vagizov, M. Scully, and O. Kocharovskaya, "Observation of acoustically induced transparency for γ-ray photons," *Phys. Rev. Lett.*, vol. 124, p. 163602, 2020.

[22] I. R. Khairulin, Y. V. Radeonychev, V. A. Antonov, and O. Korchayovskaya, "Acoustically induced transparency for synchrotron hard x-ray photons," *Sci Rep*, vol. 11, no. 7930, 2021.

[23] P. Helistö, E. Ikonen, T. Katila, and K. Riski, "Coherent transient effects in Mössbauer spectroscopy," *Phys. Rev. Lett.*, vol. 49, pp. 1209–1213, 1982.

[24] V. A. Antonov, Y. V. Radeonychev, and O. Kocharovskaya, "γ-ray-pulse formation in a vibrating recoilless resonant absorber," *Phys. Rev. A*, vol. 92, p. 023841, 2015.

[25] R. N. Shakhmuratov, F. G. Vagizov, V. A. Antonov, Y. V. Radeonychev, M. O. Scully, and O. Kocharovskaya, "Transformation of a single-photon field into bunches of pulses," *Phys. Rev. A*, vol. 92, p. 023836, 2015.

[26] R. N. Shakhmuratov, "Transformation of the frequency-modulated continuous-wave field into a train of short pulses by resonant filters," *Phys. Rev. A*, vol. 95, p. 033805, Mar 2017.

[27] R. N. Shakhmuratov and F. G. Vagizov, "Application of the Mössbauer effect to the study of subnanometer harmonic displacements in thin solids," *Phys. Rev. B*, vol. 95, p. 245429, 2017.

[28] R. N. Shakhmuratov and F. G. Vagizov, "Mössbauer method for measuring sub-angstrom displacements of thin films," *JETP Letters*, vol. 108, no. 11, p. 772–776, 2018.

[29] S. S. Wang, Y. G. Ma, X. G. Cao, D. Q. Fang, and C. W. Ma, "Hard-photon production and its correlation with intermediate-mass fragments in a framework of a quantum molecular dynamics model," *Phys. Rev. C*, vol. 102, p. 024620, 2020.

[30] R. Röhlsberger, H.-C. Wille, K. Schlage, and B. Sahoo, "Electromagnetically induced transparency with resonant nuclei in a cavity," *Nature*, vol. 482, no. 7384, pp. 199–203, 2012.

[31] K. P. Heeg, A. Kaldun, C. Strohm, P. Reiser, C. Ott, R. Subramanian, D. Lentrodt, J. Haber, H.-C. Wille, S. Goerttler, R. Rüffer, C. H. Keitel, R. Röhlsberger, T. Pfeifer, and J. Evers, "Spectral narrowing of x-ray pulses for precision spectroscopy with nuclear resonances," *Science*, vol. 357, no. 6349, pp. 375–378, 2017.

[32] D. Lentrodt, K. P. Heeg, C. H. Keitel, and J. Evers, "Ab initio quantum models for thin-film x-ray cavity QED," *Phys. Rev. Res.*, vol. 2, p. 023396, 2020.

[33] O. Diekmann, D. Lentrodt, and J. Evers, "Inverse design approach to x-ray quantum optics with mössbauer nuclei in thin-film cavities," *Phys. Rev. A*, vol. 105, p. 013715, 2022.

[34] A. Pálffy, C. H. Keitel, and J. Evers, "Single-photon entanglement in the keV regime via coherent control of nuclear forward scattering," *Phys. Rev. Lett.*, vol. 103, p. 017401, 2009.

[35] S. Yip, *Nuclear Radiation Interactions*. World Scientific, 2014.

[36] S. Hüfner, *Photoelectron spectroscopy*. Advanced Texts in Physics, Berlin, Germany: Springer, 3 ed., 2013.

[37] R. Rohlsberger, *Nuclear condensed matter physics with synchrotron radiation*. Springer Tracts in Modern Physics, Berlin, Germany: Springer, 2010.

[38] M. Cooper, P. Mijnarends, N. Shiotani, N. Sakai, and A. Bansil, *X-ray Compton scattering*. Oxford Series on Synchrotron Radiation, London, England: Oxford University Press, 2004.

[39] W. Sturhahn and V. Kohn, "Theoretical aspects of incoherent nuclear resonant scattering," *Hyperfine Interactions*, vol. 123, pp. 367–399, 1999.

[40] R. L. Mössbauer, "Kernresonanzfluoreszenz von gammastrahlung in Ir^{191}," *Eur. Phys. J. A*, vol. 151, no. 2, pp. 124–143, 1958.

[41] I. R. Khairulin, V. A. Antonov, Y. V. Radeonychev, and O. Kocharovskaya, "Transformation of Mössbauer γ-ray photon waveform into short pulses in dual-tone vibrating resonant absorber," *Journal of Physics B: Atomic, Molecular and Optical Physics*, vol. 51, no. 23, p. 235601, 2018.

[42] A. Stejskal, "Development of the dual Mössbauer spectrometer and the adaptation for dynamic measurement," master thesis, Palacky University Olomouc, Faculty of Science, 2019. Supervisor: Mgr. Petr Novák, Ph.D.

[43] A. Stejskal, "Shape filtration of signal in radiation detection," bachelor's thesis, Palacky University Olomouc, Faculty of Science, 2017. Supervisor: Mgr. Michal Dudka.

[44] A. Stejskal, V. Procházka, M. Dudka, V. Vrba, J. Kočiščák, P. Šretrová, and P. Novák, "A dual mössbauer spectrometer for material research, coincidence experiments and nuclear quantum optics," *Measurement*, vol. 215, p. 112850, 2023.

[45] A. Ambrosy and K. Holdik, "Piezoelectric PVDF films as ultrasonic transducers," *Journal of Physics E: Scientific Instruments*, vol. 17, no. 10, p. 856, 1984.

[46] A. Benjeddou, "Field-dependent nonlinear piezoelectricity: a focused review," *International Journal of Smart and Nano Materials*, vol. 9, no. 1, pp. 68–84, 2018.

[47] M. Vacula, "Characterization of piezoelectric materials and components," bachelor's thesis, Palacky University Olomouc, Faculty of Science, 2016. Supervisor: doc. RNDr. Jiří Pechoušek, Ph.D.

[48] K. Omote and H. Ohigashi, "Temperature dependence of shear piezoelectric properties of poly(vinylidene fluoride) studied by piezoelectric resonance method," *Japanese Journal of Applied Physics*, vol. 35, no. 3R, p. 1818, 1996.

[49] W. POTZEL, "^{67}Zn Mössbauer spectroscopy," *Hyperfine Interactions*, vol. 71, no. 1, pp. 1515–1522, 1992.

[50] G. M. Kalvius, F. E. Wagner, and W. Potzel, "Methodology of "less used" Mössbauer isotopes," *J. Phys. Colloques*, vol. 37, no. 6, pp. 657–671, 1976.

[51] R. Shakhmuratov, F. G. Vagizov, and V. Y. Gaiduk, "Methods of coherent control of spectral and temporal properties of gamma photons and their potential applications," *Crystallography Reports*, vol. 65, pp. 409–411, 2020.

[52] I. R. Khairulin, Y. V. Radeonychev, and O. Kocharovskaya, "Slowing down x-ray photons in a vibrating recoilless resonant absorber," *Scientific Reports*, vol. 12, no. 1, 2022.

List of Publications

I. P. Novak, V. Prochazka, **A. Stejskal**, J. Kopp, and J. Pechousek, "Pulse length and amplitude filtration of gamma radiation detection, utilization in the 57Fe Mössbauer spectroscopy", *Nucl. Instr. Meth. Phys. Res. A*, vol. 940, pp. 152–155, 2019.

II. V. Procházka, P. Novák, V. Vrba, **A. Stejskal**, and M. Dudka, "Autotuning procedure for energy modulation in Mössbauer spectroscopy", *Nucl. Instr. Meth. Phys. Res. B*, vol. 483, pp. 55–62, 2020.

III. **A. Stejskal**, V. Procházka, P. Novák, and M. Dudka, "Mössbauer spectrometer designed for measurements of fast processes", *Nucl. Instr. Meth. Phys. Res. A*, vol. 984, p. 164597, 2020.

IV. G. Mazin, **A. Stejskal**, M. Dudka, and M. Ježek, "Non-blocking programmable delay line with minimal dead time and tens of picoseconds jitter", *Review of Scientific Instruments*, vol. 92, no. 11, p. 114712, 2021.

V. P. Novák, V. Procházka, and **A. Stejskal**, "Universal drive unit for detector velocity modulation in Mössbauer spectroscopy", *Nucl. Instr. Meth. Phys. Res. A*, vol. 1031, p. 166573, 2022.

VI. V. Procházka, P. Novák, **A. Stejskal**, M. Dudka, and V. Vrba, "Lamb-Mössbauer factor determination by resonant Mössbauer spectrometer", *Physics Letters A*, vol. 442, p. 128195, 2022.

VII. J. Kočiščák, P. Novák, **A. Stejskal**, J. Kopp, and V. Procházka, "High time and energy resolution semi-transparent scintillation detectors for application in γ optics and Mössbauer spectroscopy", *Measurement*, vol. 206, p. 112225, 2023.

VIII. **A. Stejskal**, V. Procházka, M. Dudka, V. Vrba, J. Kočiščák, P. Šretrová and P. Novák "A dual Mössbauer spectrometer for material research, coincidence experiments and nuclear quantum optics", *Measurement*, vol. 215, p. 112850, 2023.